

NASA MEMO 3-11-59L

NASA

MEMORANDUM

A WIND-TUNNEL INVESTIGATION TO EVALUATE THE
AERODYNAMIC PERFORMANCE OF THREE DIFFERENT AIRPLANE
CONFIGURATIONS HAVING ARROW- AND DELTA-WING PLAN

FORMS AT A MACH NUMBER OF 2.91

By James N. Mueller and John E. Grimaud

Langley Research Center
Langley Field, Va.

N71-73434

FACILITY FORM 602

(ACCESSION NUMBER)
169
(PAGES)
(NASA CR OR TMX OR AD NUMBER)

(THRU)
Open
(CODE)
(CATEGORY)

NATIONAL AERONAUTICS AND SPACE ADMINISTRATION

WASHINGTON

May 1959

REPRODUCED BY
NATIONAL TECHNICAL
INFORMATION SERVICE
U. S. DEPARTMENT OF COMMERCE
SPRINGFIELD, VA. 22161

110

NATIONAL AERONAUTICS AND SPACE ADMINISTRATION

MEMORANDUM 3-11-59L

A WIND-TUNNEL INVESTIGATION TO EVALUATE THE
AERODYNAMIC PERFORMANCE OF THREE DIFFERENT AIRPLANE
CONFIGURATIONS HAVING ARROW- AND DELTA-WING PLAN

FORMS AT A MACH NUMBER OF 2.91*

By James N. Mueller and John E. Grimaud

SUMMARY

A wind-tunnel investigation to evaluate the aerodynamic performance of three basic airplane configurations referred to as the low-aspect-ratio arrow-, the high-aspect-ratio arrow-, and the delta-wing configurations has been made at a Mach number of 2.91 and Reynolds numbers of 0.8 to 1.6×10^6 in the Langley 9-inch supersonic wind tunnel for angles of attack of -2° to 8° at an angle of sideslip of 0° and for sideslip angles of -6° to 4° at an angle of attack of 0° .

Maximum lift-drag ratios obtained on the delta-, low-aspect-ratio arrow-, and high-aspect-ratio arrow-wing configurations were 6.3, 5.6, and 5.4, respectively, for the condition of all turbulent flow over the models and zero base drag. The results show that, for the low-aspect-ratio arrow-wing configuration, the pitching moment at the maximum lift-drag ratio can be reduced to zero by canting a forepart of the wing and body upward without loss in maximum lift-drag ratio, and that the pitching moment of the delta-wing configuration is near zero at the maximum lift-drag ratio for these tests. Extrapolation of the maximum lift-drag ratio results to full-scale Reynolds number and with an assumed base-pressure coefficient of $-1/M^2$ acting on the models (where M is the free-stream Mach number) gave values of 7.00, 6.07, and 7.23 for the low-aspect-ratio arrow-, high-aspect-ratio arrow-, and delta-wing configurations, respectively. All complete models show positive directional stability about a center-of-gravity location that is believed to be realistic. The effect of fuselage shape on the aerodynamic characteristics of the low-aspect-ratio arrow-wing configuration when the ogive-cylinder body was replaced with a 2/3-power half-body of equal volume is shown to be negligible on the maximum lift-drag ratio results and favorable in regard to trim at maximum lift-drag ratio. Estimated aerodynamic characteristics of the complete configurations are shown to agree well with experimental results.

K

L
1
8
3



INTRODUCTION

The Langley Research Center is participating in an accelerated research program to provide information on the design of aircraft configurations capable of cruise flight at Mach numbers near 3. In this program several model configurations proposed for cruise flight at Mach numbers near 3 have been designed and tested. Results of these investigations are reported in references 1 to 6. Favorable lift-interference effects (refs. 1 to 5), or reduction in drag due to lift (ref. 6) have been the design philosophy of the configurations reported on in these references.

As a continuing effort of the program tests have been conducted in the Langley 9-inch supersonic wind tunnel on several airplane configurations which were designed with the view of minimizing wave drag. All components of the airplanes were made as thin as was considered practicable. This paper presents results obtained on three of these thin-element configurations and on modifications to them. The three basic configurations are herein referred to as the low-aspect-ratio arrow-, high-aspect-ratio arrow-, and delta-wing configurations.

The tests were made at a Mach number of 2.91 in the Reynolds number range 0.8 to 1.6×10^6 with and without transition fixed on the models. Tests extended over an angle-of-attack range of -2° to 8° at an angle of sideslip of 0° and a sideslip-angle range of -6° to 4° at an angle of attack of 0° .

SYMBOLS

A	aspect ratio, b^2/S
b	wing span
\bar{c}	wing mean aerodynamic chord
C_L	lift coefficient, $\frac{\text{Lift}}{qS}$
$C_{L,opt}$	lift coefficient at maximum L/D
C_D	drag coefficient, $\frac{\text{Drag}}{qS}$
$C_{D,min}$	minimum drag coefficient

$C_{D,0}$	zero-lift drag coefficient
$C_{D,f}$	skin-friction drag coefficient
C_Y	side-force coefficient, $\frac{\text{Side force}}{qS}$
C_n	yawing-moment coefficient, $\frac{\text{Yawing moment}}{qSb}$
$C_{p,b}$	base-pressure coefficient, $\frac{P_b - P_\infty}{q_\infty}$
C_m	pitching-moment coefficient, $\frac{\text{Pitching moment}}{qS\bar{c}}$
$C_{m,0}$	pitching-moment coefficient at zero lift
$C_{m\alpha}$	pitching-moment curve slope
$\frac{dC_n}{dC_Y}$	lateral-stability parameter
$C_{L\alpha}$	lift-curve slope
$\frac{dC_m}{dC_L}$	longitudinal-stability parameter
$C_{n\beta}$	directional-stability parameter
$C_{Y\beta}$	side-force parameter
$\frac{C_D}{C_L^2}$	drag-due-to-lift parameter
L/D	lift-drag ratio
M	Mach number
p	static pressure
q	dynamic pressure
R	Reynolds number

S	wing area
V	body volume
x	longitudinal distance measured from leading edge of wing mean aerodynamic chord
x_{cp}/\bar{c}	longitudinal center-of-pressure location referenced to leading edge of wing mean aerodynamic chord
α	angle of attack
β	angle of sideslip
ϵ	wing semiapex angle
μ	Mach angle

Subscripts:

max	maximum
b	base
cp	center of pressure
∞	free stream

CONFIGURATION DESIGNATIONS

The various components of the configurations are designated as follows:

Low-aspect-ratio arrow wing:

B	ogive-cylinder body
B'	modified ogive-cylinder body
B ₁	2/3-power half-body
F _{1,0}	wing-tip fins at 0° toe-in
F _{1,5}	wing-tip fins at 5° toe-in

W_1 wing

N_6, N_4, \dots six nacelles, four nacelles, etc.

N_6', N_4', \dots nacelles displaced $0.09lb/2$ further outboard than original location

(FT) fixed transition

High-aspect-ratio arrow wing:

B_2 $2/3$ -power half-body

W_2 wing

$F_{2,0}$ wing-tip fins at 0° toe-in

N_6 six nacelles

(FT) fixed transition

Delta wing:

B_3 $2/3$ -power half-body

$B_{3,ext}$ extended $2/3$ -power half-body

$B_{3',ext}$ modified extended $2/3$ -power half-body

W_3 wing

N_6, N_4, \dots six nacelles, four nacelles, etc.

V vertical tail

F_L large wing-tip fins

F_S small wing-tip fins

$B_{3,inv}$ $2/3$ -power half-body mounted to upper surface of wing

V_{inv} vertical tail mounted to lower wing surface

$N_{6,inv}$ nacelles mounted to upper surface of wing

APPARATUS AND TESTS

Wind Tunnel, Balance, and Model Support

The investigation was conducted in the Langley 9-inch supersonic wind tunnel which is a continuous, closed-return type of tunnel with provisions for the control of the humidity, temperature, and pressure of the enclosed air. During the tests the quantity of water vapor in the tunnel air was kept sufficiently low so that the effect of water condensation in the supersonic nozzle was negligible.

The balance system used in these tests was a six-component, external type which utilized mechanical, self-balancing beams for force measurements. A detailed description of this balance system is presented in the appendix of reference 7.

The models were sting mounted to the model support of the external balance system. (See fig. 1(a).) The stings were shielded from air loads by a movable windshield which was equipped with four pressure tubes open at the snout of the windshield to measure model base pressures. The streamwise gap between the base of the models and the snout of the windshield was maintained at about 0.010 inch or less for all tests.

Models

General.- The three different basic airplane configurations are shown in figures 1 to 3. The configurations were complete in that they consisted of a wing, body, nacelles, and vertical stabilizing surfaces, such as wing-tip fins or vertical tail; however, no movable control surfaces were employed on the models. Each model was equipped with six cylindrical nacelles externally mounted on sweptback, beveled pylons beneath the wings of the configurations. The nacelle dimensions were the same for all configurations. Table I presents detail dimensions of the nacelles and the other component parts of each configuration. The 2/3-power half-body fuselages shown on the configurations were selected on the basis of Cole's work presented in reference 8, and the ordinates for these bodies are shown in table II. The location of the selected moment reference (center of gravity) on the models is shown in figures 1 to 3. The ratio of body volume to wing area of all configurations was

held approximately constant $\left(\frac{v^{2/3}}{S} = 0.034 \text{ to } 0.035\right)$. Photographs of the models are shown in figures 4 to 7.

Low-aspect-ratio arrow wing.- A three-view drawing of the low-aspect-ratio arrow-wing configuration is shown in figure 1. The wing had leading- and trailing-edge sweep angles of 67.4° and 26.6° , respectively. The wing tips were clipped and vertical wing-tip fins were affixed thereto. The wing section in a streamwise direction was a single, 2-percent-thick wedge with a sharp nose and blunt base. The lower surface of the wing was flat. One version of this configuration employed an ogive-cylinder body (fig. 1(a)), and a second version was equipped with a $2/3$ -power half-body (fig. 1(b)). The ogive-cylinder body is mounted to the wing in such a way that the flat lower surface of the wing is along the center line of the body, whereas the $2/3$ -power half-body is mounted directly to the flat, lower surface of the wing. A modification to the $2/3$ -power half-body configuration in which a forward portion of the wing and body was canted upwards $3\frac{1}{2}^\circ$ is shown in figure 1(b). The ogive-cylinder body was altered, to change effectively the camber of the fuselage, by replacing approximately 75 percent of the length of the upper surface of the body with a conical body segment (fig. 1(a)).

High-aspect-ratio arrow wing.- A three-view drawing of the high-aspect-ratio arrow-wing configuration is shown in figure 2. The wing had leading- and trailing-edge sweep angles of 67.4° and 49.3° , respectively. The aspect ratio was 2.265. The wing tips were clipped for the attachment of wing-tip fins set at 0° relative to free-stream direction. The airfoil sections in streamwise planes were 2-percent-thick single wedges with sharp noses and blunt bases. The lower surface of the wing was flat. This configuration was equipped with a $2/3$ -power half-body attached to the lower surface of the wing.

Delta wing.- A three-view drawing of the delta-wing configuration is shown in figure 3. The wing had a leading-edge sweep angle of 53.15° . The wing section in a streamwise plane is a symmetrical double wedge with the location of the maximum thickness at $0.70\bar{c}$. The selection of this wing was based on some results of wing-alone tests performed on $3\frac{1}{2}$ -percent-thick delta wings of the same airfoil sections. (See ref. 9.) The results presented in reference 9 showed that the maximum L/D was obtained at the highest wing tangent ratio ($\tan \epsilon / \tan \mu$) and the highest Mach number of the tests. ($L/D = 10.8$ at $\tan \epsilon / \tan \mu = 1.85$ and $M = 2.41$.) Also, the trend of $(L/D)_{\max}$ with increase in tangent-ratio

value was shown to be upward. Accordingly, the delta wing of the present tests was designed to have a tangent ratio of 2.05 at the test Mach number of this investigation. The delta wing was equipped with a 2/3-power half-body the length of which equaled the root chord of the wing. (See fig. 3(a).) The wing was also equipped for additional tests with a long 2/3-power half-body in which a forward portion of the body protruded beyond the wing apex. (See fig. 3(b).) The body volume of the normal-length and long-body configurations was held constant. The normal-length-body configuration (fig. 3(a)) comprised three configurations: (1) a large tip-fin configuration, (2) a small tip-fin configuration, and (3) a vertical-tail configuration (no tip fins). The long-body configuration was equipped with only the vertical tail.

Test Conditions and Procedure

The tests were made at a Mach number of 2.91 and Reynolds number of 0.8 to 1.6×10^6 based on wing mean aerodynamic chord. All configurations were tested through an angle-of-attack range of -2° to 8° at an angle of sideslip of 0° and through an angle-of-sideslip range of -6° to 4° at an angle of attack of 0° . Most of the tests were made with natural boundary-layer transition on the models (smooth models); however, some tests were made with the models having roughness strips with thicknesses of 0.005 to 0.008 inch attached to the upper and lower surfaces of the wings near the leading edges. The roughness strips were composed of spherical aluminum oxide particles and were attached to the wing surfaces by means of a plastic adhesive. (See fig. 1, for example, for the location and size of the roughness strips.)

Measurements, Corrections, and Accuracy

Lift, drag, pitching moments, side force, and yawing moments were measured on an external balance system. Angle of attack and angle of sideslip of the models were determined with an optical system for indicating pitch and yaw attitude of the models. In this system, small (1/16-inch-diameter) mirrors are attached to the models near the rear of the fuselages or on the tip fins or nacelles. These mirrors reflect an image from an external light source onto a graduated scale. A limited number of tests were made in which the wing base pressures on the low-aspect-ratio arrow-wing configuration were measured over a Reynolds number range of 0.825 to 3.06×10^6 . In other pressure tests, the body base pressure on the low-aspect-ratio arrow wing equipped with a 2/3-power half-body were measured, and the nacelle flow characteristics were determined. Some schlieren photographs of the various models are shown in figures 8 to 10.

Standard corrections for sting-mounted models in the Langley 9-inch tunnel were applied to the drag data of the configurations to account for the difference between free-stream pressure and (1) the measured pressure on the base of the fuselage and (2) the pressure in the fixed-windshield—shield—balance-box enclosure. This correction amounts to correcting the base pressure of the fuselage to free-stream static-pressure conditions or to zero base drag. No corrections were applied to the drag data to account for the wing base-pressure drag of the low-aspect-ratio and high-aspect-ratio arrow wings which have blunt trailing edges. However, it is shown in figure 11 that the wing base pressures measured on these configurations are within the range to be expected in flight. ($C_{p,b} \approx -0.1$) (See refs. 10 and 11.)

Accuracy of the presented data based on balance calibration is estimated to be within the following limits:

C_L	± 0.001
C_D	± 0.0002
C_m	± 0.002
C_Y	± 0.001
C_n	± 0.002
L/D	± 0.15
M	± 0.01
α , deg	± 0.05
β , deg	± 0.05
R	$\pm 0.02 \times 10^6$

RESULTS AND DISCUSSION

General

In the discussion to follow the measured aerodynamic characteristics in pitch and sideslip of the three basic complete airplane configurations tested are presented first as basic plots showing component data. This presentation is followed by comparison plots showing the effects of the various airplane components on the longitudinal and lateral characteristics of each configuration. (See figs. 12 to 24 for the low-aspect-ratio arrow-wing configurations; figs. 25 to 27 for the high-aspect-ratio arrow-wing configurations; and figs. 28 to 37 for the delta-wing configurations.) The experimental results are summarized in table III. Summary plots are then shown for center-of-pressure variations (fig. 38), drag-due-to-lift parameter (figs. 39 and 40), and lift-drag ratios (fig. 41) for the three basic complete airplane configurations. The corrected wind-tunnel

lift-drag ratios obtained on the models are shown extrapolated to full-scale values in figure 42.

Since the full-scale configurations at flight conditions are expected to have fully turbulent boundary-layer flow, and because of the relatively low Reynolds numbers of the present tests which preclude turbulent boundary-layer flow over most of the surfaces of the models, roughness strips were attached near the wing leading edges to induce boundary-layer transition artificially in a number of representative tests. In cases where this technique was followed, the basic data symbols are flagged or else the data are so designated. However, more credence is given to the smooth or natural transition model data and the curves are faired accordingly. The natural transition data are used because it is felt that the transition particles, which are of necessity large compared with model size, contribute some wave drag, the amount of which is not known. Also, as shown later, the estimated aerodynamic characteristics of the three basic complete models based on conditions of natural transition and the assumption of areas of laminar and turbulent flow over the models agree well with the experimental results. (The estimated aerodynamic characteristics of these models are presented in table IV.)

Low-Aspect-Ratio Arrow Wing

Basic data.- Figure 12 shows the pitch results of the individual tests on various configurations of the low-aspect-ratio arrow wing in component build-up sequence. Also shown are the tests in which modifications to the original model were made. The flagged symbols on some of the figures indicate the results of tests with a roughness strip affixed near the leading edge of the wing. (See fig. 1 for location and size of roughness strip.) The unflagged symbols represent data obtained for the smooth (or natural transition) model. In all cases the faired data points are for the natural transition tests.

In general, the lift and pitching-moment data show good linearity at least up to maximum L/D. Also the pitching-moment curves for all the configurations exhibit a stable slope. Theoretical estimates of lift, drag, and lift-drag ratio are shown for a complete model test in figure 12(d). (See table IV for values of estimated quantities.) When the model lift was estimated, only the wing was considered and the linear-theory lift-curve slope of the isolated wing surface was calculated. Drag due to lift was assumed to be determined by the reciprocal of the lift-curve slope of the wing and zero-lift drag was obtained by the simple addition of the wave and skin-friction contributions of the component parts of the model. This method for estimating the theoretical coefficient follows that used in reference 12. These estimated values of the aerodynamic characteristics are seen to be in good agreement with experiment.

It is observed that the effects of fixing transition on representative models (see, for example, fig. 12(h)) are most evident in the drag and lift-drag ratio curves, as would be expected, and the decrease in lift-drag ratio due to fixing transition is not large for this model.

The measured aerodynamic characteristics in sideslip at $\alpha = 0^\circ$ of the several low-aspect-ratio arrow-wing configurations are shown in figure 13. All the configurations exhibit positive directional stability, even for the model with no tip fins (BW_1N_6) although the value of $C_{n\beta}$ is small for this case.

Effects of trimming.- As the configurations tested in this investigation were without movable pitch-control surfaces, lift-drag ratios presented are those for the untrimmed condition of the configurations. However, it is known that a positive pitching-moment shift with minimum penalty to $(L/D)_{\max}$ can be achieved by simple means such as canting upward a portion of the wing and body forward of the center-of-gravity position or by fuselage camber as discussed in reference 13.

In order to investigate the effects of canting a portion of the wing to achieve trimmed conditions near $(L/D)_{\max}$, the low-aspect-ratio arrow-wing configuration with the 2/3-power half-body ($B_1W_1N_6'F_{1,0}$) was altered in that a portion of the wing was deflected upward $3\frac{1}{2}^\circ$. (See fig. 1(b).) The results obtained are shown in figure 14 along with the results obtained on the unmodified configuration. It is seen that canting the wing upward produced a significant increase in the positive value of $C_{m,0}$ at no expense to $(L/D)_{\max}$. The pitching-moment data for the canted-wing configuration show a near trimmed condition at $(L/D)_{\max}$. The $(L/D)_{\max}$ of the two configurations are seen to be about the same. Also, no significant changes occurred in the drag polar or lift-curve-slope parameters. There is, however, a slight negative increase in the pitching-moment-curve slope when the wing is canted upward which is not desirable from control-force considerations.

In order to show the effects of fuselage camber on $(L/D)_{\max}$, a complete configuration $BW_1N_6F_{1,0}$ was altered by replacing approximately 75 percent of the forward length of the upper surface of the ogive-cylinder body (the body portion above the top surface of the wing) with a conical body segment. (See drawing in fig. 1(a).) As seen in figure 15 a positive, although small, increase in the value of the pitching moment through the lift range is achieved without any change to the maximum value of L/D obtained on the original configuration.

Effects of tip fins.- The effects of tip fins with and without toe-in and no tip fins on the aerodynamic characteristics of a complete configuration are compared in figures 16 and 17. Tip-fin effects on the longitudinal results (fig. 16) show that the configuration with the 5° toe-in tip fins ($BW_1N_6F_{1,5}$) has a greater $(L/D)_{max}$ than the configuration with 0° toe-in tip fins ($BW_1N_6F_{1,0}$). In the absence of detail pressure distributions the exact reasons for this result are not known. The tip-fin-equipped configurations exhibit greater longitudinal stability than the finless configuration as can be seen in the plot of C_m against C_L .

The effects of tip-fin angularity on the lateral characteristics are shown in figure 17. It is seen that the angularity of the tip fins, for this particular configuration, has a negligible influence on the directional stability. However, it should be pointed out that this result cannot be construed as being indicative of the effects of tip-fin toe-in on other configurations, since other test results (unpublished) have shown that the effect of toe-in is favorable on directional stability. As indicated by the positive slopes of the plots of C_n against β , all configurations indicate positive directional stability, even for the configuration which is without tip fins.

Effects of fuselage shape.- In figures 18 and 19 the effects on the longitudinal and lateral characteristics, respectively, of changing fuselage shapes from the original ogive-cylinder body ($BW_1N_6F_{1,0}$) to a $2/3$ -power half-body mounted to the lower surface of the wing ($B_1W_1N_6F_{1,0}$) are shown. The effects on $(L/D)_{max}$ (fig. 18) are negligible. However, it should be pointed out that the L/D results shown are for the condition of zero base drag. As the base of the $2/3$ -power half-body fuselage configuration ($B_1W_1N_6F_{1,0}$) is larger than the ogive-cylinder body configuration ($BW_1N_6F_{1,0}$), it would be expected that the $(L/D)_{max}$ of the configuration with the larger base would be less than that of the original configuration when the base drag is considered.

Probably the most significant advantage of the $2/3$ -power half-body is the favorable effect on pitching-moment characteristics. The pitching moment to be trimmed out at $(L/D)_{max}$ for this configuration ($B_1W_1N_6F_{1,0}$) is about one-half that of the ogive-cylinder body configuration ($BW_1N_6F_{1,0}$). Both configurations indicate positive longitudinal stability.

The effects of fuselage shape on lateral characteristics are shown in figure 19 to be small.

Effects of nacelles.- Figure 20 shows the effects of the nacelles on the longitudinal characteristics of the low-aspect-ratio arrow-wing configuration ($BW_1N_6F_{1,5}$) equipped with the ogive-cylinder body. The nacelles were successively removed in pairs starting at the inboard location. As would be expected, the $(L/D)_{max}$ values increase when the nacelles are removed, except for the case when the two inboard nacelles are removed and the $(L/D)_{max}$ remains practically unchanged. (Compare configurations $BW_1N_6F_{1,5}$ and $BW_1N_4F_{1,5}$.) This exception can probably be ascribed to a favorable lift-interference effect generated by the inboard-nacelles body arrangement on the complete configuration ($BW_1N_6F_{1,5}$). The drag shows the expected decrease as the nacelles are successively removed, but there is essentially no change in the slope of the curve for the variation of C_m with C_L with nacelle removal. All configurations show a stable variation of C_m with C_L .

The inboard nacelles on a $2/3$ -power half-body configuration were also removed and the results are compared with the six-nacelle configuration in figure 21(a). Also included in the same figure are the results obtained on the ogive-cylinder body configuration with and without the inboard nacelles. (See fig. 21(b).) The removal of the inboard nacelles on the $2/3$ -power half-body configuration results in a $(L/D)_{max}$ increase of twice that obtained on the ogive-cylinder configuration, although small, which suggests that the favorable lift interference effects are less on this configuration than that on the ogive-cylinder body configuration.

In figures 22 and 23 the effects of moving all nacelles outboard 0.091b/2 on the aerodynamic characteristics of the low-aspect-ratio arrow-wing configuration with the ogive-cylinder body ($BW_1N_6'F_{1,0}$) are shown. The most noticeable effects on the longitudinal characteristics (fig. 22) appear as a reduction in maximum lift-drag ratio when the nacelles are displaced outboard. This condition is reflected in the drag data where it is seen that the configuration with the nacelles outboard has slightly more drag, whereas the lift-curve slopes of the configurations are essentially the same. This result lends credence to the preceding discussion on favorable lift-interference effects associated with nacelle placement close to the body.

The effects on lateral characteristics of displacing the nacelles outboard are shown in figure 23. Although an essentially constant increment in C_Y and C_N is noted, the slopes of $C_{N\beta}$ and $C_{Y\beta}$ are not significantly different for the different nacelle locations. A higher drag is noted for the case where the nacelles are further outboard, however.

Effects of Reynolds number.- In figure 24 the effects of Reynolds number on the force coefficients of two low-aspect-ratio arrow-wing configurations are shown. Figure 24(a) is for the ogive-cylinder body configuration ($BW_1N_6'F_{1,0}$), and figure 24(b) is for 2/3-power half-body configuration ($B_1W_1N_6'F_{1,0}$). The only significant change in the force data with Reynolds number is seen to be the slight increase in lift-drag ratio with increase in Reynolds number for both configurations.

High-Aspect-Ratio Arrow Wing

The second model tested in the three basic airplane configuration series was a high-aspect-ratio arrow wing equipped with a 2/3-power half-body (fuselage) mounted on the lower surface of the wing. This model was similar to the low-aspect-ratio arrow wing with the 2/3-power half-body (previously discussed) in that the wing leading-edge sweep is unchanged and the six nacelles are identical in dimensions. The wing trailing-edge sweep angle and span were increased, however, to obtain an aspect ratio of 2.265 which is approximately 51 percent greater than that of the low-aspect-ratio arrow wing. The high-aspect-ratio arrow wing was equipped with tip fins at 0° toe-in similar to the low-aspect-ratio arrow wing. The results of the high-aspect-ratio arrow wing are presented in figures 25 to 27. In figure 25, the measured aerodynamic characteristics in pitch are shown for the natural-transition case (smooth model) and also for the fixed-transition case (denoted by the flagged data points). It is seen that the $(L/D)_{\max}$ for this configuration is about 5.6, which is only slightly higher than the values obtained on the low-aspect-ratio arrow-wing configuration ($B_1W_1N_6'F_{1,0}$, fig. 12(i)). The lift-curve slope is linear in a narrow range of angle of attack ($\alpha = \pm 2^\circ$) with a gradual decrease evident as α is increased beyond $\alpha = 2^\circ$. The selected location of the moment reference center results in an unstable variation of the pitching moment with lift. The moment curve is linear, however, through the angle-of-attack range. The principal effect of fixing transition on the model is most noticeable in the drag polar where an increase in the drag, as would be expected, is noted (fig. 25). This increase in drag is reflected in a reduced value of $(L/D)_{\max}$ of about 0.3. The estimated aerodynamic characteristics of the complete configuration are shown in figure 25 and are seen to agree well with the experimental results. (See table IV for estimated values.) The estimated characteristics were determined in the same manner as for the low-aspect-ratio arrow-wing configuration described previously.

In figure 26 the measured aerodynamic characteristics in sideslip for the high-aspect-ratio arrow-wing configuration are presented. The configuration is seen to be directionally stable at the angle of attack of these tests ($\alpha = 0^\circ$).

In figure 27 the effects of Reynolds number on the measured aerodynamic characteristics in pitch are shown. It is seen that the change in $(L/D)_{\max}$ is small with negligible change in drag.

Delta Wing

Basic data.- The measured aerodynamic characteristics in pitch of the delta-wing configurations are presented in figure 28. The figure shows the results on individual tests of the various configurations of the delta-wing airplane. Most of the data were obtained for the case where the model is without fixed-transition strips attached to the wing surfaces (natural transition). In the tests where fixed transition was used, the data are shown as flagged symbols. (The location and size of the roughness strips are shown in fig. 3.) In all cases the paired data points are for the natural transition tests.

In general, the lift and pitching-moment data exhibit good linearity through the range of angle of attack of the tests. The selection of the pitching-moment reference center on the model (0.50c) resulted in unstable variation of pitching moment with lift. But as seen from the figures (for example, fig. 28(e)) the complete configurations show near neutral stability, that is, small variation of C_m with C_L . The effects of fixing transition are reflected in the lift-drag ratio curves as a rather large reduction in $(L/D)_{\max}$ values as compared with the values for the natural transition data. (See, for example, fig. 28(e).) The reduction is of the order of 1 in $(L/D)_{\max}$.

In estimating the theoretical characteristics of the models, the procedures as explained in the low-aspect-ratio arrow-wing section were used. The theoretical estimates are shown to agree with the measured data, as shown in a representative case (fig. 28(e)). (See table IV for estimated values.)

The measured aerodynamic characteristics in sideslip (at $\alpha = 0^\circ$) of several delta-wing configurations are shown in figure 29. All the configurations show positive directional stability, including the configuration without directional stabilizing control surfaces $B_3W_3N_6$. The variations of C_n and C_y with sideslip angle β are generally linear throughout the sideslip-angle range.

Effect of tip-fin size.- In figures 30 and 31 the effects of the tip-fin size on longitudinal and lateral characteristics, respectively, of the delta-wing configurations are shown. The results are also compared with the configuration without tip fins. It is seen (fig. 30) that the configuration equipped with the large tip fins has a higher

$(L/D)_{\max}$ than the small tip-fin-equipped configuration ($B_3W_3N_6F_S$). The high lift-drag ratio can probably be attributed to a more favorable end-plate effect (higher $C_{L\alpha}$) provided by the larger tip fins. The configuration equipped with large tip fins is, however, more unstable than the configuration with small tip fins which is nearly neutrally stable. The drag data show the configurations with no tip fins to have the least drag followed by the large and small tip-fin configurations in that order.

In figure 31 the effects of tip-fin size on the lateral characteristics of the delta-wing configurations are shown. The directional stability of the configurations is positive, including the configuration with no directional stabilizing surfaces, and the directional stability provided by the large tip fins ($B_3W_3N_6F_L$) as indicated by the slope of C_n against β is about twice that provided by the small tip fins. The area of the large tip fins is over twice the area of the small tip fins. In addition to the difference in size of the tip fins, the geometry of the fins is very different.

Comparison of tip-fin and vertical-tail effects.- In figure 32 a comparison of the effects on longitudinal characteristics of the delta-wing configuration equipped with a vertical tail ($B_3W_3N_6V$) and with the large tip fins ($B_3W_3N_6F_L$) is shown. The maximum lift-drag ratio of the vertical-tail configuration is significantly greater than that of the large tip-fin configuration, and only slightly less than that for the configuration without directional stabilizing surfaces ($B_3W_3N_6$). A comparison of the drag curves shows that the addition of the vertical tail does not increase the drag, within measurable limits, over that of the configuration without directional controls ($B_3W_3N_6$). With reference to the moment data, it is seen that the vertical-tail configuration ($B_3W_3N_6V$) is slightly unstable and has a low value of pitching moment at maximum L/D .

Figure 33 compares the lateral characteristics of the large tip-fin-equipped configuration with the configuration equipped with the vertical tail. The vertical tail has only about one-third the effectiveness in providing directional stability as that of the large tip fins. A significant increase in the side force provided by the wing-tip fins over that provided by the vertical tail is also evident in the plot of C_y against β .

Effects of fuselage modification.- Figure 34 shows the effects on the longitudinal characteristics of the delta-wing configuration when the original body is replaced with an elongated body of the same volume. (See fig. 3(b).) The purpose of increasing the length of the body forward of the wing apex was an attempt to create a favorable upwash field

over the wing upper surface and thereby improve the lift-drag ratio of the configuration by increasing the wing lift. However, as seen in figure 34, the changes effected in the lift-drag ratio, pitching moment, and drag are negligible. A slight modification to the extended body configuration ($B_{3,ext}W_3N_6V$) in the form of rounding off the sharp corners of the body at the juncture of the flat upper portion and curved under-surface to alleviate flow separation at the sharp edge ($B_{3',ext}W_3N_6V$) resulted in no change in the aerodynamic characteristics of the configuration. The pitching-moment data show that all the configurations are essentially trimmed at $(L/D)_{max}$, although the curves indicate that the configurations are slightly unstable. The data presented here are for the fixed-transition case.

Figure 35 shows that the effects of elongating the fuselage on the lateral characteristics of the delta-wing configuration are negligible.

Effects of inverting fuselage.- The effect of inverting the fuselage (placing the fuselage on the upper wing surface) on the aerodynamic characteristics of the delta-wing configuration is shown in figure 36. The data show that a substantial loss in $(L/D)_{max}$ is incurred when the fuselage is placed on the upper surface of the wing. (The vertical tail has also been inverted or placed on the lower surface of the wing for this configuration ($B_{3,inv}W_3N_6V_{inv}$).) The plot C_L against α shows that, when the fuselage is placed on the upper surface of the wing, the angle of attack for maximum lift-drag ratio for this configuration is about 50 percent higher than that for the original configuration. The decrease in $(L/D)_{max}$ can be attributed to the higher drag due to lift.

Effects of nacelles.- In figure 37 the effects of nacelles on the longitudinal characteristics of the delta-wing configuration are shown. These data are for the fixed-transition case as indicated by the configuration designations on the figure. The lift-drag ratio shows the expected increase as the nacelles are successively removed in pairs starting with the inboard pair. The drag data show parallel behavior in that a decrease occurs when the nacelles are removed. The pitching-moment data indicate that the complete configuration ($B_3W_3N_6V$) has the least out-of-trim moment of the four configurations shown. The lift-curve slopes are essentially the same for all configurations, although the curves are displaced as the nacelles are removed.

Comparisons of the Basic Configurations

Center of pressure.- The center-of-pressure variations of the three basic airplane configurations are shown in figure 38. With exception of

the high-aspect-ratio arrow-wing configuration ($B_2W_2N_6F_{2,0}$), the variation of the center of pressure of the configuration is small over the angle-of-attack range of the tests. It is seen that the delta-wing configurations ($B_3W_3N_6V$ and $B_3W_3N_6FS$) exhibit near neutral stability. The high-aspect-ratio arrow-wing and delta-wing configurations have an unstable center-of-pressure location based on the selection of the moment reference center of these models.

Drag due to lift.- In figure 39 the drag due to lift of the three basic airplane configurations is plotted and the results are summarized in figure 40 as a function of wing aspect ratio. The infinite-aspect-ratio value of the drag-due-to-lift parameter is also shown in this figure. The delta wing had the lowest drag due to lift of the three basic configurations shown, the high-aspect-ratio arrow wing having the largest value.

Lift-drag ratio (wind tunnel).- In figure 41(a), the lift-drag ratios of the three basic configurations are shown for the case where the models were tested under conditions of natural boundary-layer transition (smooth models). In figure 41(b) the drag data have been corrected as noted and the corresponding lift-drag ratio results are shown. The increment in skin-friction drag (as shown) was used to correct the model drag to all-turbulent flow. No correction for $C_{D,b}$ for the low-aspect-ratio arrow wing with the ogive-cylinder body ($BW_1N_6F_{1,5}$) is shown, inasmuch as this correction has already been applied in the initial data reduction. The corrections shown for nacelle internal skin-friction drag and nacelle internal-pressure drag are for six nacelles. The internal skin-friction drag was calculated on the basis of a laminar boundary layer and with the assumption of free-stream Mach number within the nacelles. (See ref. 14.) The final $(L/D)_{max}$ ratios are shown to be 6.3 for the delta-wing configuration ($B_3W_3N_6V$), 5.6 for the low-aspect-ratio arrow-wing configuration ($BW_1N_6F_{1,5}$), and 5.4 for the high-aspect-ratio arrow-wing configuration ($B_2W_2N_6F_{2,0}$). These values are for the case where the base drag is zero.

Lift-drag ratio (full-scale extrapolation).- In figure 42 the all-turbulent $(L/D)_{max}$ values of the three basic airplane configurations are shown extrapolated to a full-scale Reynolds number of 10^8 . The unflagged symbols denote the case where the base drag of the models is zero, whereas the flagged symbols denote the condition whereby the base-pressure coefficient on the models is assumed to be $-1/M^2$. It is seen, that for the case in which base drag is considered, the extrapolated results for the delta-wing, low-aspect-ratio arrow-wing, and high-aspect-ratio arrow-wing configurations are 7.23, 7.00, and 6.07, respectively.

The low-aspect-ratio arrow-wing configuration with the smallest base area of the three configurations has the lowest base drag and, consequently, the least loss in $(L/D)_{\max}$ due to base drag. Consequently, the $(L/D)_{\max}$ of this configuration approaches closely that of the delta wing.

CONCLUSIONS

L
1
8
3
A wind-tunnel investigation to evaluate the aerodynamic performance of three basic airplane configurations referred to as the low-aspect-ratio arrow-wing, the high-aspect-ratio arrow-wing, and the delta-wing configurations has been made at a Mach number of 2.91 in the Reynolds number range of 0.8 to 1.65×10^6 . The following conclusions are drawn from the results:

1. Lift-drag-ratio results obtained on the low-aspect-ratio arrow-wing, high-aspect-ratio arrow-wing, and delta-wing configurations for the conditions of all-turbulent flow on the models and zero base drag show values of maximum lift-drag ratio $(L/D)_{\max}$ of 5.6, 5.4, and 6.3, respectively. Results show that the pitching moment of the low-aspect-ratio arrow-wing configuration at $(L/D)_{\max}$ can be reduced to zero by canting the nose upward without loss in $(L/D)_{\max}$, and that the pitching moment of the delta-wing configuration is near zero at $(L/D)_{\max}$ for these tests.

2. Lift-drag ratio results extrapolated to full-scale Reynolds number (10^8) and the condition that the base-pressure coefficient is $-1/M^2$ (M denoting Mach number) showed the delta-wing configuration to have a $(L/D)_{\max}$ of 7.23 as compared with values of 7.00 and 6.07 for the low- and high-aspect-ratio arrow-wing configurations, respectively.

3. All complete configurations show positive directional stability for a center-of-gravity position that is believed to be realistic.


4. The effects on the aerodynamic characteristics of the low-aspect-ratio arrow-wing configuration when the fuselage was changed from the ogive-cylinder body to a $2/3$ -power half-body of the same volume is shown to be negligible on $(L/D)_{\max}$ and favorable in regard to trim at maximum lift-drag ratio.

CONFIDENTIAL



5. Estimated aerodynamic characteristics of the complete configurations are shown to agree well with experimental results.

Langley Research Center,
National Aeronautics and Space Administration,
Langley Field, Va., December 19, 1958.



REFERENCES

1. Sleeman, William C., Jr.: Preliminary Study of Airplane Configurations Having Tail Surfaces Outboard of the Wing Tips. NACA RM L58B06, 1958.
2. Kelly, Thomas C., Carmel, Melvin M., and Gregory, Donald T.: An Exploratory Investigation at Mach Numbers of 2.50 and 2.87 of a Canard Bomber-Type Configuration Designed for Supersonic Cruise Flight. NACA RM L58B28, 1958.
3. Church, James D., Hayes, William C., Jr., and Sleeman, William C., Jr.: Investigation of Aerodynamic Characteristics of an Airplane Configuration Having Tail Surfaces Outboard of the Wing Tips at Mach Numbers of 2.30, 2.97, and 3.51. NACA RM L58C25, 1958.
4. Silvers, H. Norman, and Zedekar, Raymond L.: Investigation of the Aerodynamic Characteristics of a Model of a Supersonic Bomber Configuration With a Swept and an Unswept Wing at Mach Numbers From 1.79 to 2.67. NACA RM L58C27, 1958.
5. Carmel, Melvin M., Kelly, Thomas C., and Gregory, Donald T.: Aerodynamic Characteristics at Mach Numbers From 2.5 to 3.5 of a Canard Bomber Configuration Designed for Supersonic Cruise Flight. NACA RM L58G16, 1958.
6. Hallissy, Joseph M., Jr., and Hasson, Dennis F.: Aerodynamic Characteristics at Mach Numbers 2.36 and 2.87 of an Airplane Configuration Having a Cambered Arrow Wing With a 75° Swept Leading Edge. NACA RM L58E21, 1958.
7. Rainey, Robert W.: Investigation of the Effects of Bomb-Bay Configuration Upon the Aerodynamic Characteristics of a Body With Circular Cross Section at Supersonic Speeds. NACA RM L55E27, 1955.
8. Cole, J. D.: Newtonian Flow Theory for Slender Bodies. Jour. Aero. Sci., vol. 24, no. 6, June 1957, pp. 448-455.
9. Mueller, James N.: An Investigation of the Effect of Varying the Maximum Thickness Position Upon the Aerodynamic Characteristics of a Series of $3\frac{1}{2}$ -Percent-Thick Delta Wings. NACA RM L55D26, 1955.
10. Love, Eugene S.: Base Pressure at Supersonic Speeds on Two-Dimensional Airfoils and on Bodies of Revolution With and Without Fins Having Turbulent Boundary Layers. NACA TN 3819, 1957. (Supersedes NACA RM L53C02.)

11. Jackson, H. Herbert: Free-Flight Measurements of the Zero-Lift Drag of Several Wings at Mach Numbers From 1.4 to 3.8. NACA RM L56C13, 1956.
12. Baals, Donald D., Toll, Thomas A., and Morris, Owen G.: Airplane Configurations for Cruise at a Mach Number of 3. NACA RM L58E14a, 1958.
13. Spearman, M. Leroy: Some Factors Affecting the Static Longitudinal and Directional Stability Characteristics of Supersonic Aircraft Configurations. NACA RM L57E24a, 1957.
14. Van Driest, E. R.: Investigation of Laminar Boundary Layer in Compressible Fluids Using the Crocco Method. NACA TN 2597, 1952.
15. Van Driest, E. R.: Turbulent Boundary Layer in Compressible Fluids. Jour. Aero. Sci., vol. 18, no. 3, Mar. 1951, pp. 145-160, 216.

TABLE I.- DIMENSIONS OF MODELS

(a) Low-aspect-ratio arrow-wing configuration

Wing:	Wing	Altered ¹ wing
Area, sq in.	18.212	18.104
Span, in.	5.224	5.045
Root chord, in.	6.000	6.000
Tip chord, in.	1.308	1.251
Aspect ratio	1.498	1.405
Taper ratio	0.214	0.209
Mean aerodynamic chord, in.	4.156	4.150
Leading-edge sweep angle, deg	67.4	67.4
Trailing-edge sweep angle, deg	26.6	26.6
Airfoil section	Single wedge, flat lower surface	Single wedge, flat lower surface
Thickness chord ratio, percent	2	2
Location of maximum thickness	Trailing edge	Trailing edge
Tip fins:		
Area, sq in.		0.850
Height, in.		0.85
Root chord, in.		1.50
Tip chord, in.		0.50
Aspect ratio		0.85
Taper ratio		0.333
Leading-edge sweep angle, deg		66.97
Airfoil section		Flat plate, beveled leading edge
Thickness, in.		0.010
Nacelles:		
Length, in.		1.50
Diameter, in.		0.25
Wall thickness, in.		0.015
Fore-and-aft lips beveled externally		
Nacelle struts:		
Length, in.		0.60
Height, in.		0.100
Thickness, in.		0.010
Leading-edge sweep angle, deg		45
Trailing-edge sweep angle, deg		45

¹Wing altered to place tip fins at 0° toe-in.

TABLE I.- DIMENSIONS OF MODELS - Continued

(b) High-aspect-ratio arrow-wing configuration

Wing:	
Area, sq in.	15.90
Span, in.	6.00
Root chord, in.	4.50
Tip chord, in.	0.80
Aspect ratio	2.265
Taper ratio	0.178
Mean aerodynamic chord, in.	3.078
Leading-edge sweep angle, deg	67.4
Trailing-edge sweep angle, deg	49.4
Airfoil section	Single wedge, flat lower surface
Thickness chord ratio, percent chord	2
Location of maximum thickness	Wing trailing edge
Tip fins:	
Area, sq in.	0.56
Height, in.	0.80
Root chord, in.	1.10
Tip chord, in.	0.30
Aspect ratio	1.142
Taper ratio	0.273
Leading-edge sweep angle, deg	63.43
Airfoil section	Flat plate, beveled leading edge
Thickness, in.	0.010
Nacelles:	
Length, in.	1.50
Diameter, in.	0.25
Wall thickness, in.	0.015
Fore-and-aft lips beveled externally	
Nacelle struts:	
Length, in.	0.60
Height, in.	0.10
Thickness, in.	0.010
Leading-edge sweep angle, deg	45
Trailing-edge sweep angle, deg	45

TABLE I.- DIMENSIONS OF MODELS - Concluded

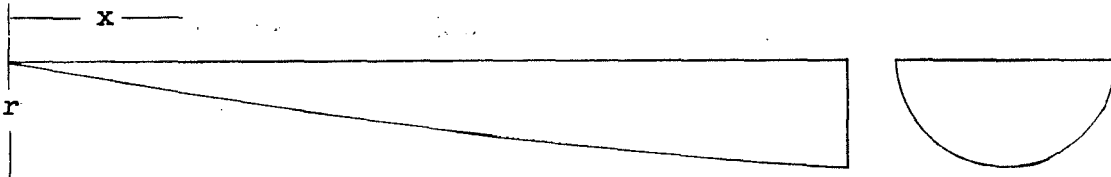
(c) Delta-wing configuration

Wing:			
Area, sq in.			18.750
Span, in.			7.50
Root chord, in.			5.00
Tip chord, in.			0
Aspect ratio			3
Taper ratio			0
Mean aerodynamic chord, in.			3.333
Leading-edge sweep angle, deg			53.15
Airfoil section		Symmetrical double wedge	
Thickness chord ratio, percent			2
Location of maximum thickness, percent chord			70
Tip fins:	Small	Large	
Area, sq in.	0.563		1.250
Height, in.	1.50		1.00
Root chord, in.	0.75		1.500
Tip chord, in.	0		1.00
Aspect ratio	0.40		0.800
Taper ratio	0		0.667
Leading-edge sweep angle, deg	45		45
Airfoil section	Flat plate, beveled leading edge	Flat plate, beveled leading edge	
Thickness, in.	0.010		0.010
Vertical tail:			
Area, sq in.			0.468
Height, in.			0.75
Root chord, in.			1.250
Tip chord, in.			0
Aspect ratio			1.21
Taper ratio			0
Leading-edge sweep angle, deg			53.13
Airfoil section		Flat plate, beveled leading edge	
Thickness, in.			0.010
Nacelles:			
Length, in.			1.50
Diameter, in.			0.25
Wall thickness, in.			0.015
Fore-and-aft lips beveled externally			
Nacelle struts:			
Length, in.			0.60
Height, in.			0.10
Thickness, in.			0.010
Leading-edge sweep angle, deg			45
Trailing-edge sweep angle, deg			45

L-183



TABLE II.- ORDINATES FOR 2/3-POWER HALF-BODY FUSELAGES



Arrow-wing configurations				Delta-wing configurations			
Low aspect ratio		High aspect ratio		Short		Long	
x, in.	r, in.	x, in.	r, in.	x, in.	r, in.	x, in.	r, in.
0	0	0	0	0	0	0	0
.305	.0466	.225	.0506	.250	.0522	.350	.0441
.610	.0739	.450	.0803	.500	.0829	.700	.0700
.915	.0969	.675	.1052	.750	.1086	1.050	.0918
1.220	.1173	.900	.1275	1.000	.1316	1.400	.1112
1.525	.1362	1.125	.1479	1.250	.1527	1.750	.1290
1.830	.1538	1.350	.1670	1.500	.1724	2.100	.1457
2.135	.1704	1.575	.1851	1.750	.1911	2.450	.1615
2.440	.1863	1.800	.2024	2.000	.2089	2.800	.1765
2.745	.2015	2.025	.2189	2.250	.2260	3.150	.1909
3.050	.2161	2.250	.2349	2.500	.2464	3.500	.2048
3.355	.2303	2.475	.2503	2.750	.2583	3.850	.2182
3.660	.2441	2.700	.2652	3.000	.2737	4.200	.2313
3.965	.2575	2.925	.2797	3.250	.2887	4.550	.2440
4.270	.2705	3.150	.2939	3.500	.3034	4.900	.2563
4.575	.2832	3.375	.3077	3.750	.3176	5.250	.2684
4.880	.2957	3.600	.3213	4.000	.3316	5.600	.2802
5.185	.3079	3.825	.3345	4.250	.3453	5.950	.2917
5.490	.3198	4.050	.3475	4.500	.3587	6.300	.3031
5.795	.3316	4.275	.3603	4.750	.3719	6.650	.3142
6.100	.3431	4.500	.3728	5.000	.3848	7.000	.3251

TABLE III.- SUMMARY OF RESULTS

(a) Low-aspect-ratio arrow wing

Configuration designation	Test	$C_{D,min}$	$\left(\frac{L}{D}\right)_{max}$	$C_{L,opt}$	$\frac{dC_L}{d\alpha}$	$\frac{dC_m}{d\alpha}$	$\frac{dC_m}{dC_L}$	$\frac{dC_Y}{d\beta}$	$\frac{dC_n}{d\beta}$	$\frac{dC_n}{dC_Y}$	R
BW ₁ N ₆ ^F _{1,5}	Pitch	0.0100	5.88	0.115	0.0258	-0.0016	-0.0800	-----	-----	-----	0.862 × 10 ⁶
BW ₁ N ₄ ^F _{1,5}	Pitch	.0098	5.90	.114	.0248	-.0024	-.0900	-----	-----	-----	.871
BW ₁ N ₂ ^F _{1,5}	Pitch	.0085	6.29	.103	.0249	-.0018	-.0765	-----	-----	-----	.862
BW ₁ ^F _{1,5}	Pitch	.0075	6.71	.103	.0253	-.0021	-.0825	-----	-----	-----	.851
BW ₁ N ₆ ^F _{1,5}	Yaw	.0095	----	-----	-----	-----	-----	-0.0037	0.0012	-0.3125	.831
BW ₁ N ₆	Yaw	.0095	----	-----	-----	-----	-----	-.0019	.0003	-.1650	.819
BW ₁ N ₆	Pitch	.0092	5.95	.118	.0254	-.0014	-.0537	-----	-----	-----	.859
BW ₁ N ₆ ^F _{1,0}	Pitch	.0098	5.68	.112	.0257	-.0028	-.1000	-----	-----	-----	.869
BW ₁ N ₆ ^F _{1,0}	Yaw	.0100	----	-----	-----	-----	-----	-.0035	.0011	-.3000	.872
B ['] W ₁ N ₆ ^F _{1,0}	Pitch	.0104	5.71	.118	.0262	-.0023	-.0800	-----	-----	-----	.862
BW ₁ N ₆ ^F _{1,0}	Pitch	Wing base-pressure measurements									.825
											1.600
											3.06
BW ₁ N ₆ ^F _{1,0}	Pitch	Wing base-pressure measurements									.825
											1.600
											3.06
B ₁ W ₁ N ₄ ^F _{1,0} (FT)	Pitch	Body base-pressure measurements									.879
BWN ₆ ^F _{1,0}	Pitch	Nacelle pressure measurements									.840
											2.76
B ₁ W ₁ N ₆ ^F _{1,0} (FT)	Pitch	.0130	5.23	.125	.0252	-.0016	-.0525	-----	-----	-----	1.645
B ₁ W ₁ N ₆ ^F _{1,0}	Pitch	.0110	5.40	.1295	.0249	-.0018	-.0644	-----	-----	-----	1.652
B ₁ W ₁ N ₆ ^F _{1,0} (FT)	Yaw	.0131	----	-----	-----	-----	-----	-.0035	.0011	-.3375	1.657
B ₁ W ₁ N ₆ ^F _{1,0}	Yaw	.0120	----	-----	-----	-----	-----	-.0036	.0013	-.3475	1.625
B ₁ W ₁ N ₆ ^F _{1,0}	Pitch	.0117	5.25	.124	.0260	-.00156	-.0570	-----	-----	-----	.875
B ₁ W ₁ N ₆ ^F _{1,0}	Pitch	.0111	5.46	.124	.0254	-.0010	-.0600	-----	-----	-----	1.655
B ₁ W ₁ N ₄ ^F _{1,0}	Pitch	.0102	5.60	.124	.0258	-.0018	-.0625	-----	-----	-----	1.632
BW ₁ N ₆ ^F _{1,0} (FT)	Pitch	.0125	5.22	.129	.0256	-.0017	-.0708	-----	-----	-----	.891
BW ₁ N ₆ ^F _{1,0} (FT)	Pitch	.0120	5.32	.136	.0254	-.0018	-.0800	-----	-----	-----	1.705
BW ₁ N ₆ ^F _{1,0}	Pitch	.0113	5.42	.128	.0256	-.0018	-.0694	-----	-----	-----	.857
BW ₁ N ₆ ^F _{1,0}	Pitch	.0103	5.58	.131	.0254	-.0018	-.0740	-----	-----	-----	1.623
BW ₁ N ₆ ^F _{1,0} (FT)	Yaw	.0125	----	-----	-----	-----	-----	-.0037	.0013	-----	1.634
BW ₁ N ₆ ^F _{1,0}	Yaw	.0107	----	-----	-----	-----	-----	-.0037	.0012	-.3278	1.663
BW ₁ N ₆ ^F _{1,0} (FT)	Pitch	.0120	5.30	.133	.0257	-.0020	-.0784	-----	-----	-----	1.637
BW ₁ N ₆ ^F _{1,0}	Pitch	.0104	5.47	.133	.0260	-.0020	-.0811	-----	-----	-----	1.630
B ₁ W ₁ N ₆ ^F _{1,0} (Canted nose)	Pitch	.0108	5.53	.107	.0248	-.0020	-.0787	-----	-----	-----	1.580

I-183

TABLE III.- SUMMARY OF RESULTS - Concluded

(b) High-aspect-ratio arrow wing

Configuration designation	Test	$C_{D,min}$	$\left(\frac{L}{D}\right)_{max}$	$C_{L,opt}$	$\frac{dC_L}{d\alpha}$	$\frac{dC_m}{d\alpha}$	$\frac{dC_m}{dC_L}$	$\frac{dC_Y}{d\beta}$	$\frac{dC_n}{d\beta}$	$\frac{dC_n}{dC_Y}$	R
$B_2W_2N_6F_{2,0}$	Yaw	0.0112	----	-----	-----	-----	-----	0.00348	0.0008	-0.2200	1.232×10^6
$B_2W_2N_6F_{2,0}$ (FT)	Pitch	.0140	5.11	0.150	0.0259	0.0010	0.0445	-----	-----	-----	1.234
$B_2W_2N_6F_{2,0}$ (FT)	Pitch	.0141	5.30	.140	.0264	.00128	.055	-----	-----	-----	1.206
$B_2W_2N_6F_{2,0}$ (FT)	Pitch	.0137	5.25	.146	.0276	.0009	.055	-----	-----	-----	.628
$B_2W_2N_6F_{2,0}$	Pitch	.0115	5.45	.150	.0276	.0009	.0325	-----	-----	-----	.637
$B_2W_2N_6F_{2,0}$	Pitch	.0110	5.55	.135	.0264	.0011	.055	-----	-----	-----	1.228

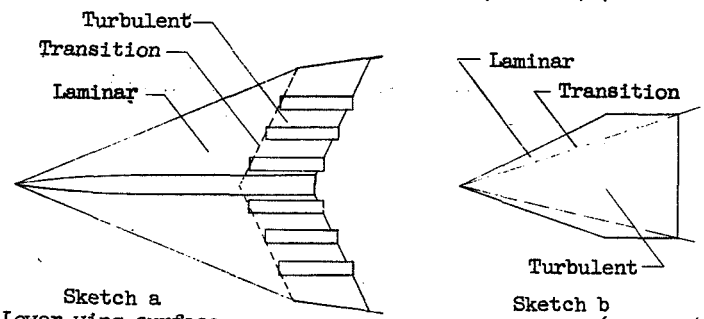
(c) Delta wing

$B_3W_3N_6$ (FT)	Pitch	0.0102	5.98	0.122	0.0269	0.00104	0.0375	-----	-----	-----	1.334×10^6
$B_3W_3N_6$ (FT)	Pitch	.0095	6.15	.115	.0270	.0009	.0445	-----	-----	-----	.688
$B_3W_3N_6$ (FT)	Yaw	.0098	----	-----	-----	-----	-----	-0.0029	0.000135	-0.0450	1.329
$B_3W_3N_6$	Yaw	.0078	----	-----	-----	-----	-----	.0024	.000125	-.0450	1.309
$B_3W_3N_6$	Pitch	.0077	6.98	.110	.0261	.0008	.0300	-----	-----	-----	1.325
B_3W_3	Pitch	.0053	8.42	.094	.0258	.0012	.0460	-----	-----	-----	1.308
$B_3W_3N_6FL$	Pitch	.0090	6.40	.112	.0266	.0015	.0640	-----	-----	-----	1.325
$B_3W_3N_6FL$	Yaw	.0093	----	-----	-----	-----	-----	-.0056	.0007	-.1271	1.312
$B_3W_3N_6FS$	Pitch	.0093	6.13	.120	.0260	.0010	.0400	-----	-----	-----	1.338
$B_3W_3N_6FS$	Yaw	.0101	----	-----	-----	-----	-----	-.0036	.00039	-.1025	1.333
$B_3W_3N_6V$	Pitch	.0080	6.79	.102	.0262	.0009	.0340	-----	-----	-----	1.352
$B_3W_3N_6V$	Yaw	.0080	----	-----	-----	-----	-----	-.0029	.00021	-.0625	1.340
$B_{ext}W_3N_6V$ (FT)	Yaw	.0109	----	-----	-----	-----	-----	-.0027	.0003	-.0850	1.286
$B_{ext}W_3N_6V$	Yaw	.0081	----	-----	-----	-----	-----	-.0027	.0002	-.0710	1.303
$B_{ext}W_3N_6V$ (FT)	Pitch	.0107	5.75	.1345	.0259	.0003	.0215	-----	-----	-----	1.295
$B_{ext}W_3N_6V$	Pitch	.0080	6.30	.103	.0258	.00055	.0224	-----	-----	-----	1.284
$B_{ext}W_3N_6V$ (FT)	Pitch	.0110	5.71	.133	.0259	.0006	.0279	-----	-----	-----	1.323
$B_3W_3N_6V$ (FT)	Pitch	.0105	5.70	.125	.0258	.00055	.01125	-----	-----	-----	1.323
$B_3W_3N_4V$ (FT)	Pitch	.0100	5.90	.120	.0256	.00075	.0294	-----	-----	-----	1.315
$B_3W_3N_2V$ (FT)	Pitch	.0092	6.13	.112	.0253	.0007	.0320	-----	-----	-----	1.361
B_3W_3V (FT)	Pitch	.0080	6.75	.107	.0255	.00076	.0320	-----	-----	-----	1.370
B_3W_3 (FT)	Pitch	.0079	6.81	.106	.0256	.00065	.0332	-----	-----	-----	1.369
B_3W_3	Pitch	.0055	8.11	.090	.0251	.00086	.0333	-----	-----	-----	1.368
$B_{inv}W_3N_6V_{inv}$ (FT)	Pitch	.0110	5.50	.124	.0258	.0008	.0350	-----	-----	-----	1.326
$B_{inv}W_3N_6V_{inv}$	Pitch	.0080	6.25	.1135	.0257	.0008	.0350	-----	-----	-----	1.292
$B_3W_3N_6,invV$ (FT)	Pitch	.0110	5.80	.124	.0260	.000875	.0310	-----	-----	-----	1.323
$B_3W_3N_6,invV$	Pitch	.0081	6.60	.109	.0255	.00097	.0393	-----	-----	-----	1.317

TABLE IV.- SUMMARY OF ESTIMATED AERODYNAMIC CHARACTERISTICS

[Natural transition]

(a) Low-aspect-ratio arrow wing (BW₁N6F_{1,5})



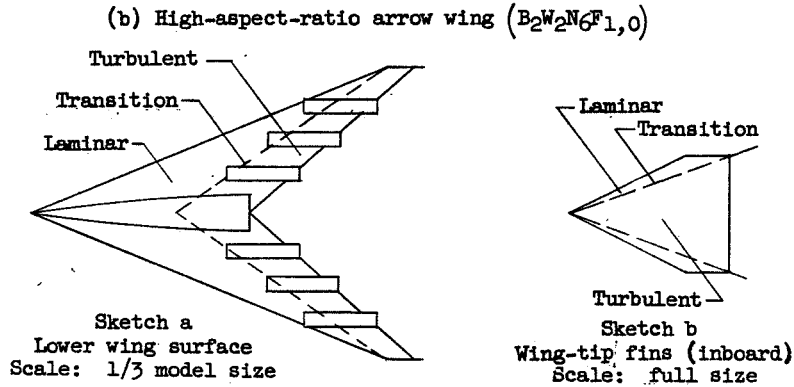
Sketch a
Lower wing surface
Scale: 1/3 model size

Sketch b
Wing-tip fins (inboard)
Scale: full size

Skin-friction drag ¹		
Component	Boundary layer	C _{D,F}
Wing -		
Upper surface	Laminar	0.0012
Lower surface (see sketch a)	Laminar and turbulent	.0016
Struts	Turbulent	.0002
Nacelles	Turbulent	.0015
Tip fins (see sketch b)	Laminar and turbulent	.0004
Nacelle internal friction	Laminar	.0009
Body	Laminar and turbulent	.0007
Total		0.0065
Pressure drag		
Component		C _{D,p}
Wing		0.0025
Body0002
Nacelle0004
Struts0001
Tip fins0001
Nacelle internal pressure drag0006
Total		0.0039
$C_{D,0} = C_{D,F} + C_{D,p} = 0.0104;$ $C_{L\alpha} = 1.4637/\text{radians};$ $C_D/C_L^2 = 0.6832 \text{ radian}.$		

¹Laminar values determined from reference 14; turbulent values, from reference 15.

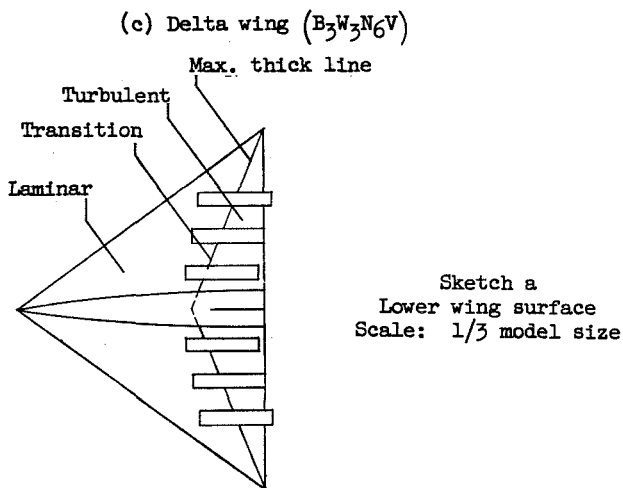
TABLE IV.- SUMMARY OF ESTIMATED AERODYNAMIC CHARACTERISTICS - Continued



Skin-friction drag ¹		
Component	Boundary layer	$C_{D,F}$
Wing - Upper surface	Laminar	0.0012
Lower surface (see sketch a)	Laminar and turbulent	.0016
Struts	Turbulent	.0002
Nacelles	Turbulent	.0015
Tip fins (see sketch b)	Laminar and turbulent	.0004
Nacelle internal friction	Laminar	.0009
Body	Laminar and turbulent	.0004
Total		0.0062
Pressure drag		
Component		$C_{D,p}$
Wing		0.0028
Body0007
Nacelles0004
Struts0001
Tip fins0001
Nacelle internal pressure drag0006
Base0003
Total		0.0050
$C_{D,0} = C_{D,F} + C_{D,p} = 0.0112;$ $C_{L_w} = 1.4637/\text{radians};$ $C_D/C_L^2 = 0.6832 \text{ radian}.$		

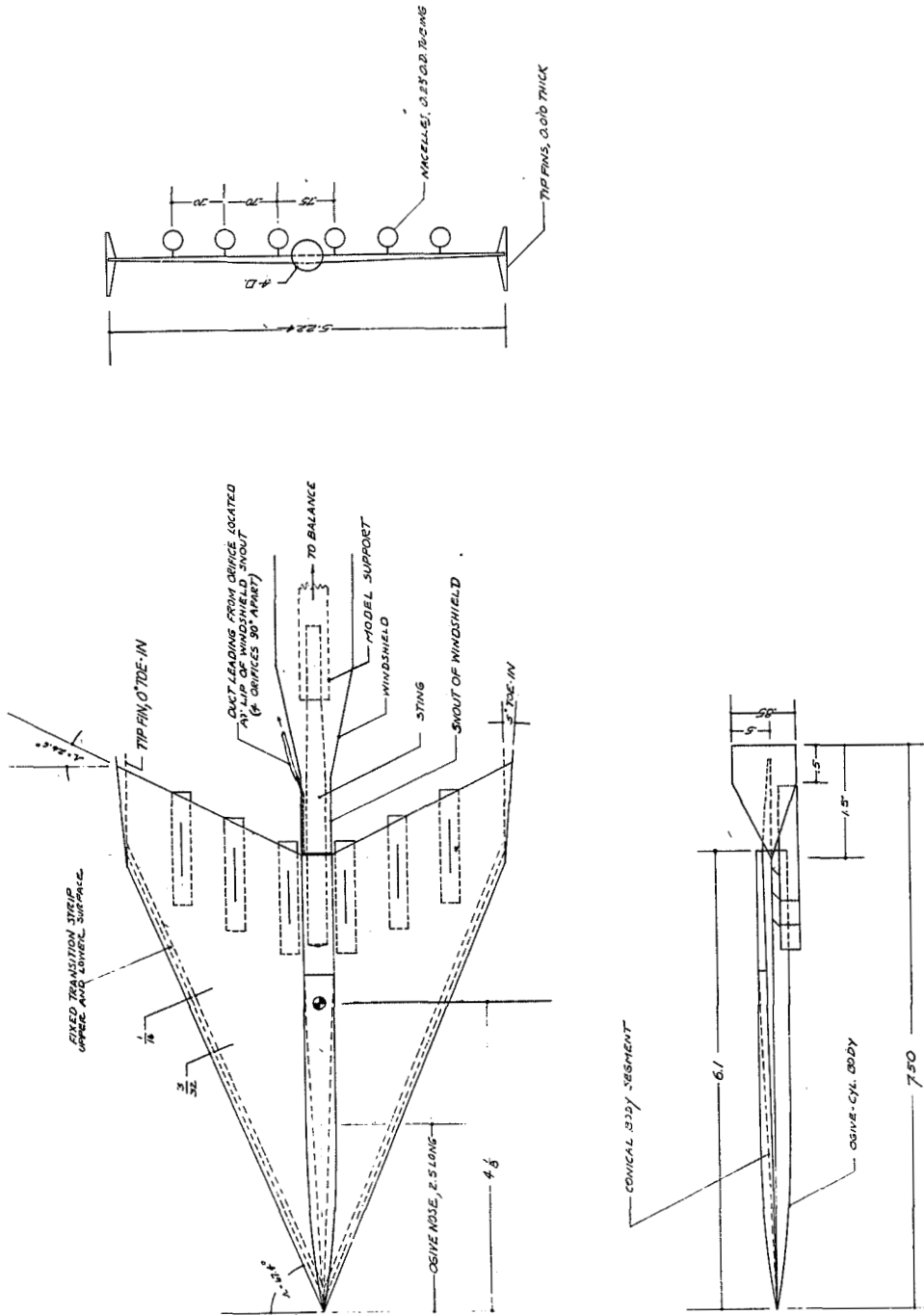
¹Laminar values determined from reference 14; turbulent values, from reference 15.

TABLE IV.- SUMMARY OF ESTIMATED AERODYNAMIC CHARACTERISTICS - Concluded



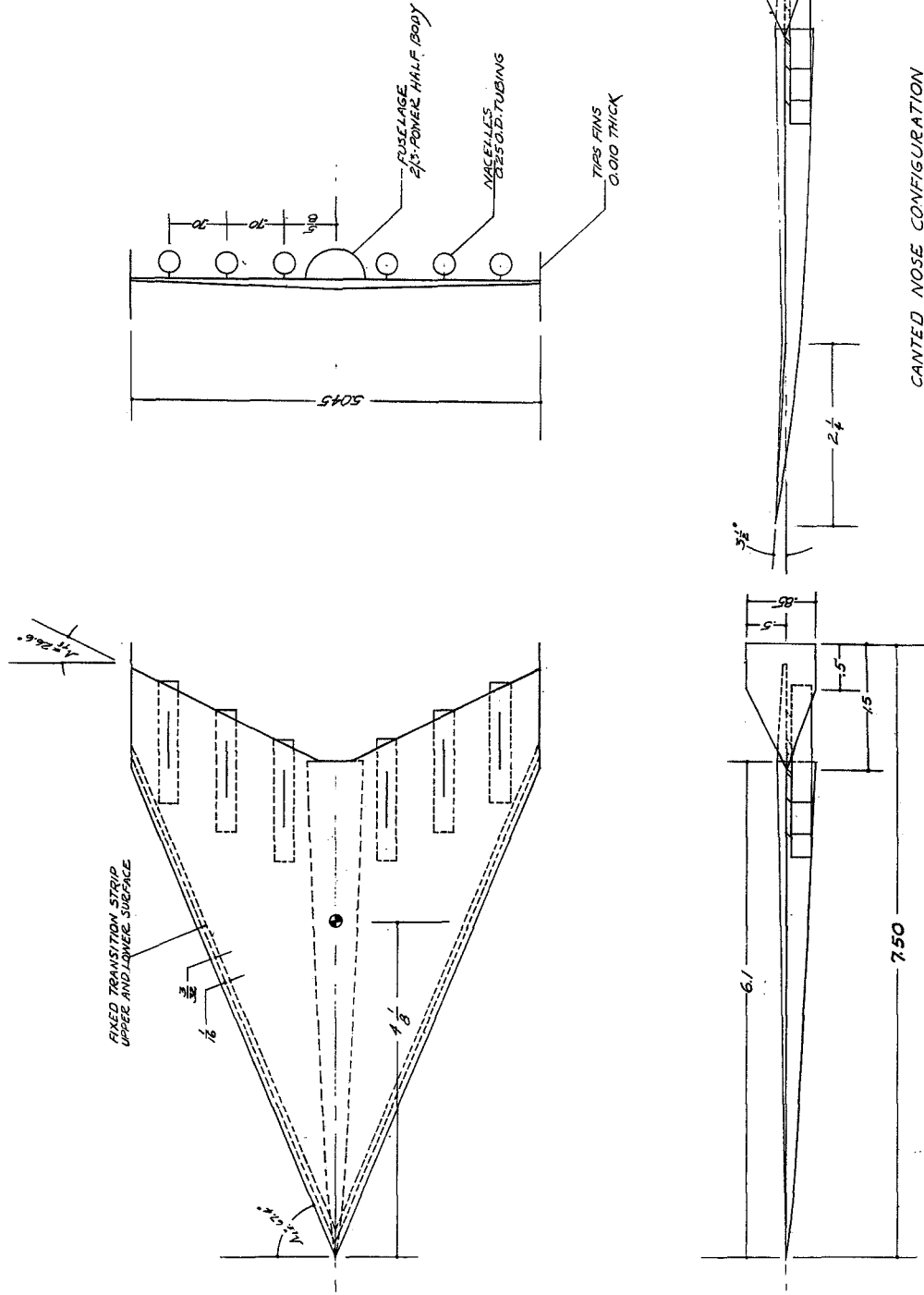
Skin-friction drag ¹		
Component	Boundary layer	C _{D,F}
Wing - Upper surface	Laminar	0.0012
Lower surface (see sketch a)	Laminar and turbulent	.0013
Struts	Turbulent	.0002
Nacelles	Turbulent	.0012
Vertical tail	Laminar	.0001
Nacelle internal friction	Laminar	.0006
Body	Laminar and turbulent	.0003
Total		0.0049
Pressure drag		
Component		C _{D,p}
Wing		0.0010
Body0006
Nacelles0004
Struts0001
Vertical tail0001
Nacelle internal pressure drag0006
Base0003
Total		0.0031
$C_{D,0} = C_{D,F} + C_{D,p} = 0.0080;$ $C_{L\alpha} = 1.4637/\text{radians};$ $C_D/C_L^2 = 0.6832 \text{ radian.}$		

¹Laminar values determined from reference 14; turbulent values, from reference 15.



(a) Ogive-cylinder body configuration.

Figure 1.- Three-view drawing of low-aspect-ratio arrow wing. All dimensions are in inches unless otherwise noted.



(b) 2/3-power half-body configuration.

Figure 1.- Concluded.

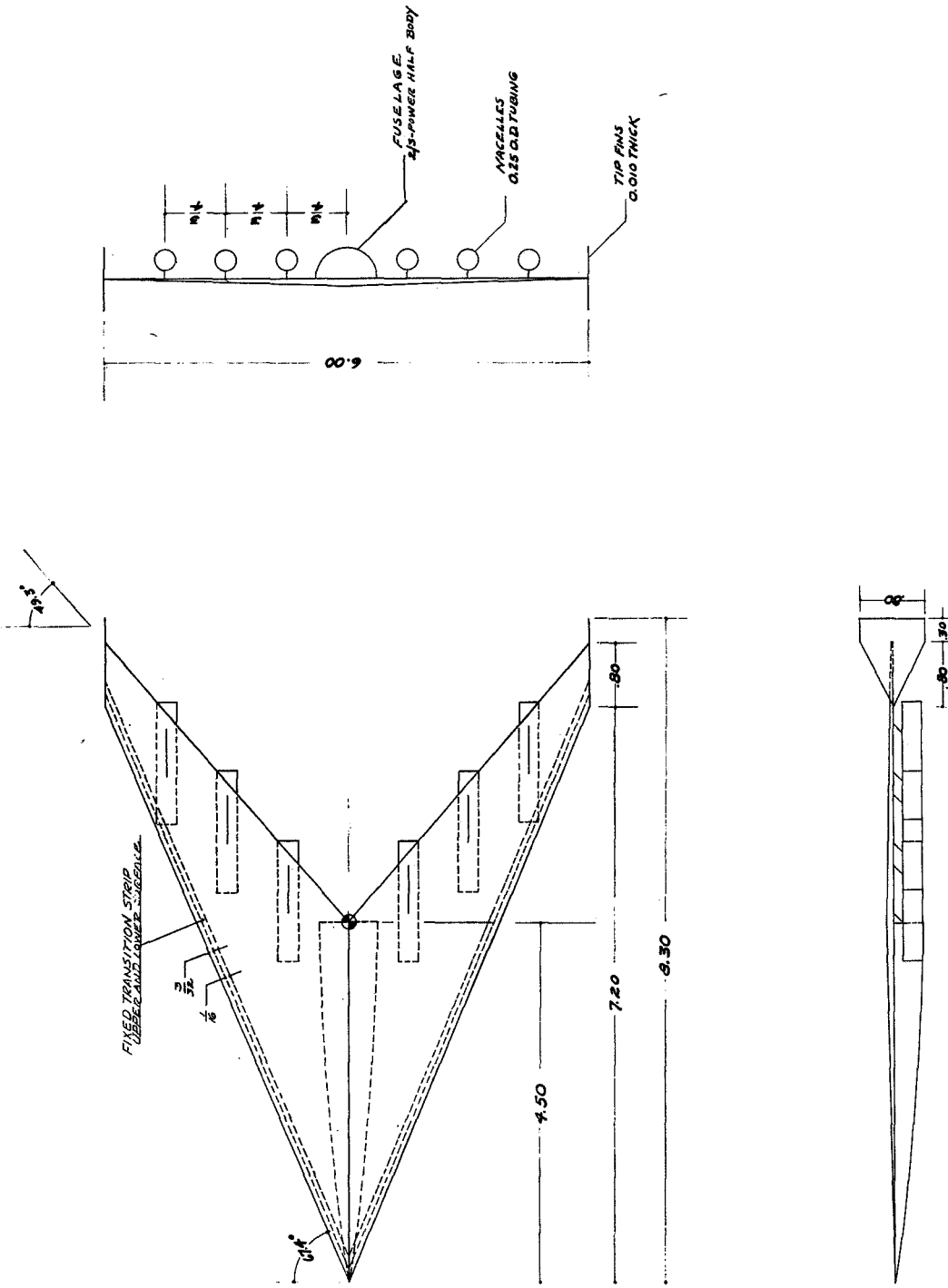
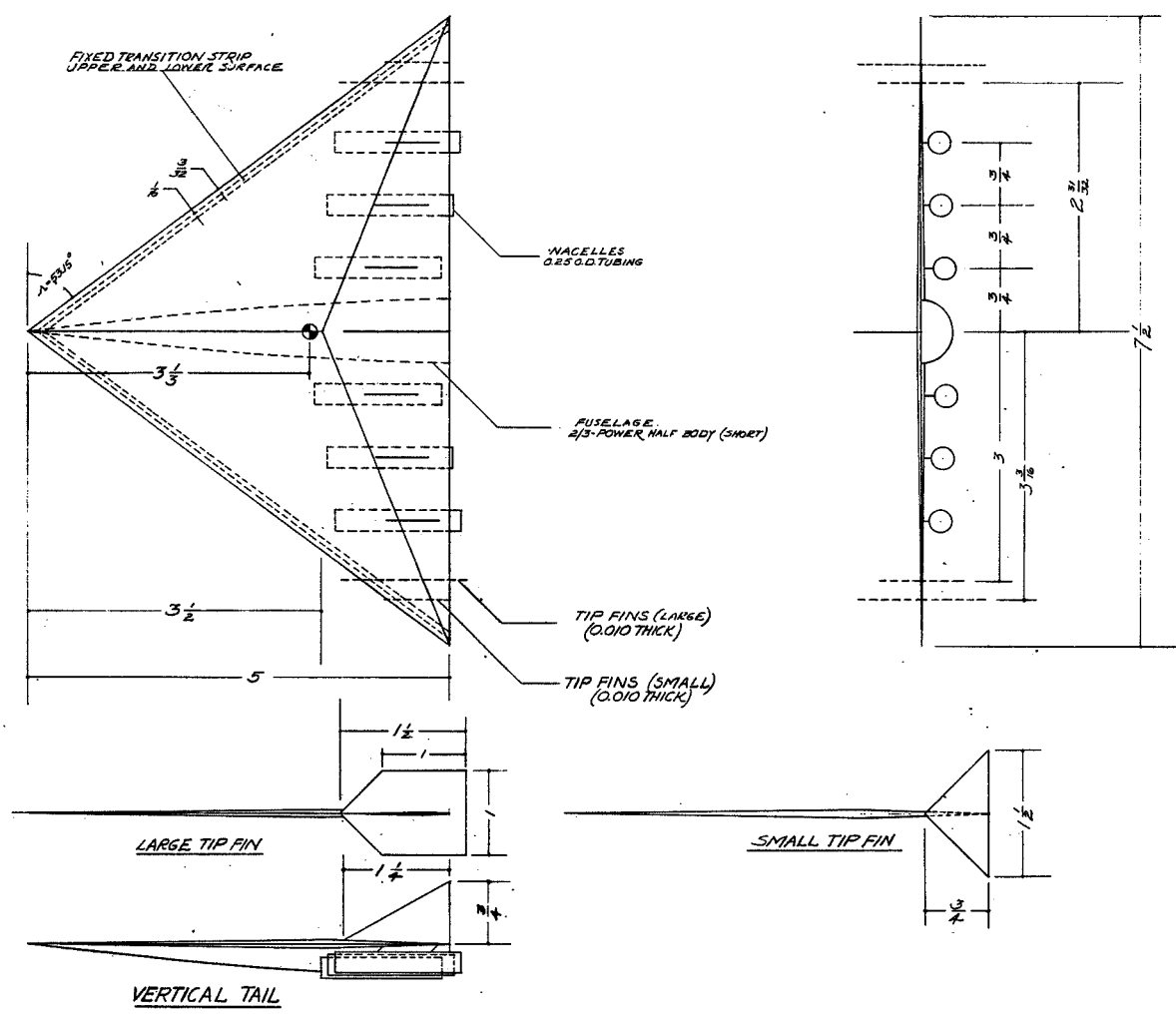


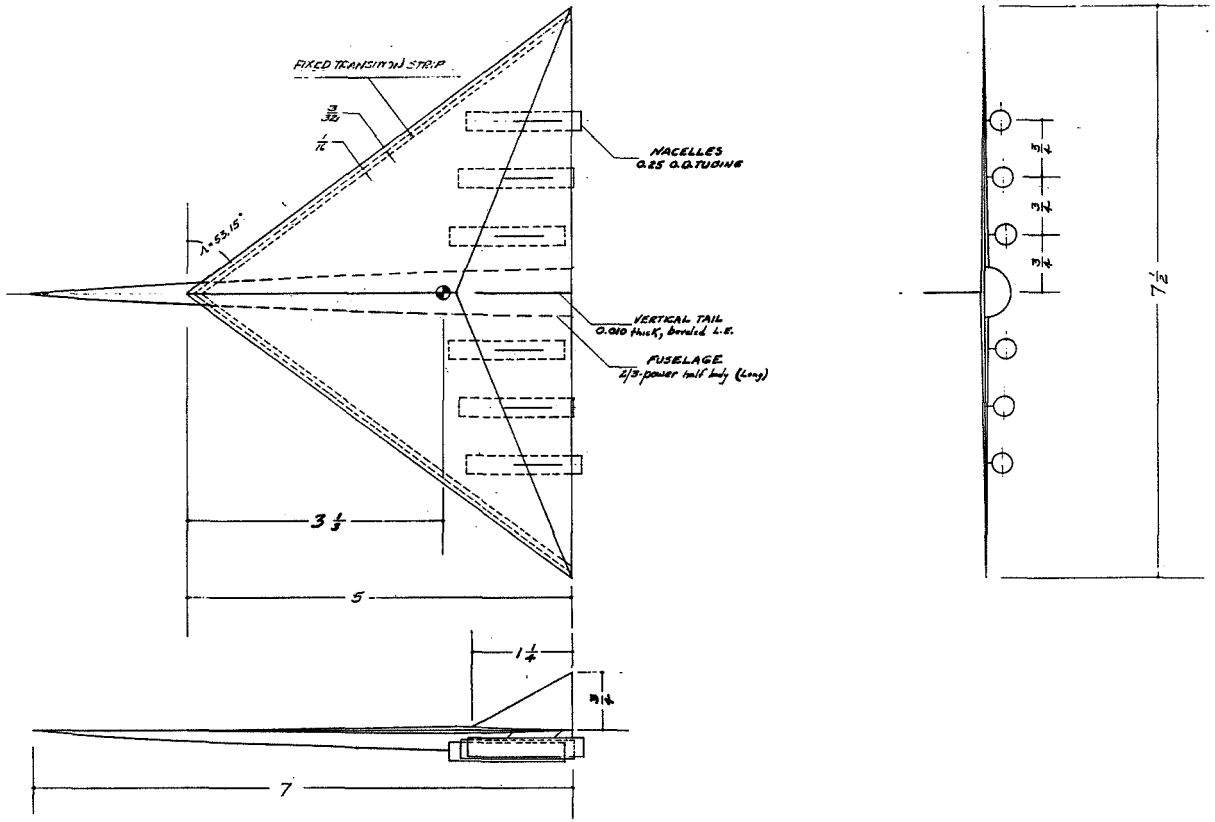
Figure 2.- Three-view drawing of high-aspect-ratio arrow wing. All dimensions are in inches unless otherwise noted.

L-183

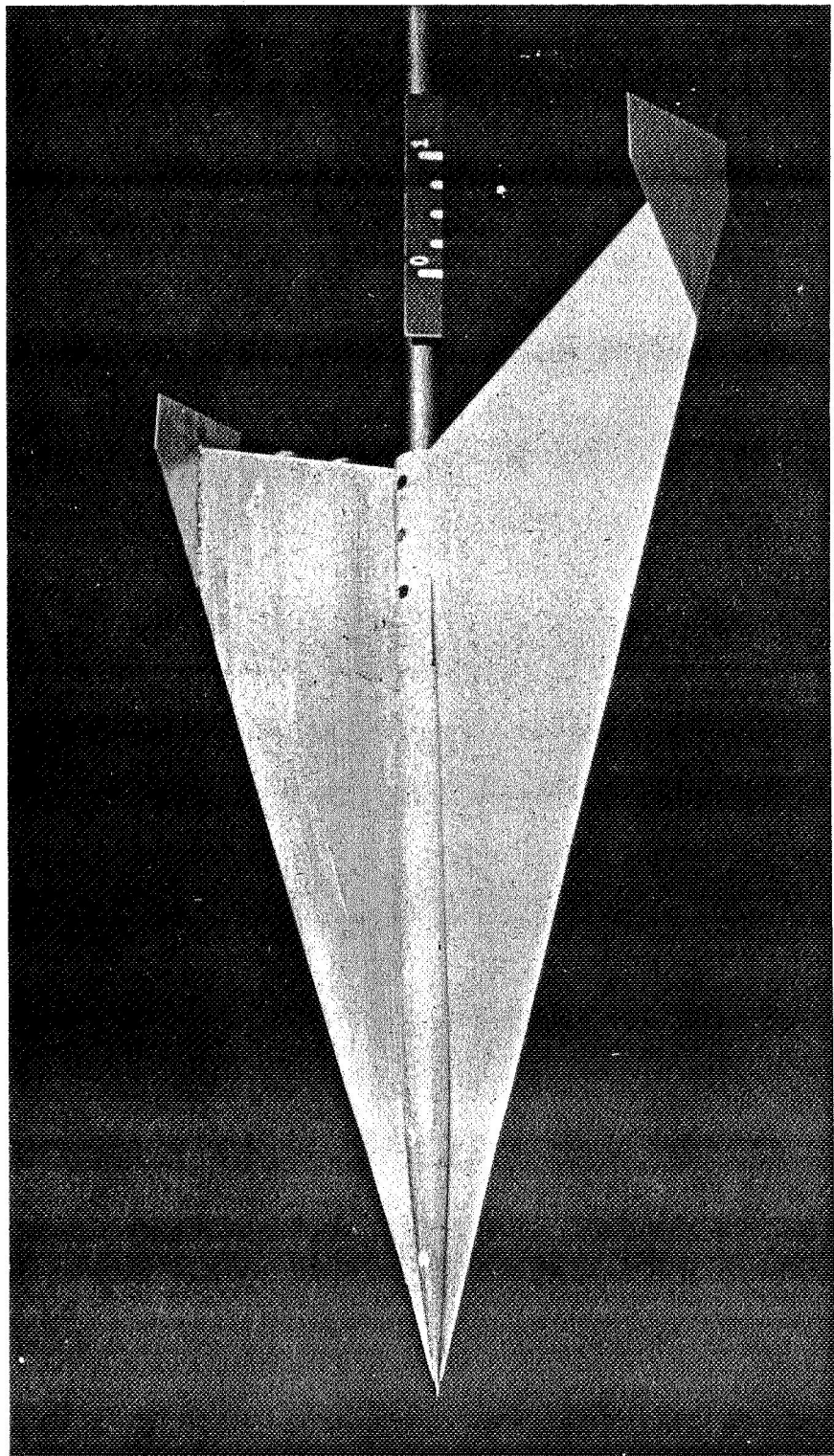


(a) Normal-length body configuration.

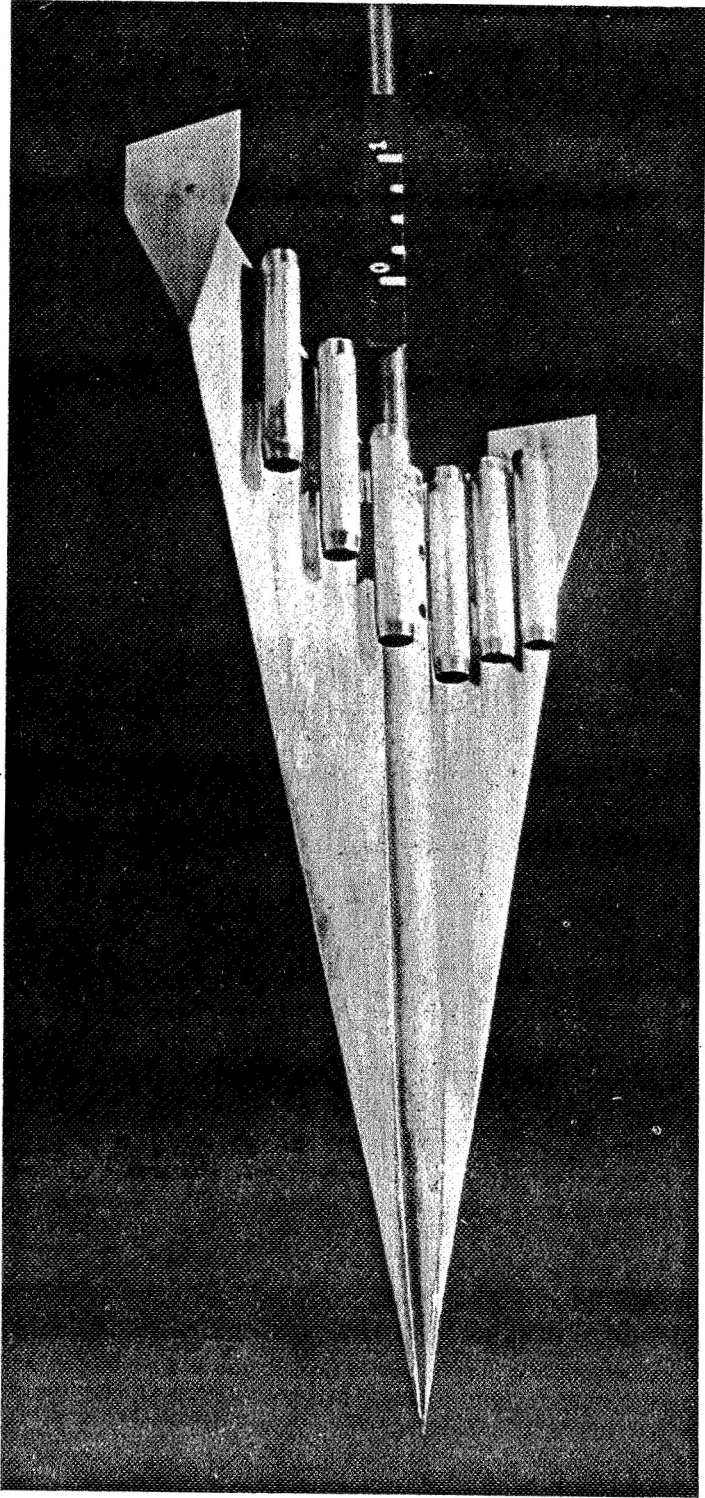
Figure 3.- Three-view drawing of delta wing. All dimensions are in inches unless otherwise noted.



(b) Long body configuration.
Figure 3.- Concluded.

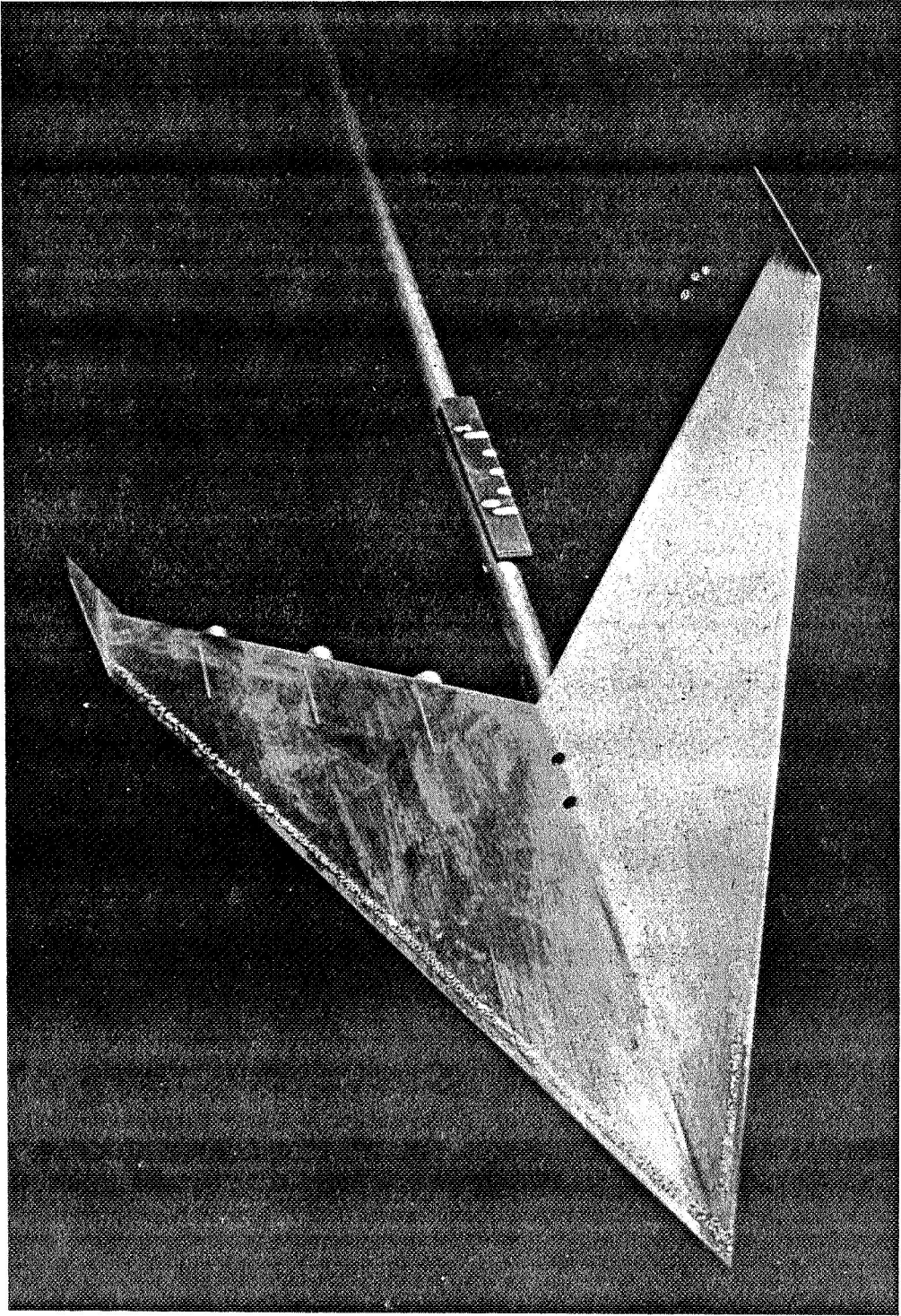


(a) Three-quarter front top view. L-58-678
Figure 4.- Photographs of low-aspect-ratio arrow wing. (Ogive-cylinder body.)



(b) Three-quarter front bottom view. L-58-679

Figure 4.- Concluded.

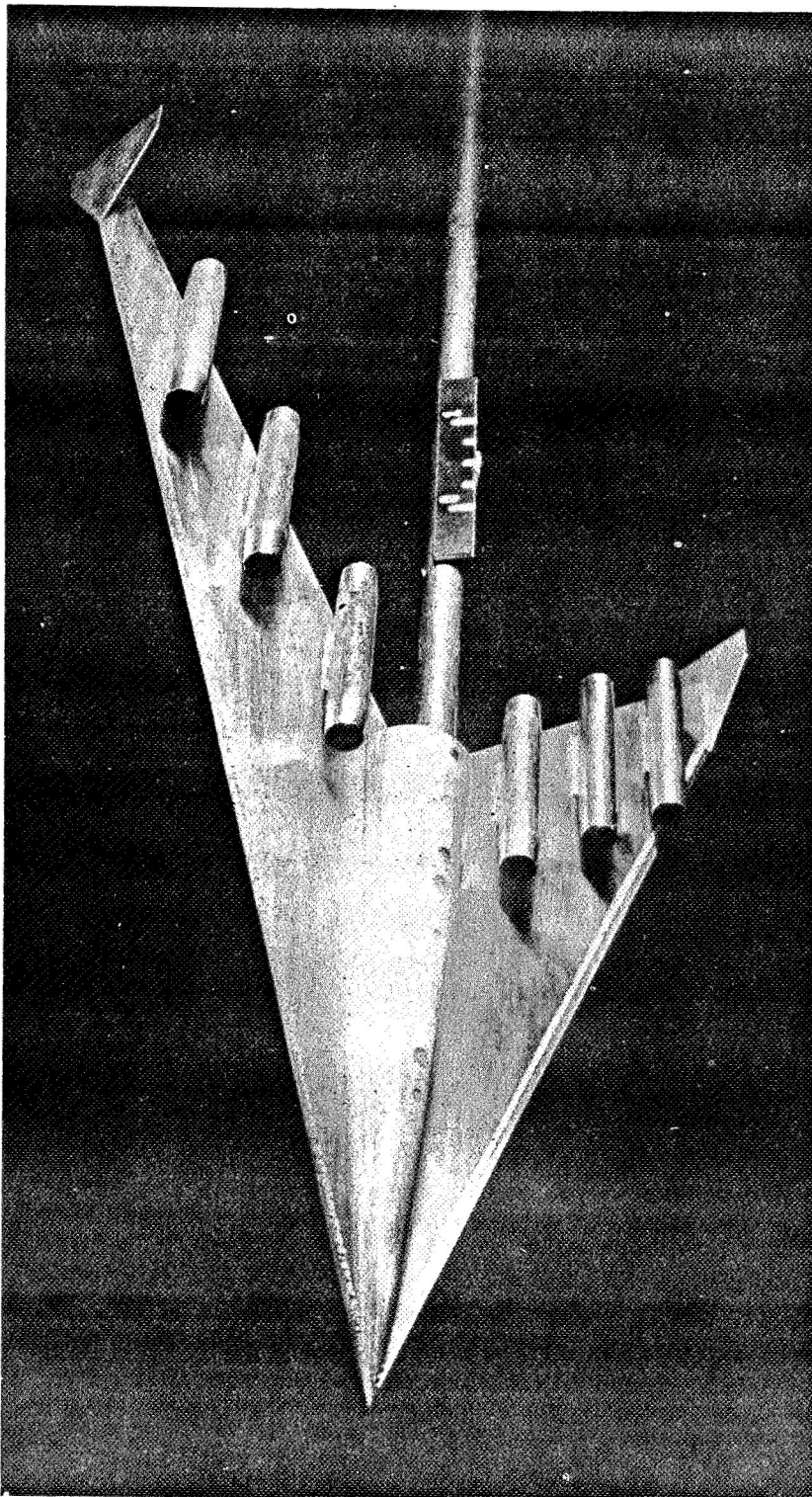


(a) Three-quarter front top view. L-58-1241

Figure 5.- Photographs of high-aspect-ratio arrow wing.

CONFIDENTIAL

CONFIDENTIAL



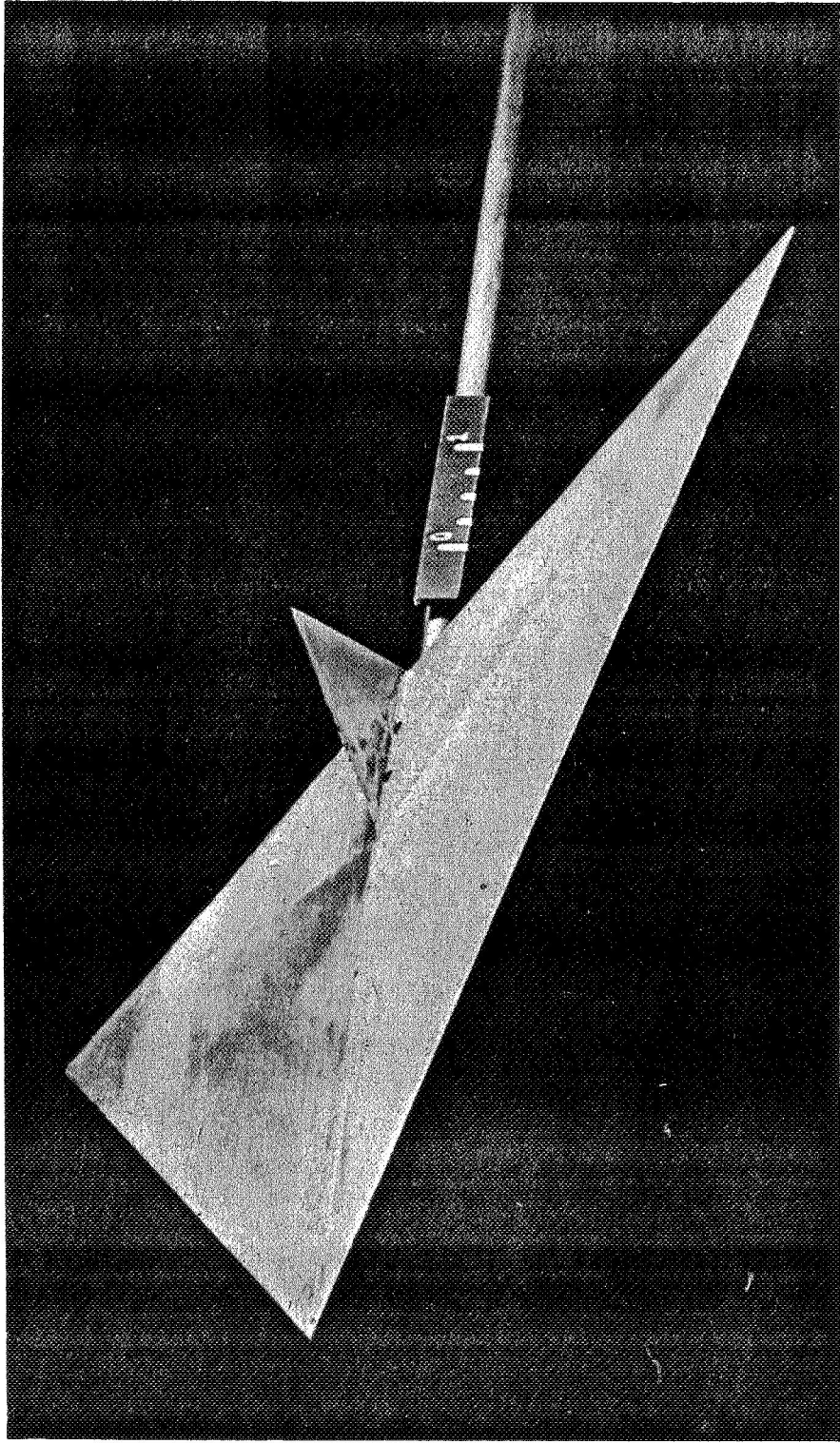
(b) Three-quarter front bottom view. L-58-1242

Figure 5.- Concluded.

3 3 3
3 3 3
3 3 3
3 3 3
3 3 3
3 3 3
3 3 3
3 3 3
3 3 3
3 3 3
3 3 3
3 3 3
3 3 3
3 3 3
3 3 3
3 3 3
3 3 3
3 3 3
3 3 3
3 3 3
3 3 3



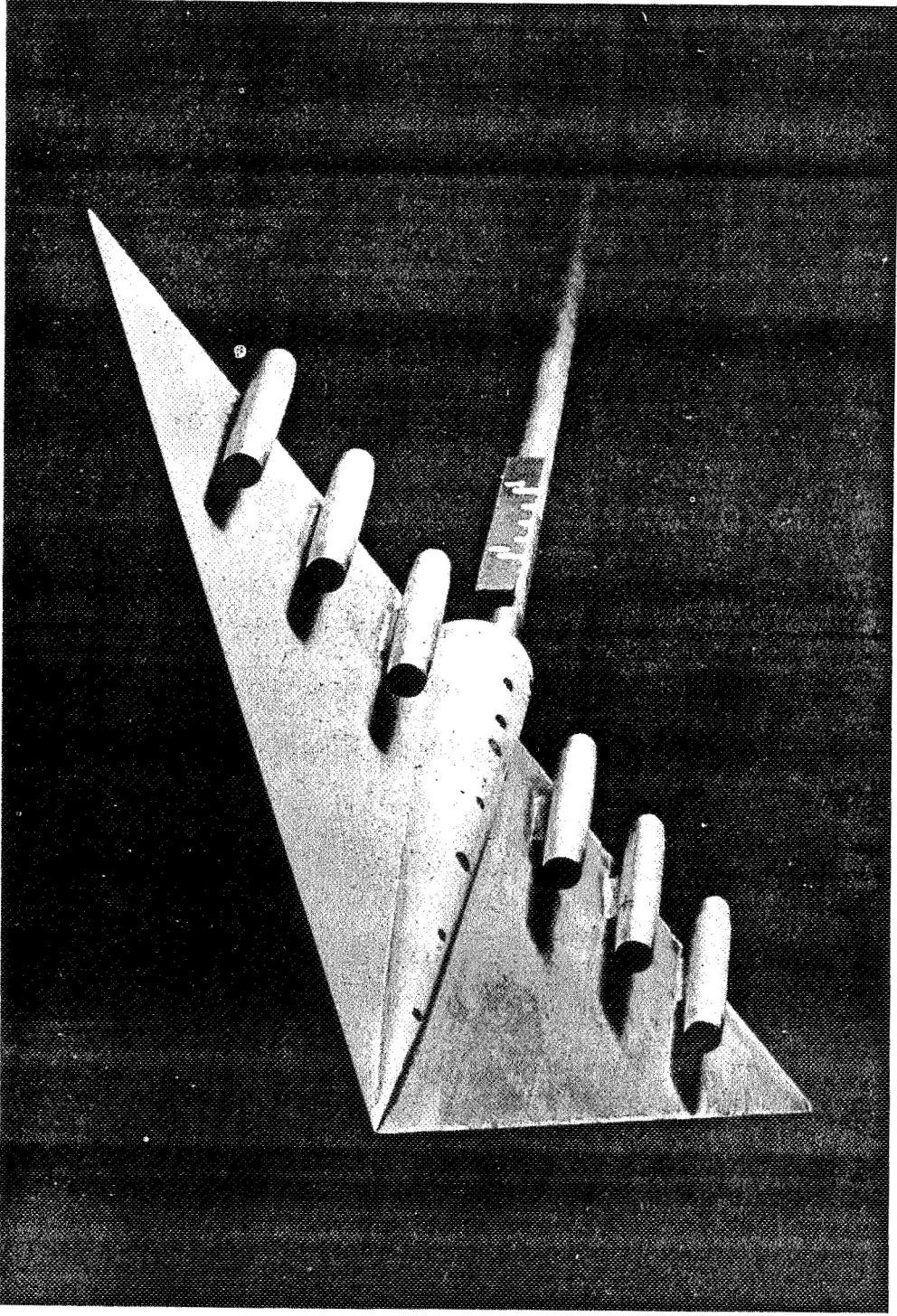
L-185



(a) Three-quarter front top view. L-58-903

Figure 6.- Photographs of delta wing. (Short body.)

33393
33392
33391
33390
33389
33388
33387
33386
33385
33384
33383
33382
33381
33380
33379
33378
33377
33376
33375
33374
33373
33372
33371
33370
33369
33368
33367
33366
33365
33364
33363
33362
33361
33360
33359
33358
33357
33356
33355
33354
33353
33352
33351
33350
33349
33348
33347
33346
33345
33344
33343
33342
33341
33340
33339
33338
33337
33336
33335
33334
33333
33332
33331
33330
33329
33328
33327
33326
33325
33324
33323
33322
33321
33320
33319
33318
33317
33316
33315
33314
33313
33312
33311
33310
33309
33308
33307
33306
33305
33304
33303
33302
33301
33300
33299
33298
33297
33296
33295
33294
33293
33292
33291
33290
33289
33288
33287
33286
33285
33284
33283
33282
33281
33280
33279
33278
33277
33276
33275
33274
33273
33272
33271
33270
33269
33268
33267
33266
33265
33264
33263
33262
33261
33260
33259
33258
33257
33256
33255
33254
33253
33252
33251
33250
33249
33248
33247
33246
33245
33244
33243
33242
33241
33240
33239
33238
33237
33236
33235
33234
33233
33232
33231
33230
33229
33228
33227
33226
33225
33224
33223
33222
33221
33220
33219
33218
33217
33216
33215
33214
33213
33212
33211
33210
33209
33208
33207
33206
33205
33204
33203
33202
33201
33200
33199
33198
33197
33196
33195
33194
33193
33192
33191
33190
33189
33188
33187
33186
33185
33184
33183
33182
33181
33180
33179
33178
33177
33176
33175
33174
33173
33172
33171
33170
33169
33168
33167
33166
33165
33164
33163
33162
33161
33160
33159
33158
33157
33156
33155
33154
33153
33152
33151
33150
33149
33148
33147
33146
33145
33144
33143
33142
33141
33140
33139
33138
33137
33136
33135
33134
33133
33132
33131
33130
33129
33128
33127
33126
33125
33124
33123
33122
33121
33120
33119
33118
33117
33116
33115
33114
33113
33112
33111
33110
33109
33108
33107
33106
33105
33104
33103
33102
33101
33100
33099
33098
33097
33096
33095
33094
33093
33092
33091
33090
33089
33088
33087
33086
33085
33084
33083
33082
33081
33080
33079
33078
33077
33076
33075
33074
33073
33072
33071
33070
33069
33068
33067
33066
33065
33064
33063
33062
33061
33060
33059
33058
33057
33056
33055
33054
33053
33052
33051
33050
33049
33048
33047
33046
33045
33044
33043
33042
33041
33040
33039
33038
33037
33036
33035
33034
33033
33032
33031
33030
33029
33028
33027
33026
33025
33024
33023
33022
33021
33020
33019
33018
33017
33016
33015
33014
33013
33012
33011
33010
33009
33008
33007
33006
33005
33004
33003
33002
33001
33000

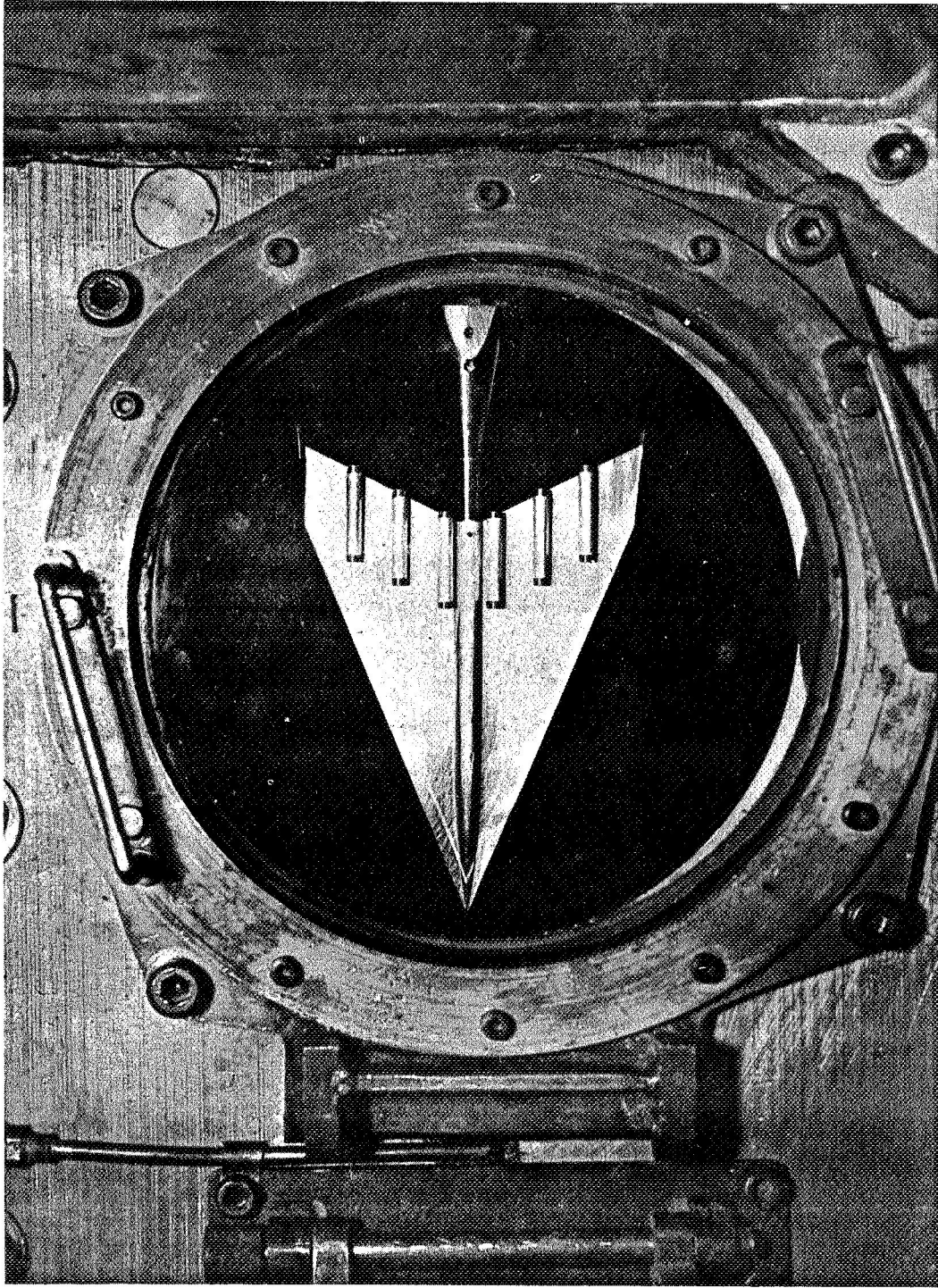


(b) Three-quarter front bottom view. L-58-902

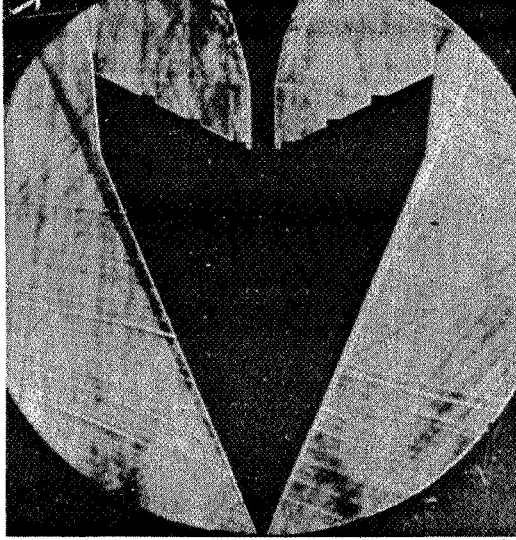
Figure 6.- Concluded.

33000

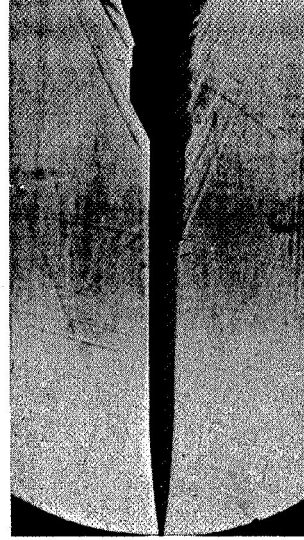
L-183



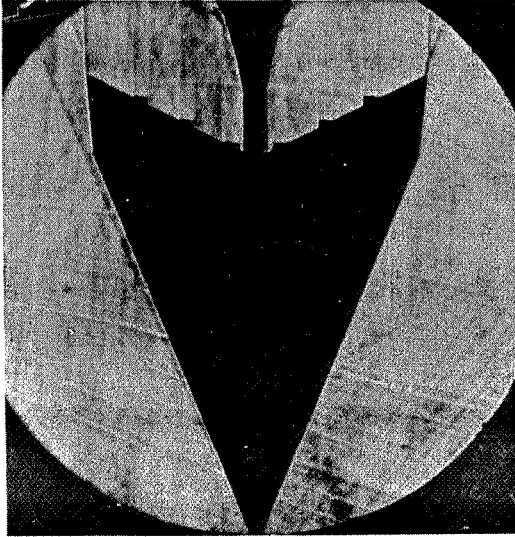
L-57-5257
Figure 7.- Photographs of low-aspect-ratio arrow wing mounted in tunnel test section.



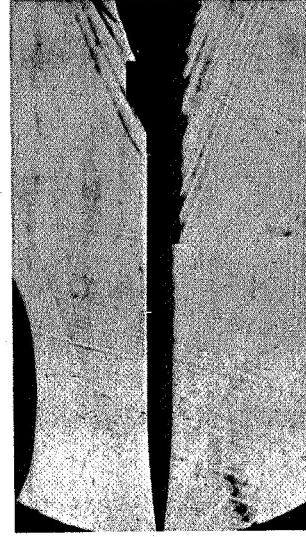
$\alpha = 5^\circ$



$\beta = 4^\circ$



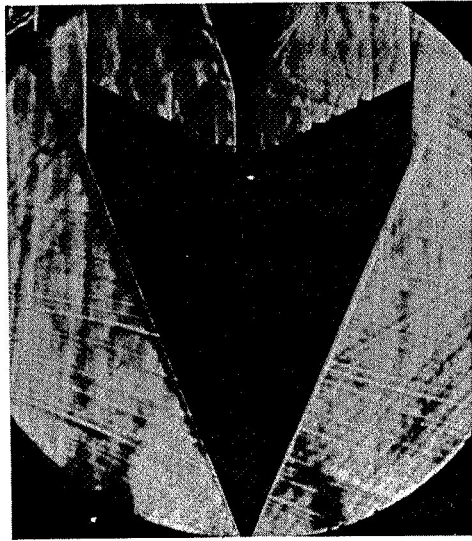
$\alpha = 0^\circ$



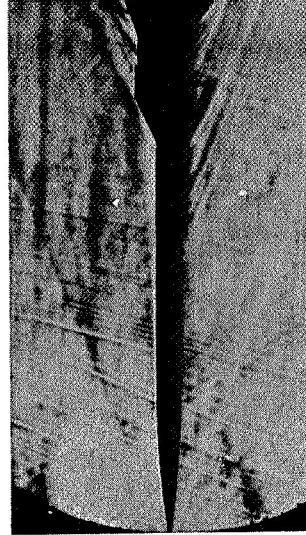
$\beta = 0^\circ$

(a) BW₁N₆F_{1,5} L-59-162

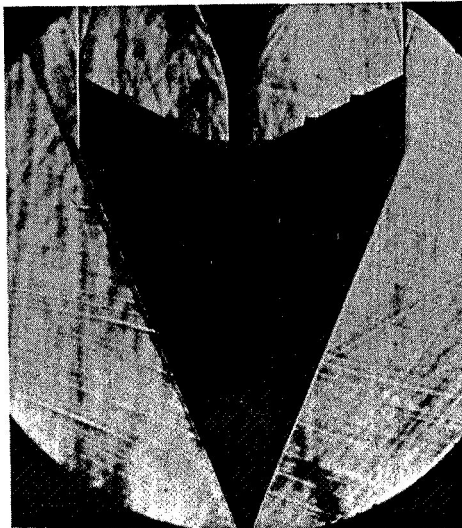
Figure 8.- Typical schlieren photographs of the low-aspect-ratio arrow wing. (Ogive-cylinder body.)



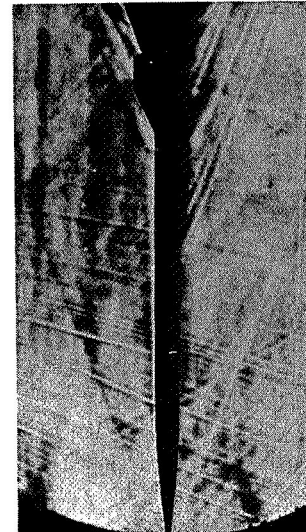
$\alpha = 4^\circ$



$\beta = 4^\circ$



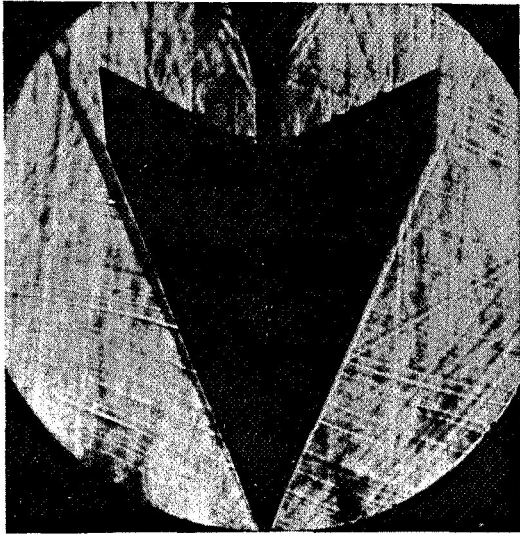
$\alpha = 0^\circ$



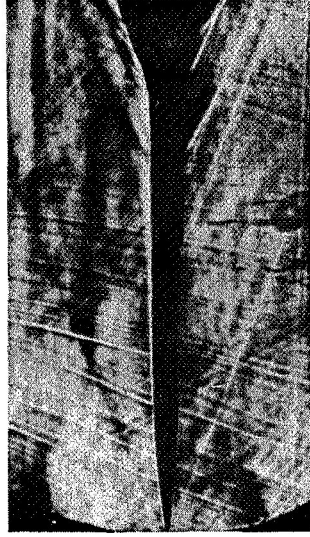
$\beta = 0^\circ$

(b) $BW_1N_6F_1, 0^\circ$ L-59-163

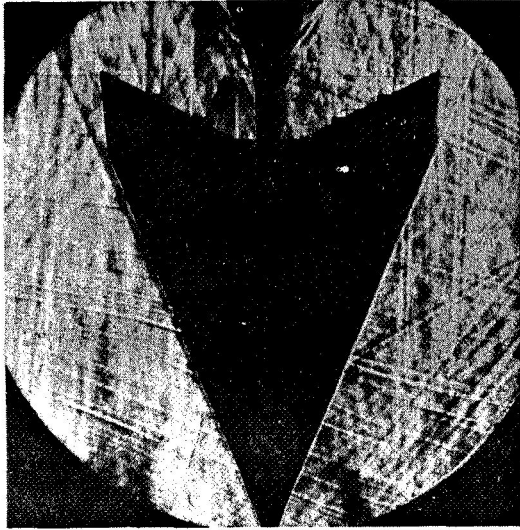
Figure 8.- Continued.



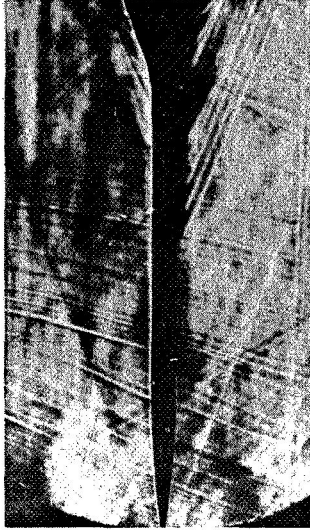
$\alpha = 4^\circ$



$\beta = 4^\circ$



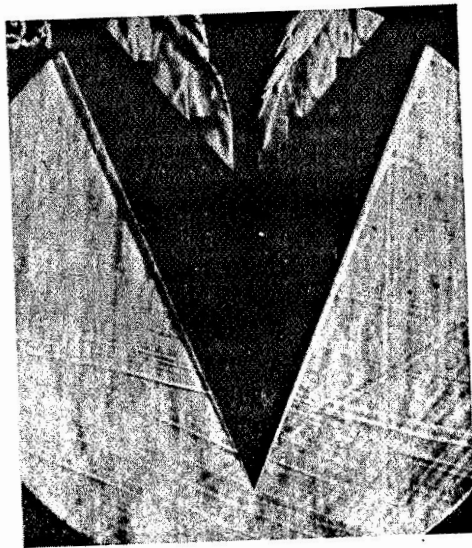
$\alpha = 0^\circ$



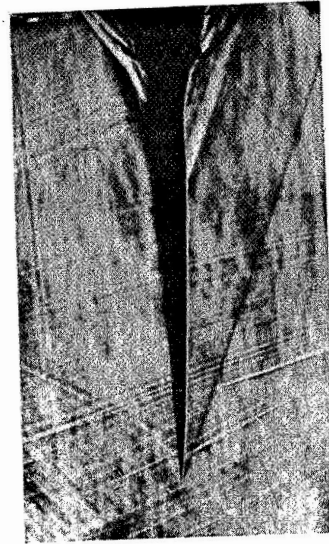
$\beta = 0^\circ$

(c) BW1N6. L-59-164

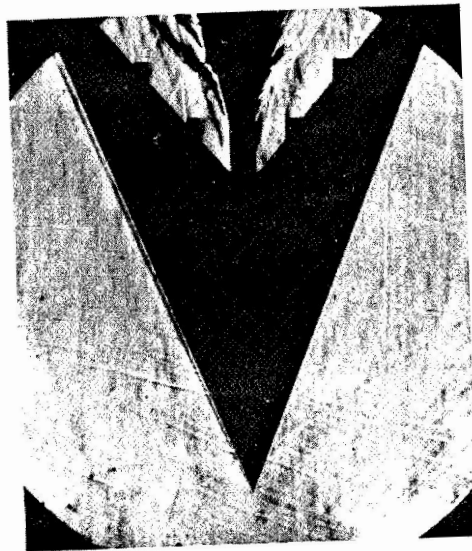
Figure 8.- Concluded.



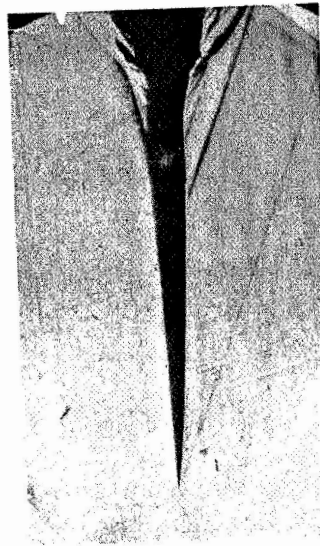
$\alpha = 4^\circ$



$\beta = 4^\circ$



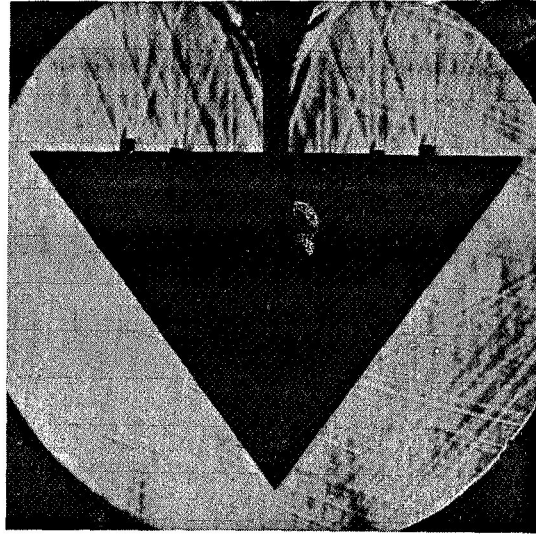
$\alpha = 0^\circ$



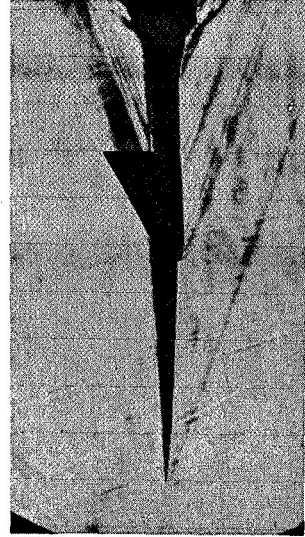
$\beta = 0^\circ$

I-59-165
B₂W₂N₆F₂,0°

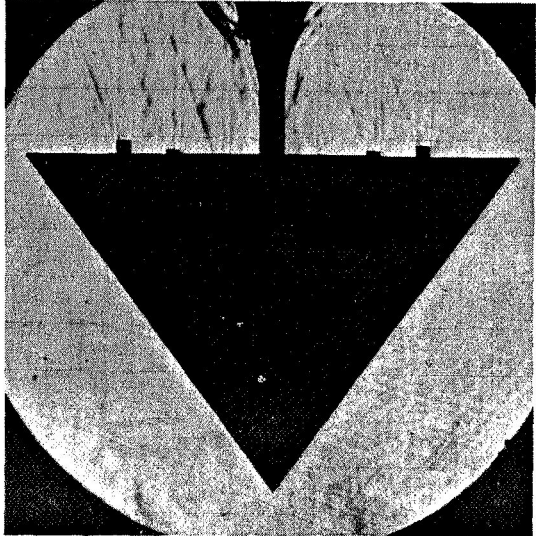
Figure 9.- Typical schlieren photographs of the high-aspect-ratio arrow wing.



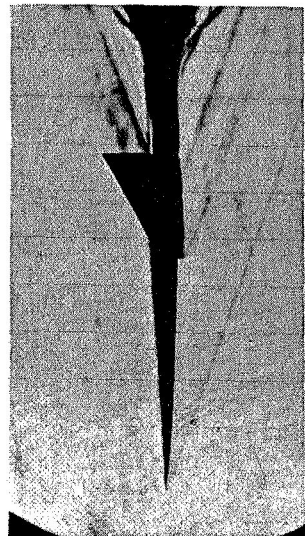
$\alpha = 4^\circ$



$\beta = 4^\circ$



$\alpha = 0^\circ$

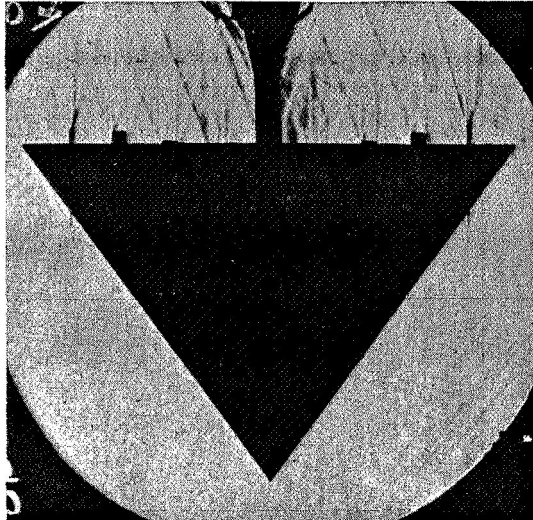


$\beta = 0^\circ$

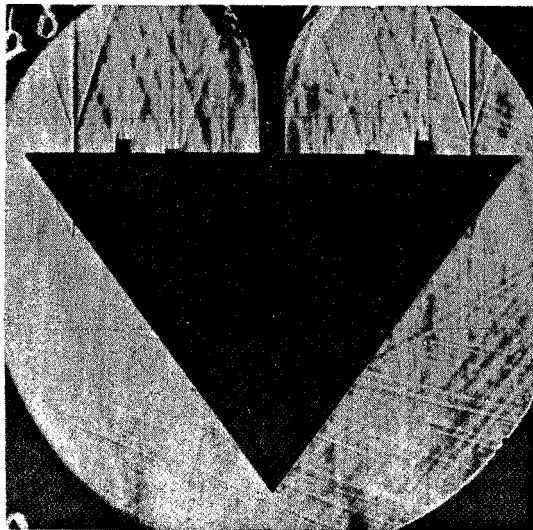
(a) $B_2W_2N_6V$. L-59-166
Figure 10.- Typical schlieren photographs of the delta wing. (Short body.)

L-109

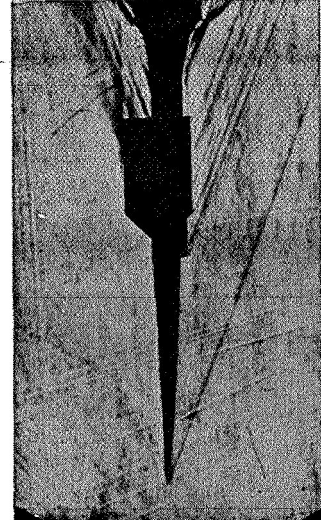
K



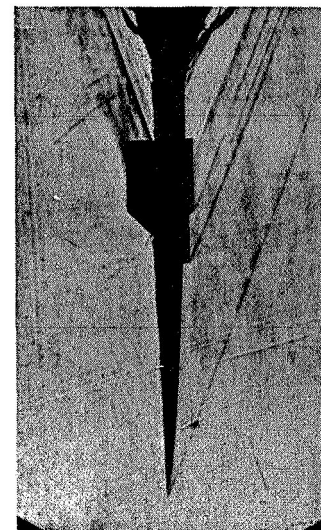
$\alpha = 5^\circ$



$\alpha = 0^\circ$



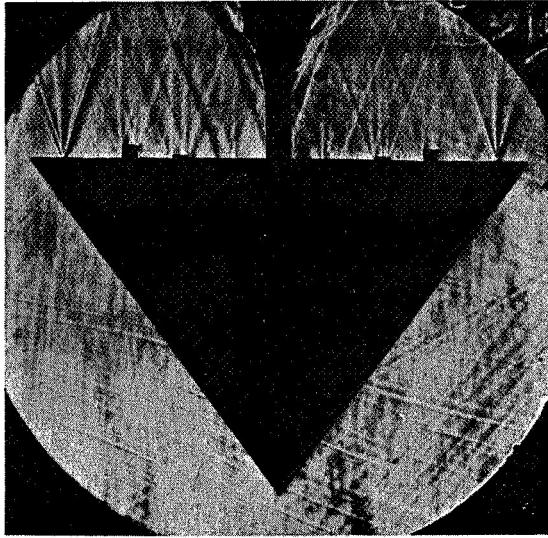
$\beta = 4^\circ$



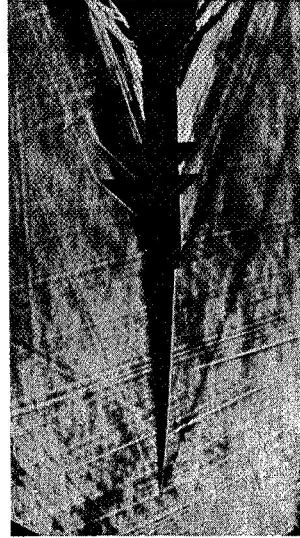
$\beta = 0^\circ$

(b) $B_3W_3N_6Fl.$ L-59-167

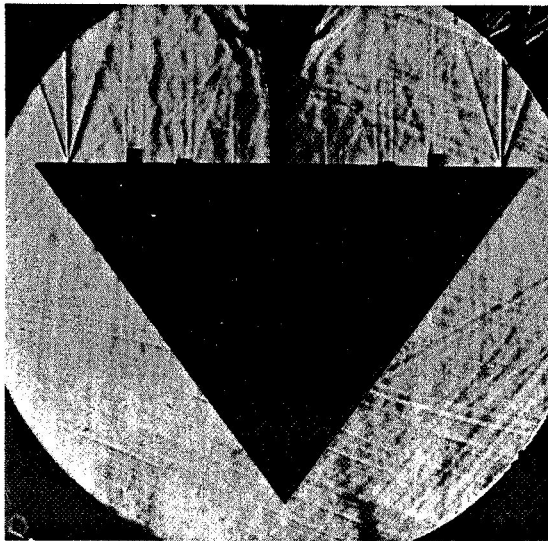
Figure 10.- Continued.



$\alpha = 4^\circ$



$\beta = 4^\circ$



$\alpha = 0^\circ$



$\beta = 0^\circ$

(c) $B_3W_3N_6FS$ L-59-168

Figure 10.- Concluded.

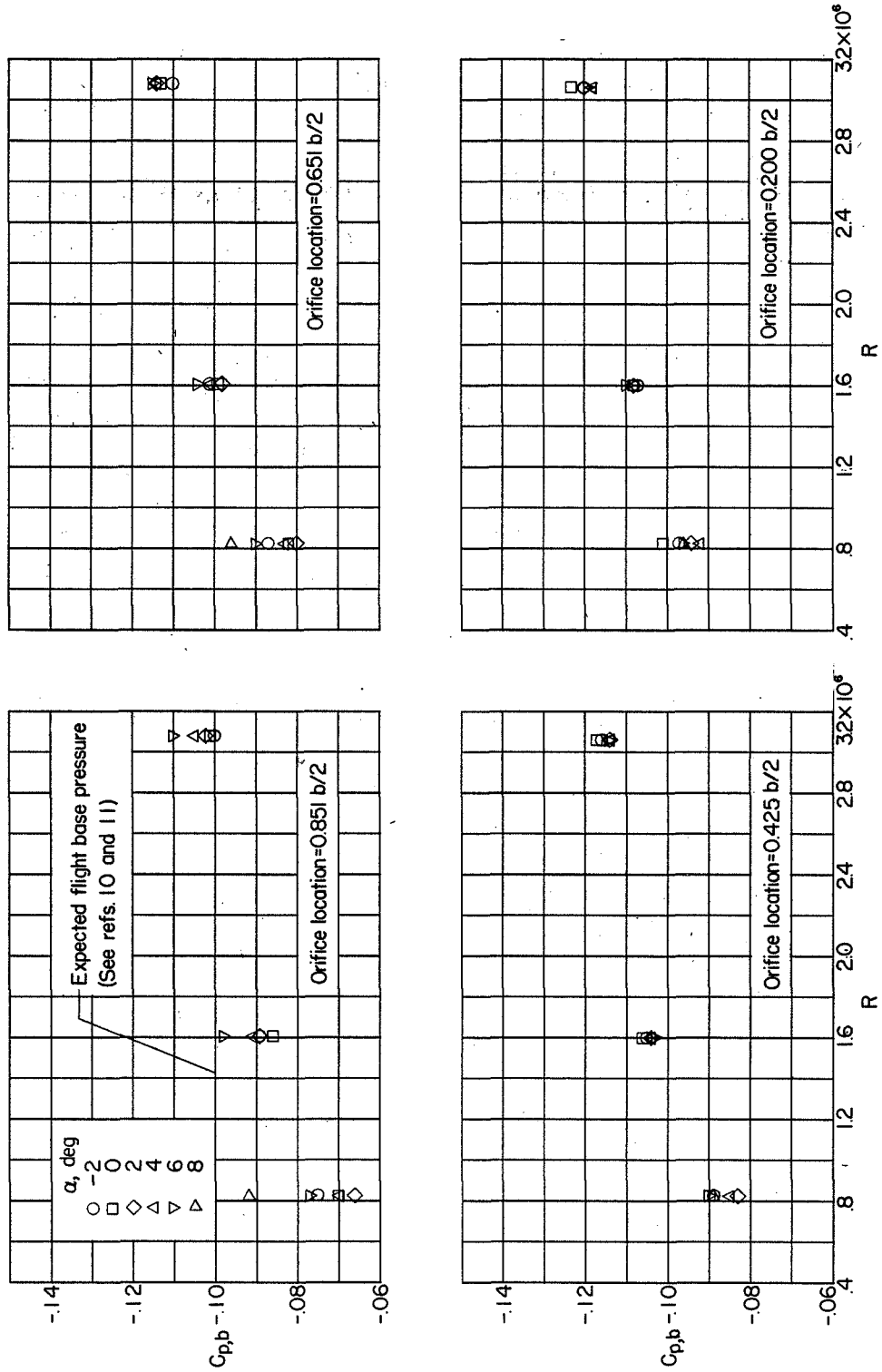
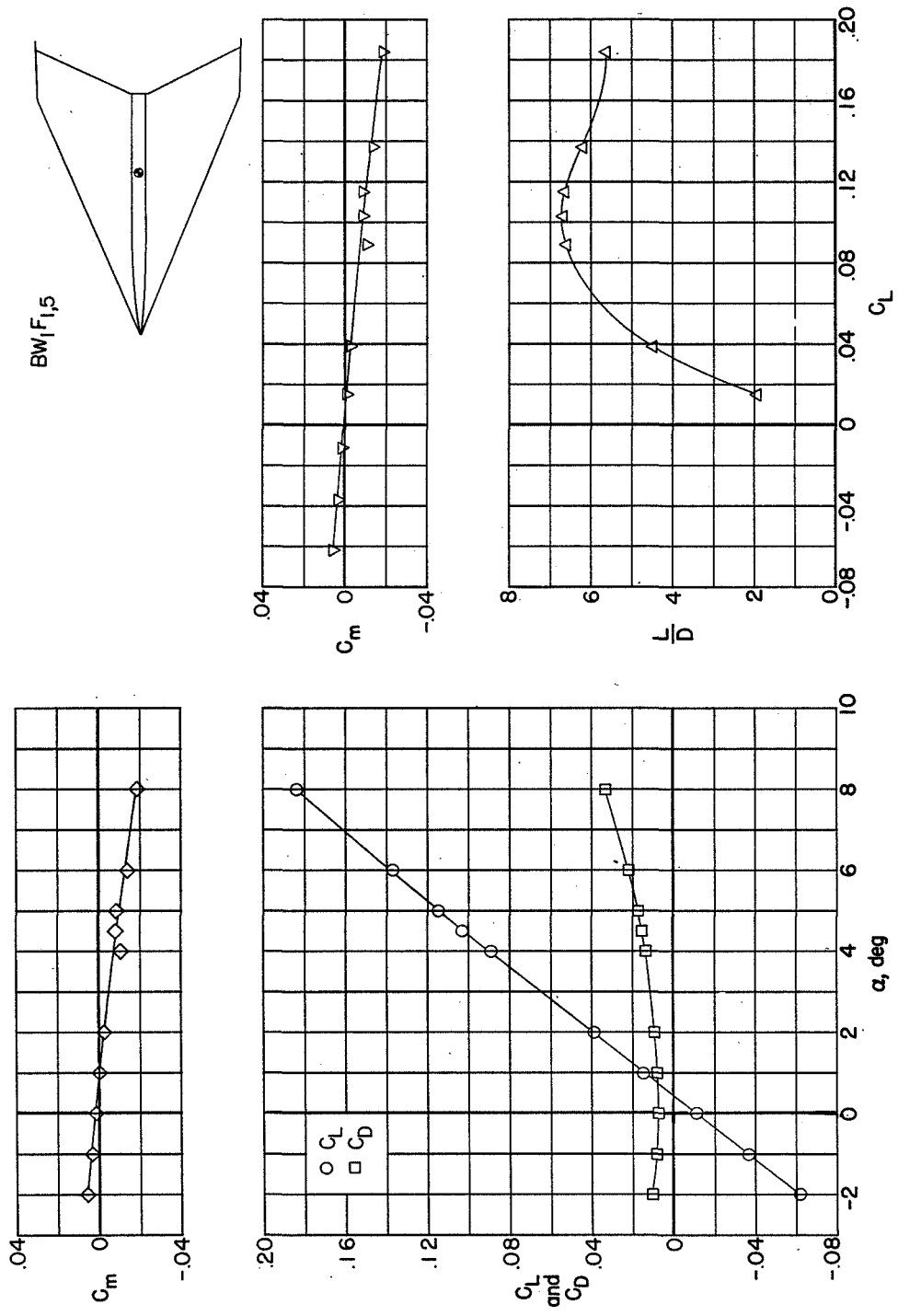
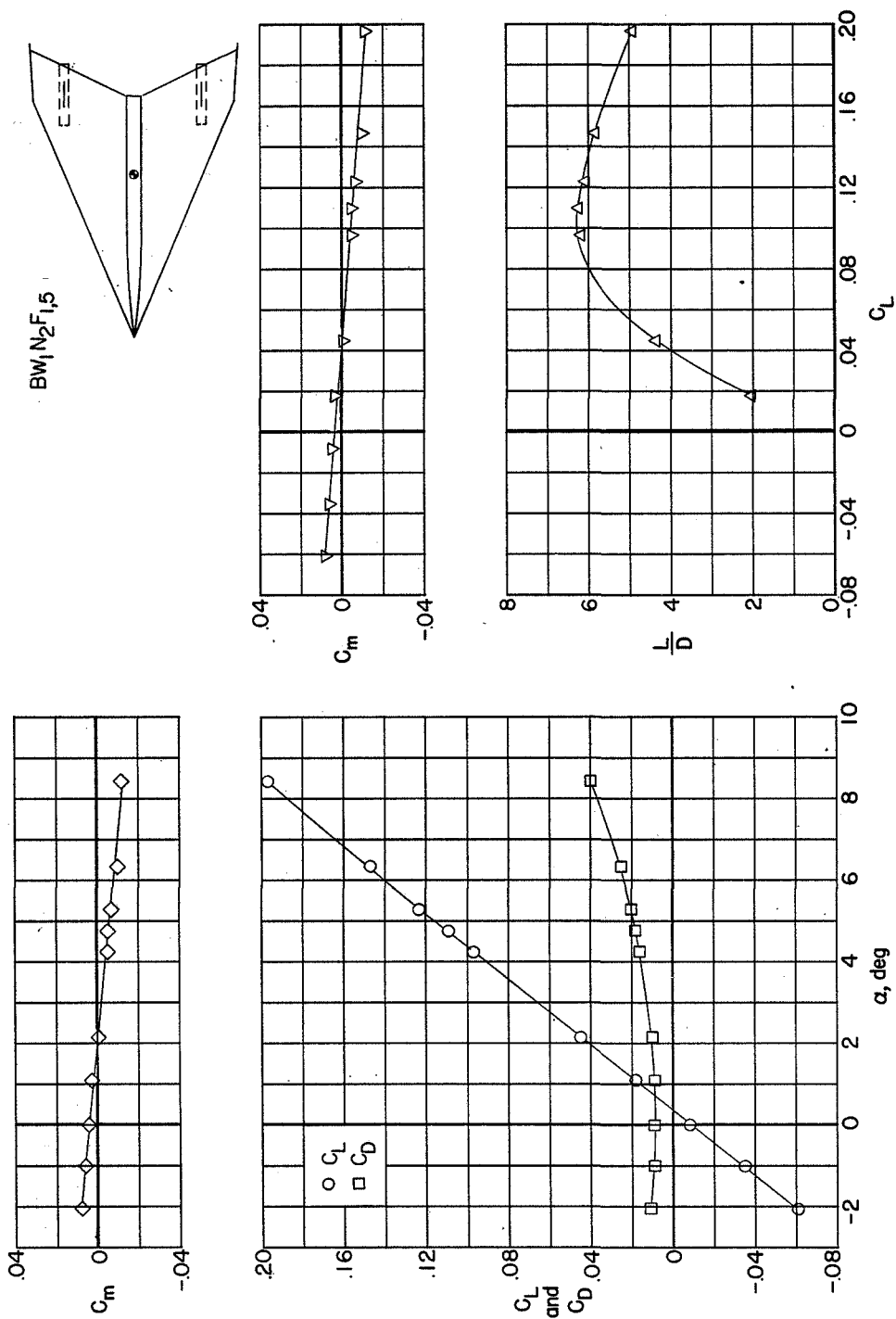


Figure 11.- Variation of wing base-pressure coefficient with angle of attack at various Reynolds numbers for the low-aspect-ratio arrow-wing configuration. $BW_{10}F_{1,0}$.



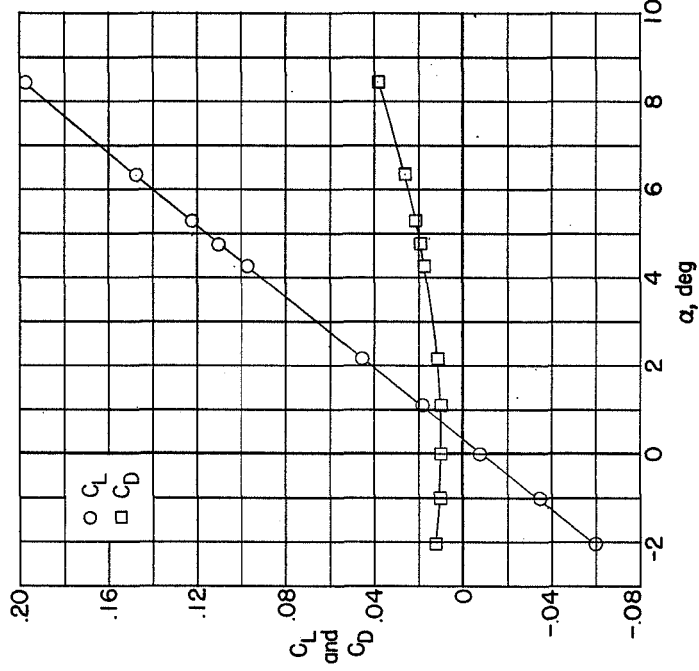
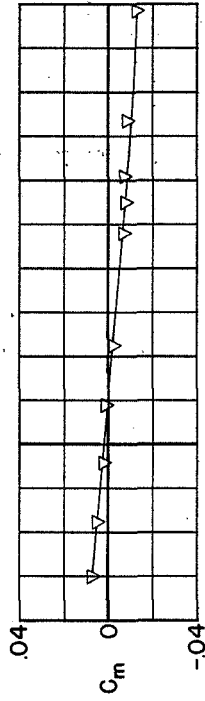
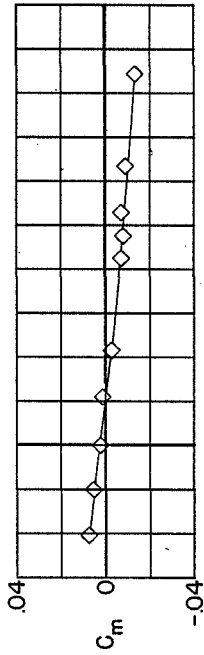
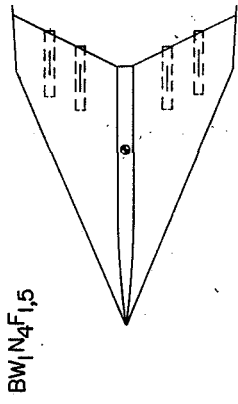
(a) $BW_1 F_{1,5}$.

Figure 12.- Measured aerodynamic characteristics in pitch of the low-aspect-ratio arrow-wing configurations. (Flagged symbols denote fixed transition.)



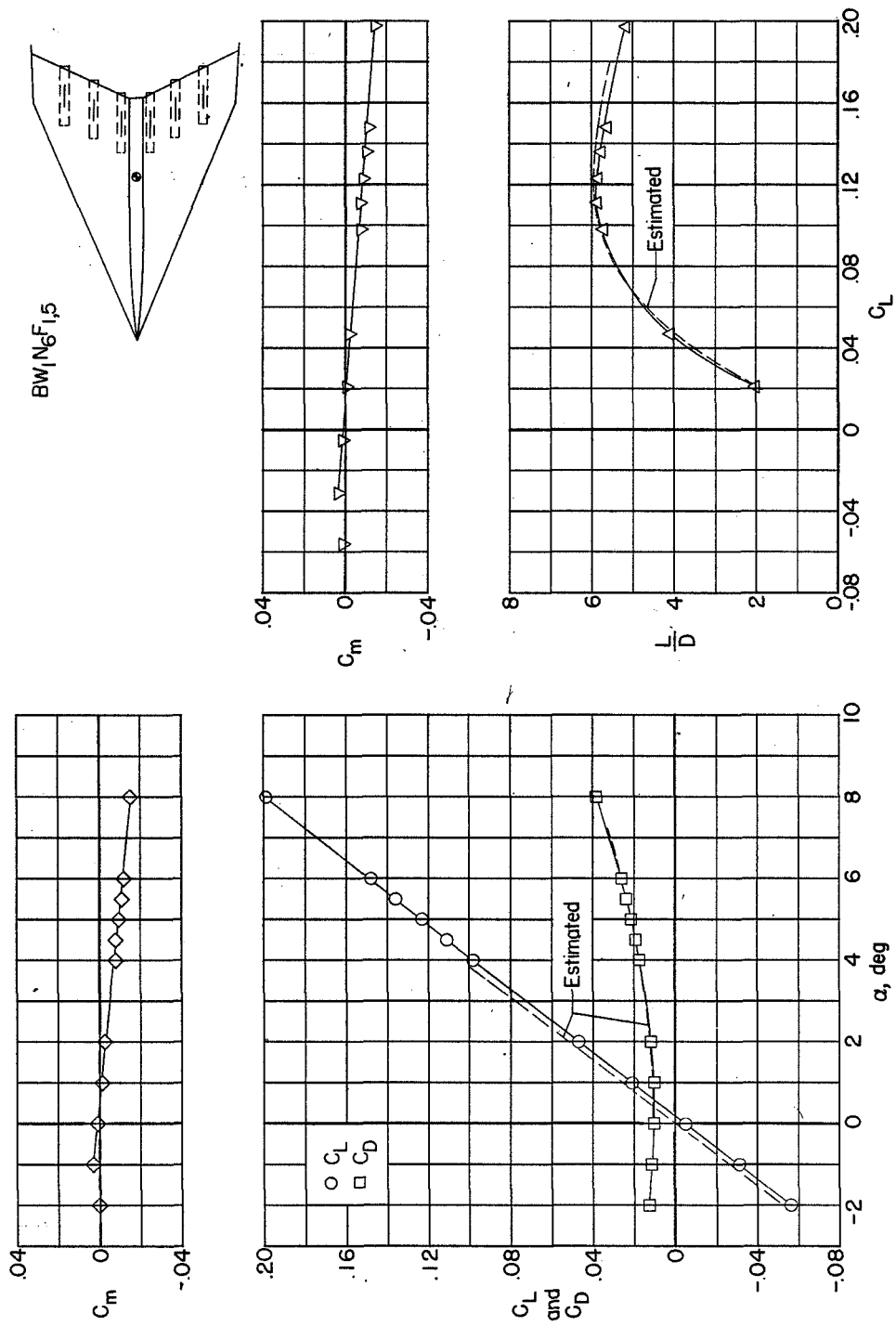
(b) BW1N2F1,5.

Figure 12.- Continued.



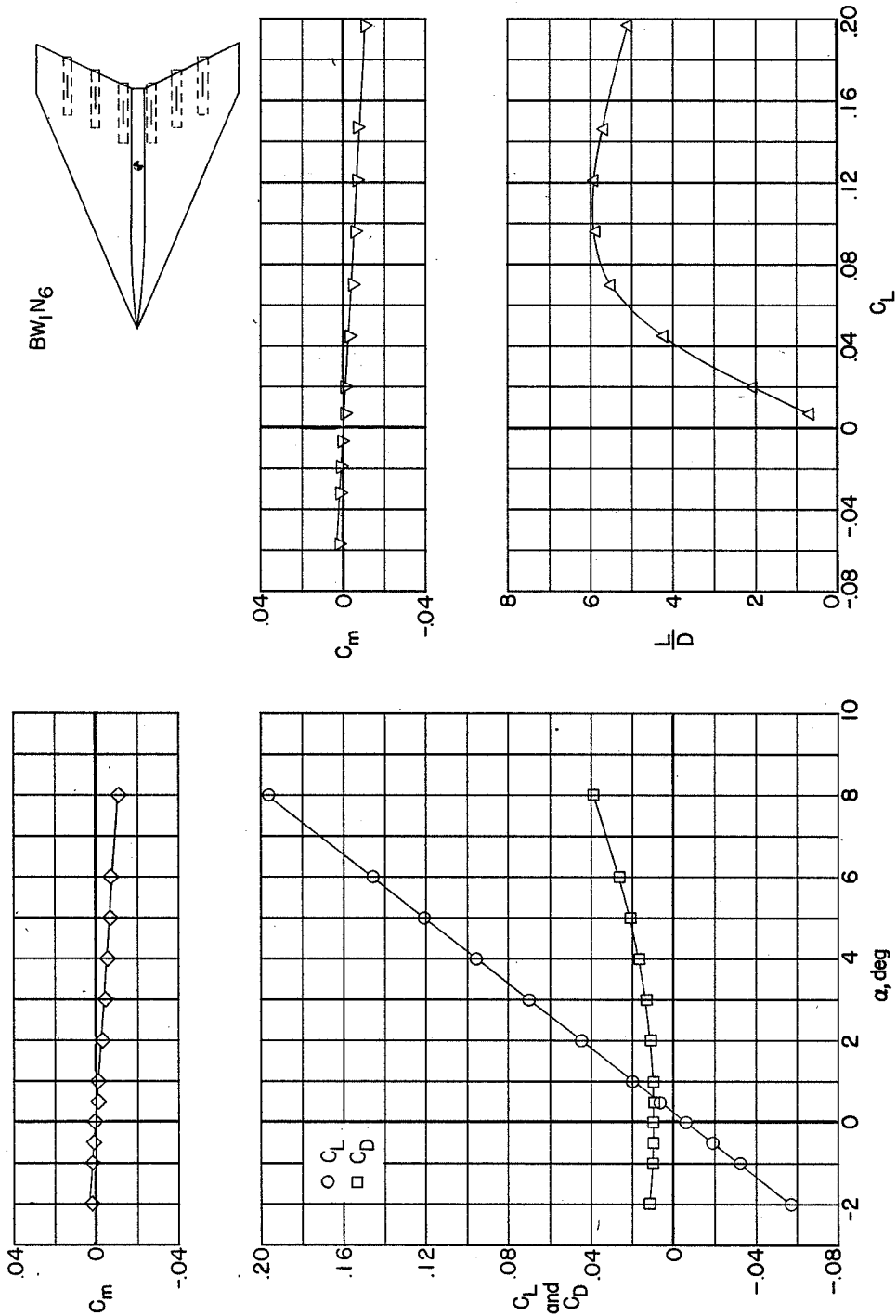
(c) BW1N4F1,5.

Figure 12.- Continued.



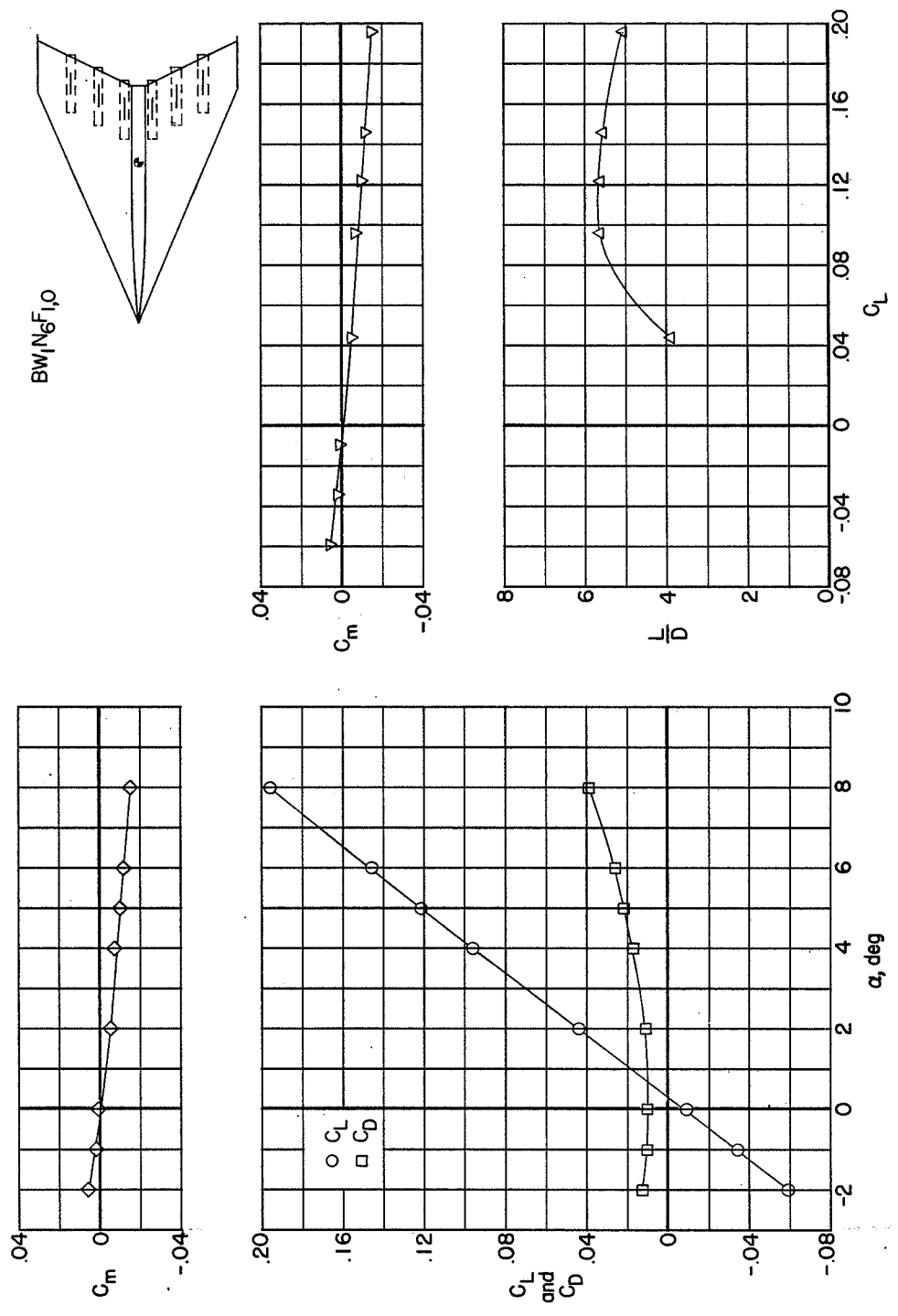
(d) BW1N6F1,5.

Figure 12.- Continued.



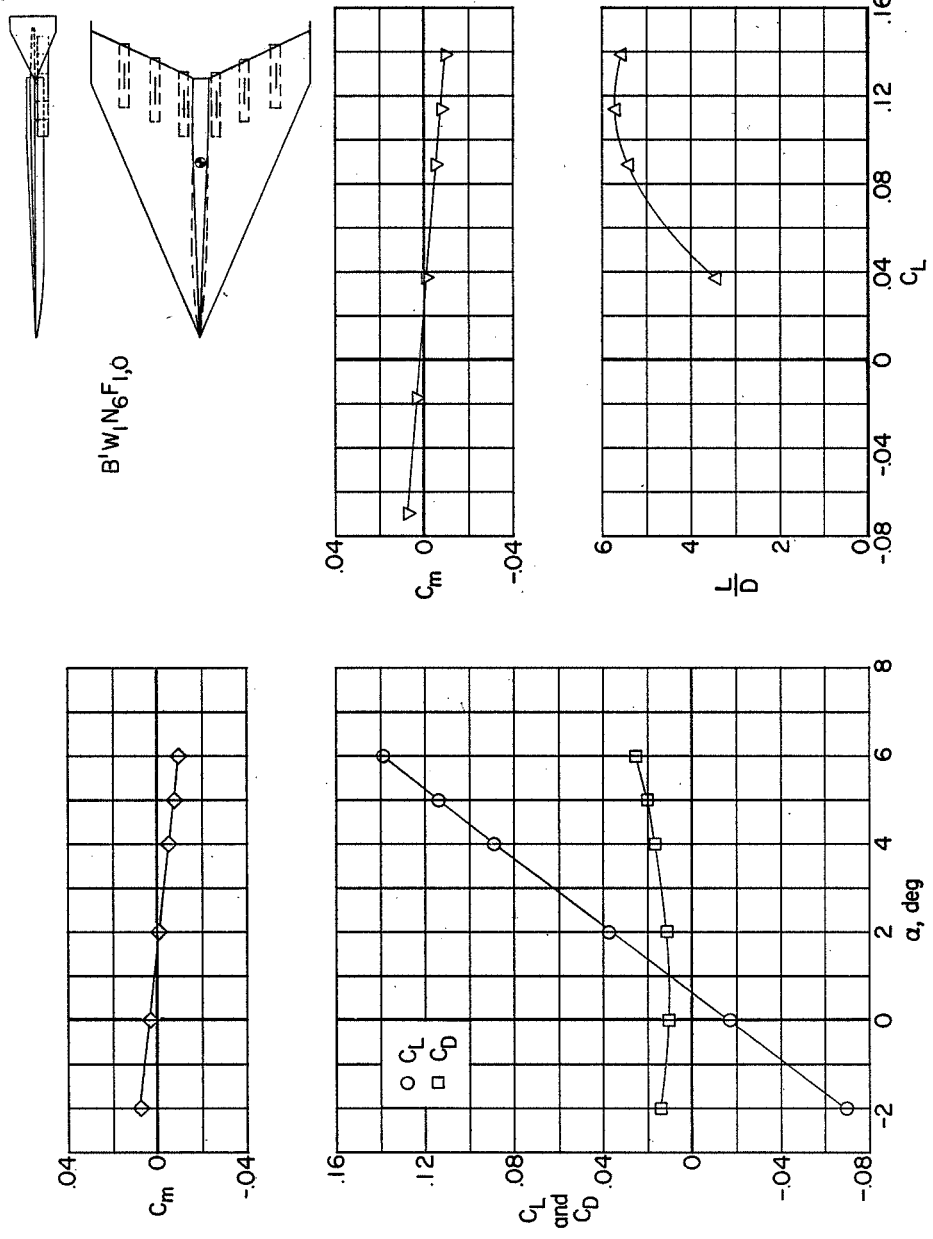
(e) BW1N6.

Figure 12.- Continued.



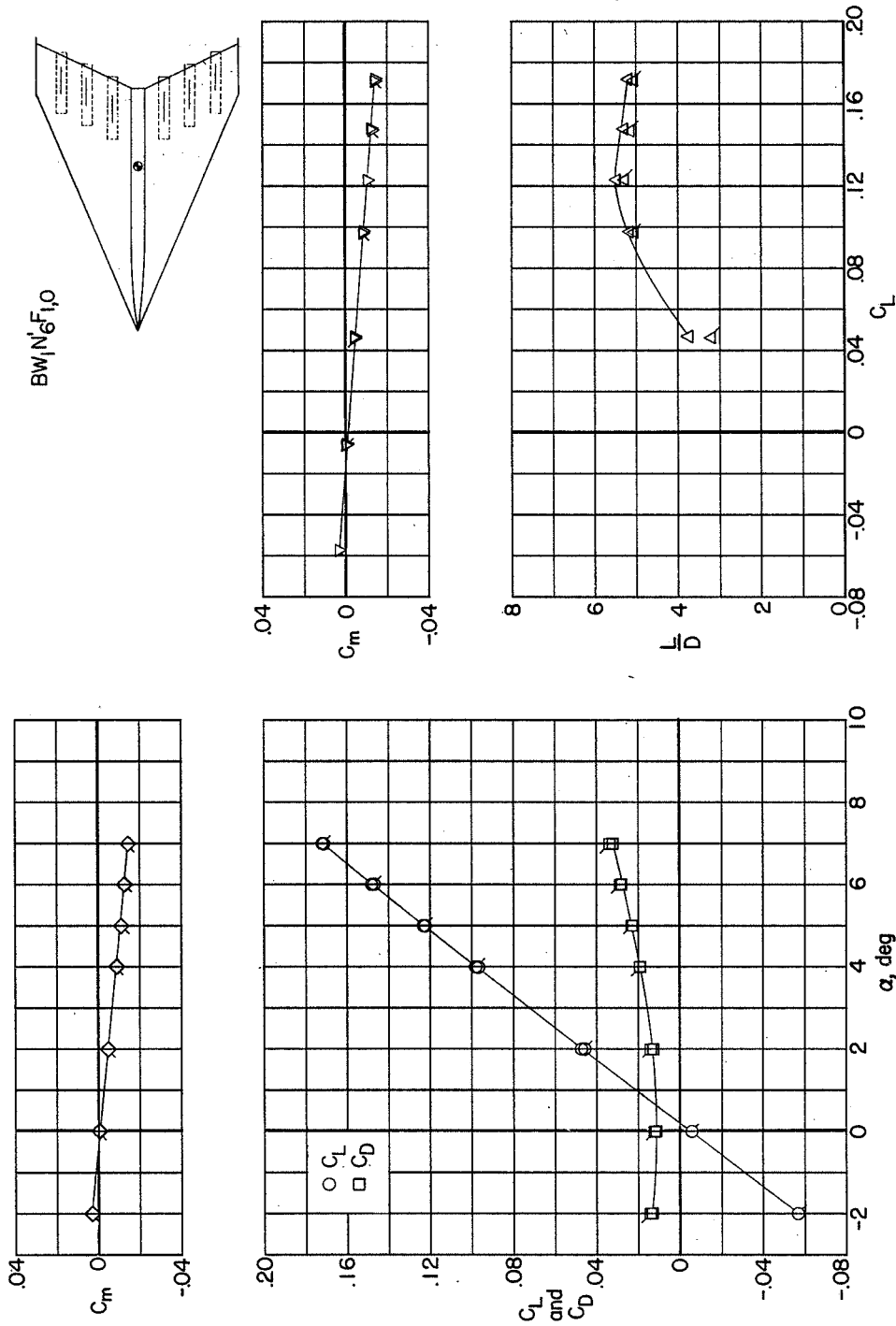
(f) BW1N6F1,0.

Figure 12.- Continued.



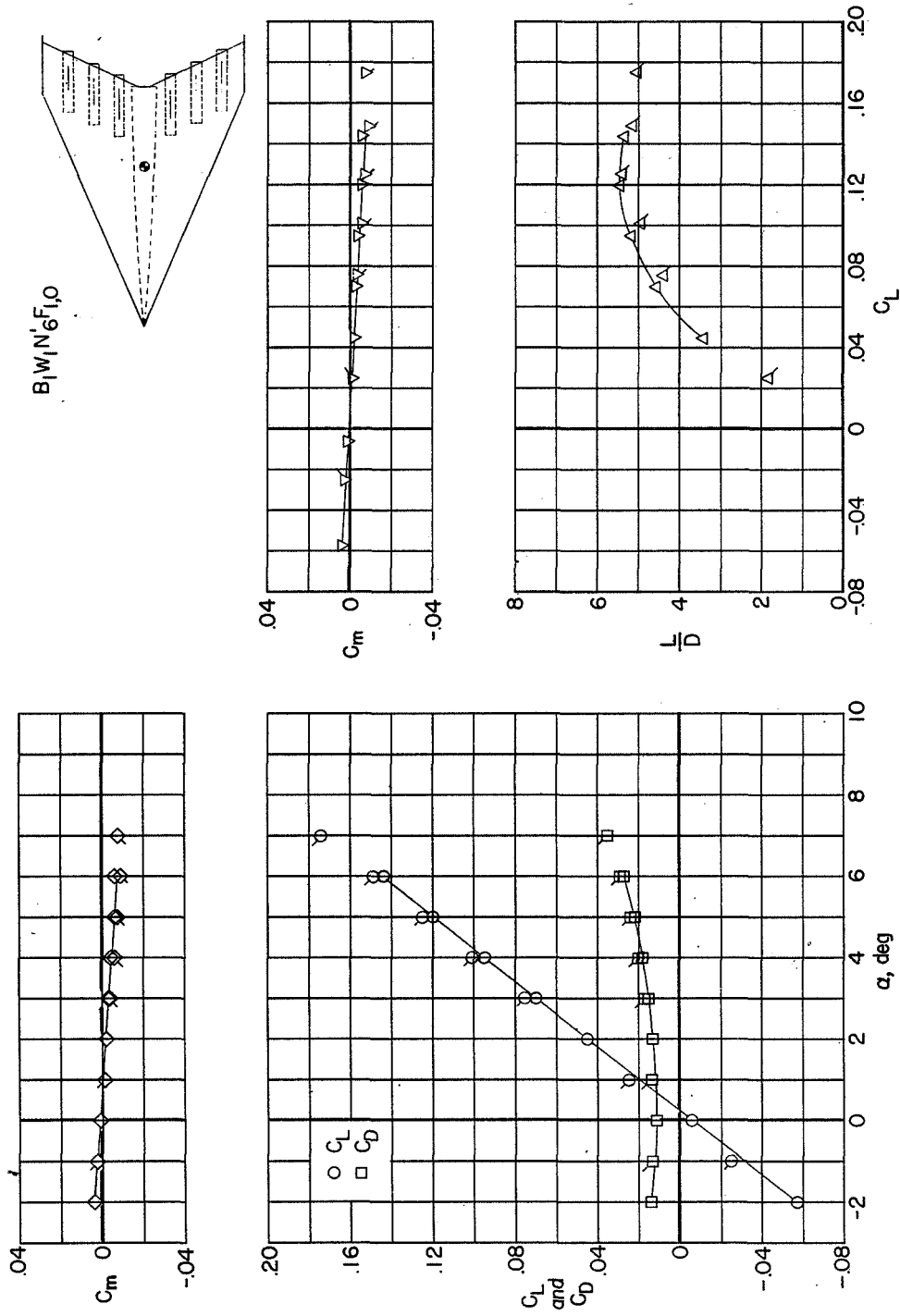
(g) B'W1N6F1,0.

Figure 12.- Continued.



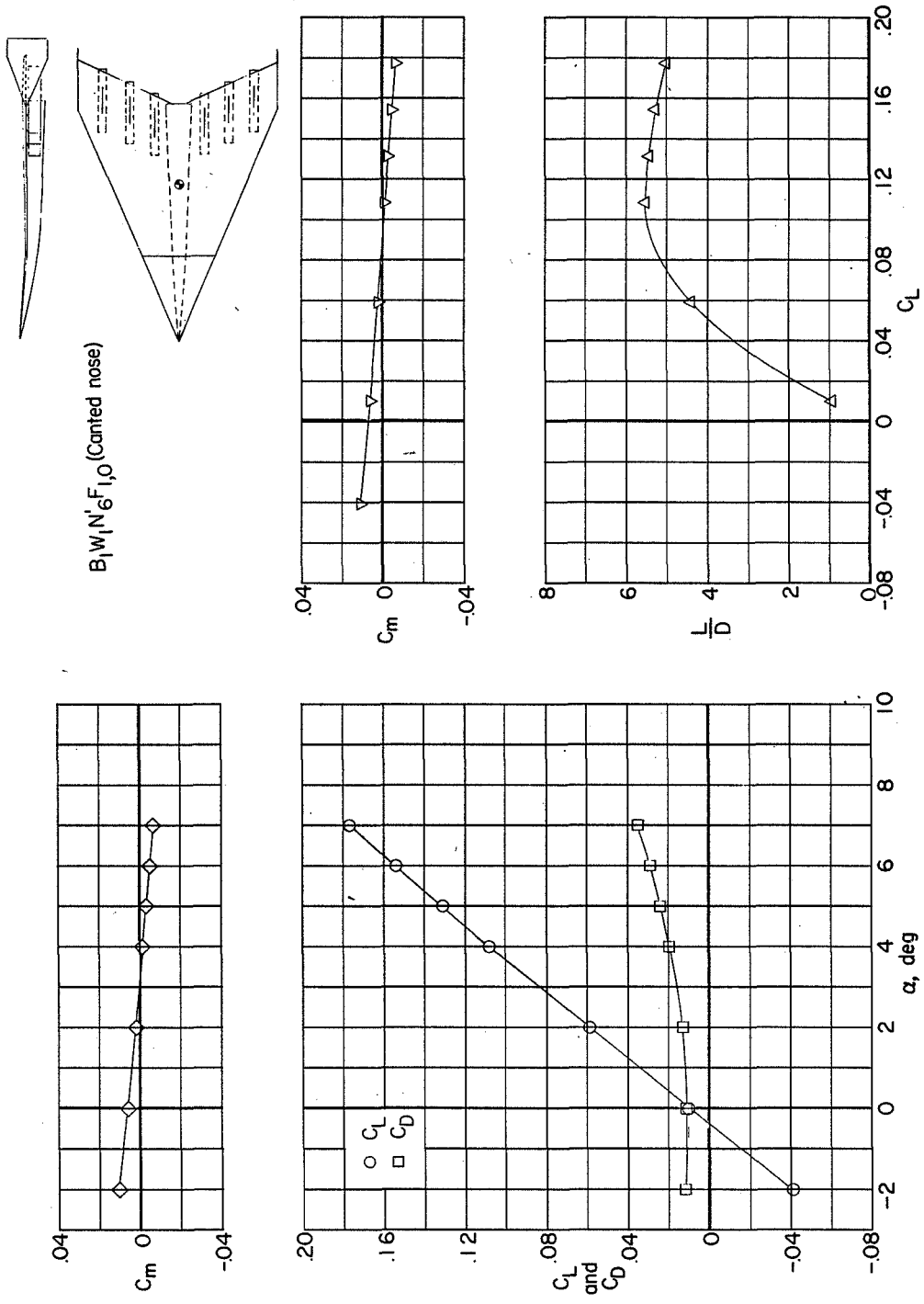
(h) BW1N'6F1,0

Figure 12.- Continued.



(i) $B_1W_1N'6F_{1,0}$.

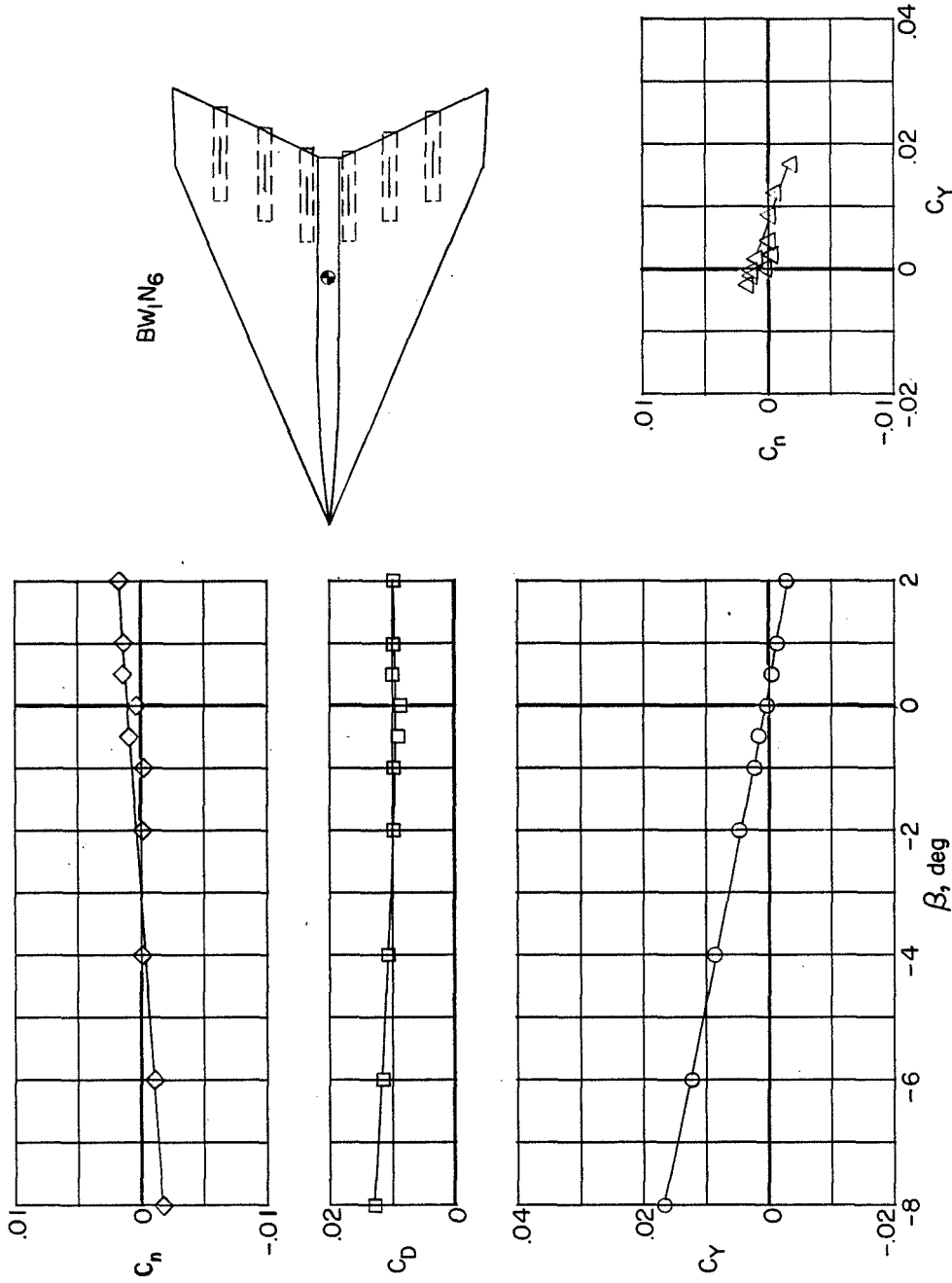
Figure 12.- Continued.



$B_1W_1N'_6F_{1,0}$ (Canted nose)

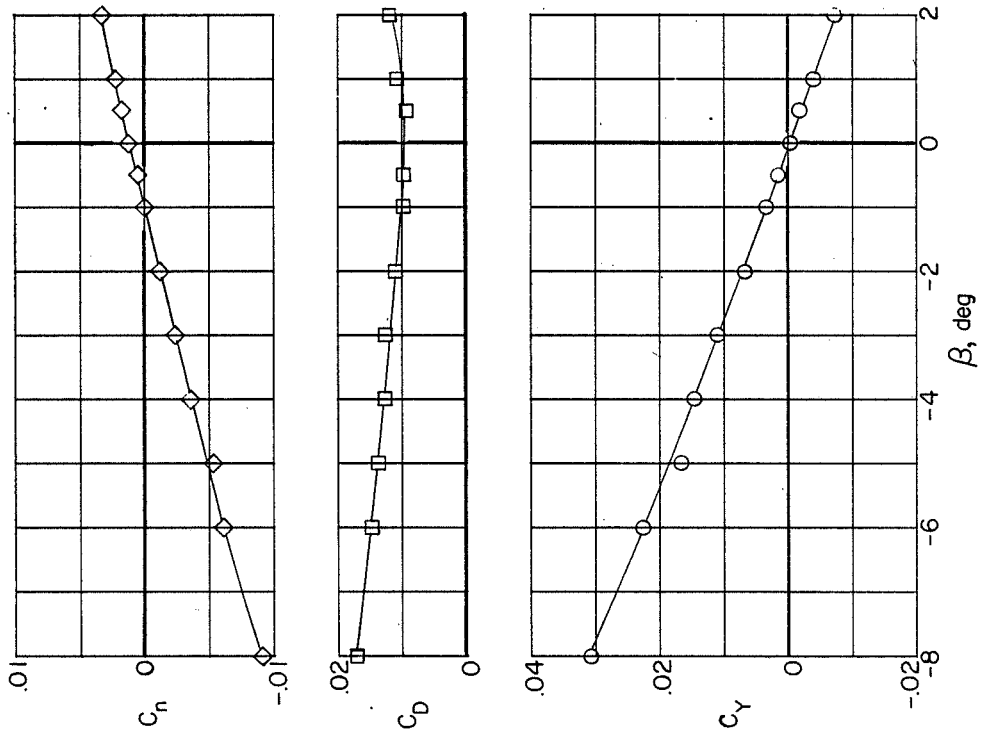
(j) $B_1W_1N'_6F_{1,0}$ (canted nose).

Figure 12.- Concluded.

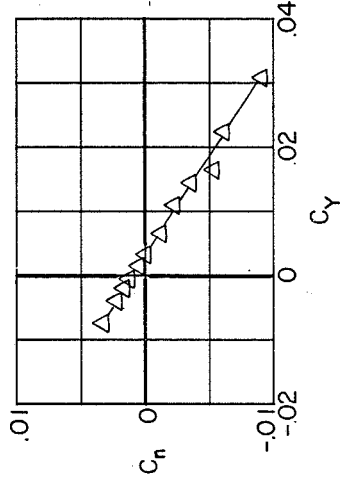
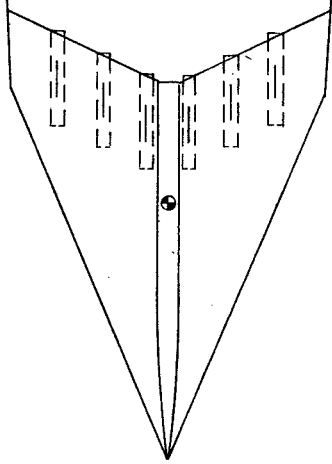


(a) BW1N6.

Figure 13.- Measured aerodynamic characteristics in sideslip of the low-aspect-ratio arrow-wing configurations. $\alpha = 0^\circ$. (Flagged symbols denote fixed transition.)

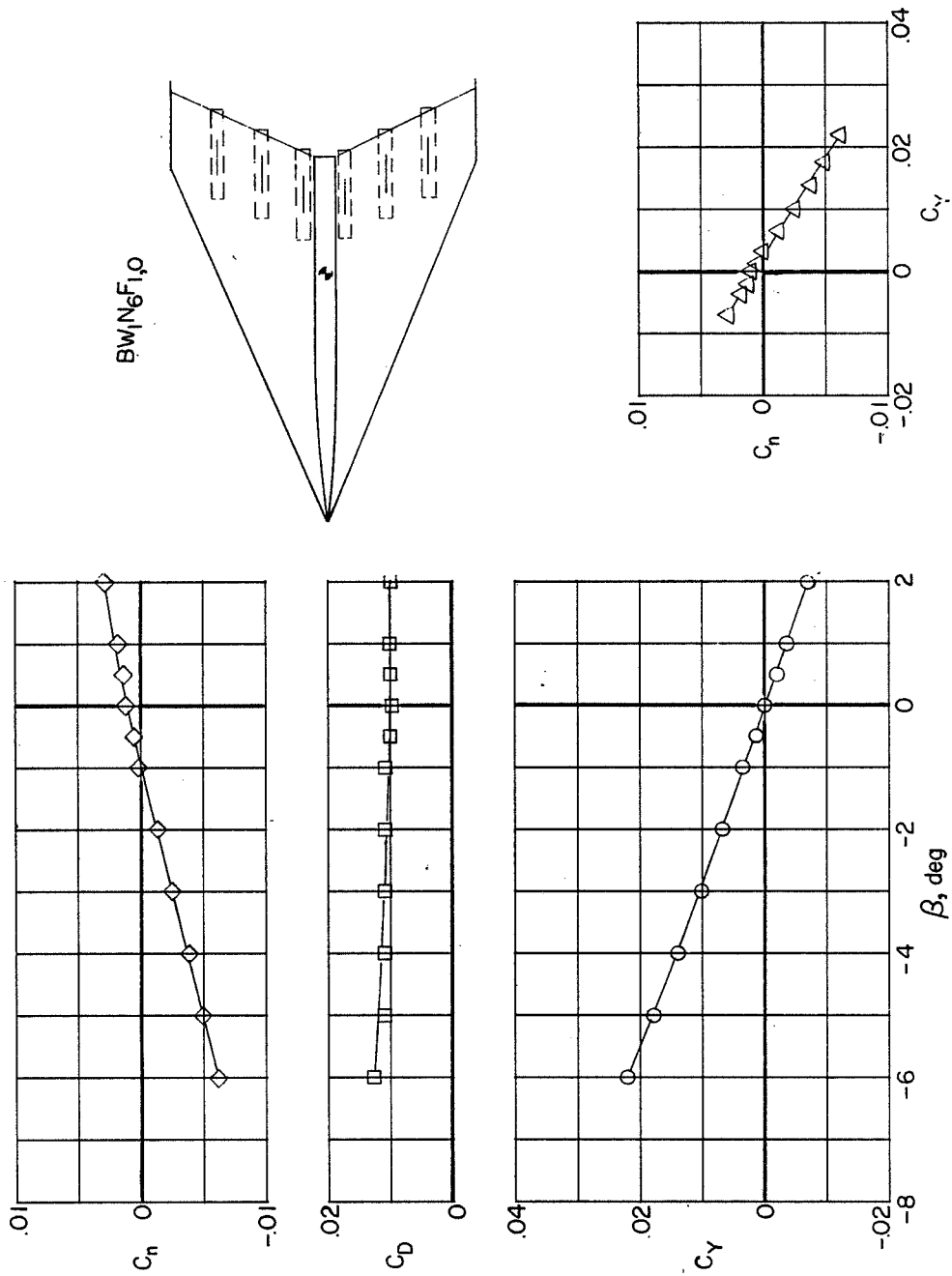


BW1N6F1,5



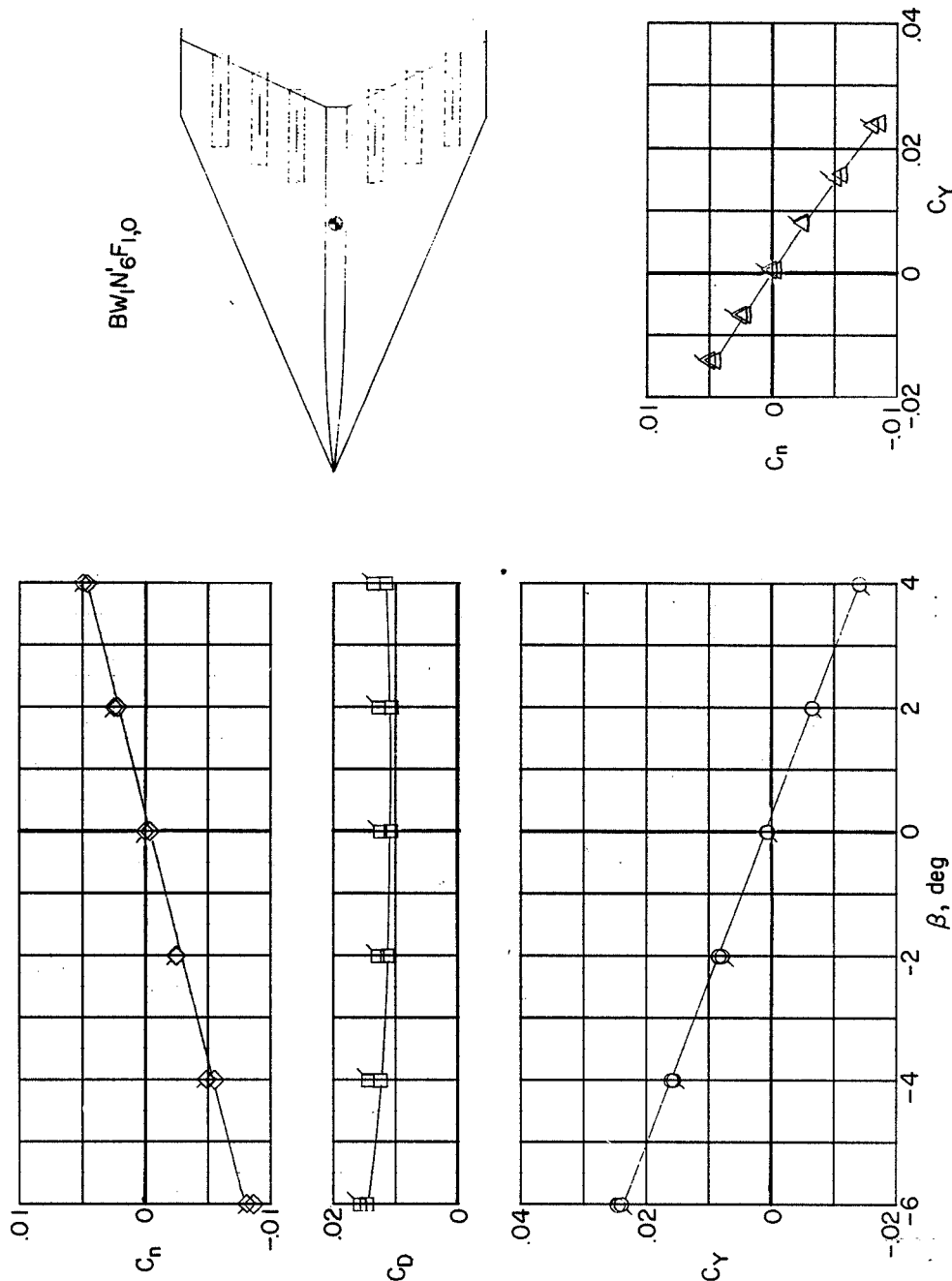
(b) BW1N6F1,5.

Figure 13.- Continued.



(c) BW1N6F1,0.

Figure 13.- Continued.



(a) BW1N'6F1,0.

Figure 13.- Continued.

I-183

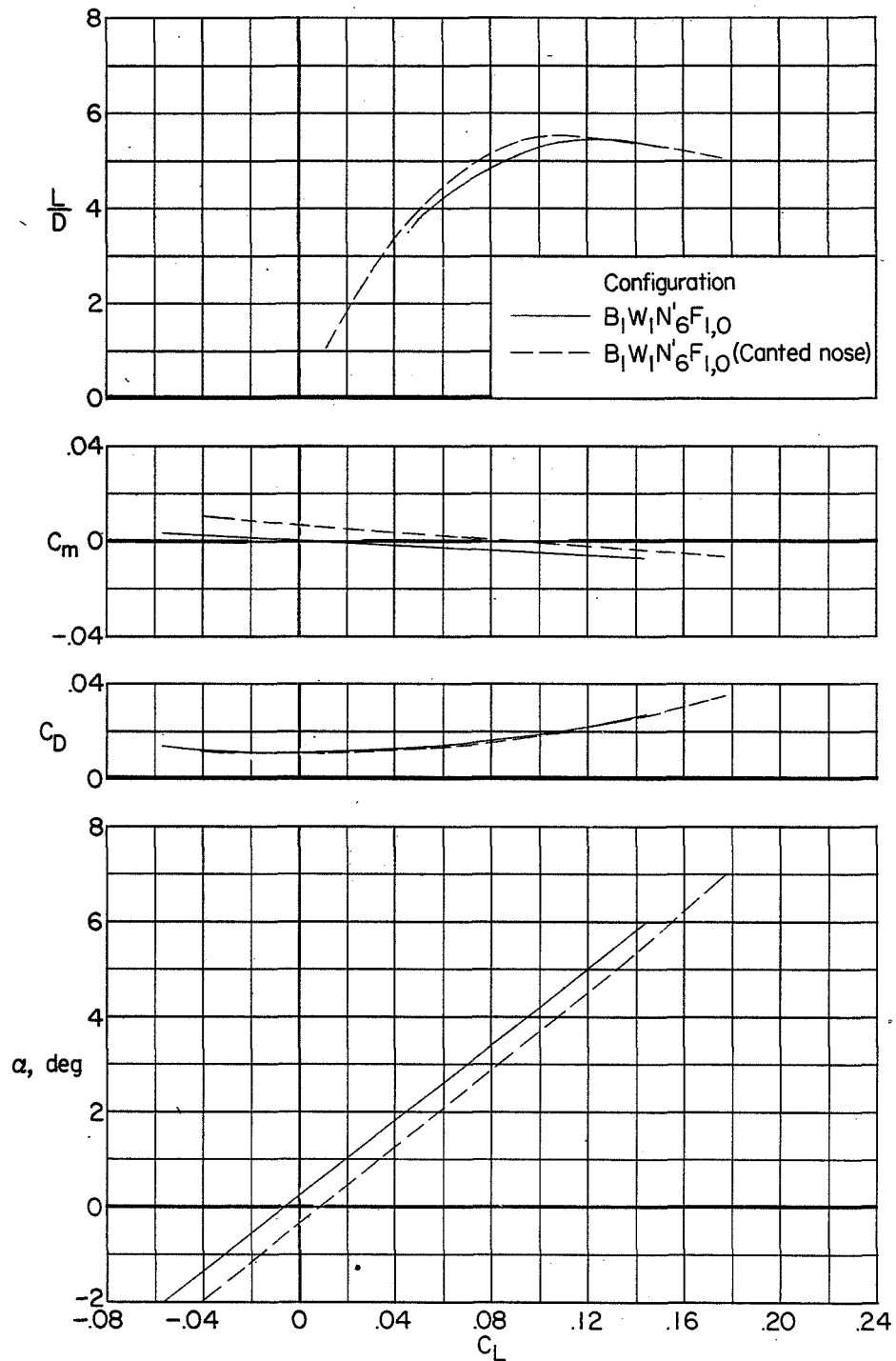


Figure 14.- Effect of canted nose on the longitudinal characteristics of the low-aspect-ratio arrow-wing configuration.

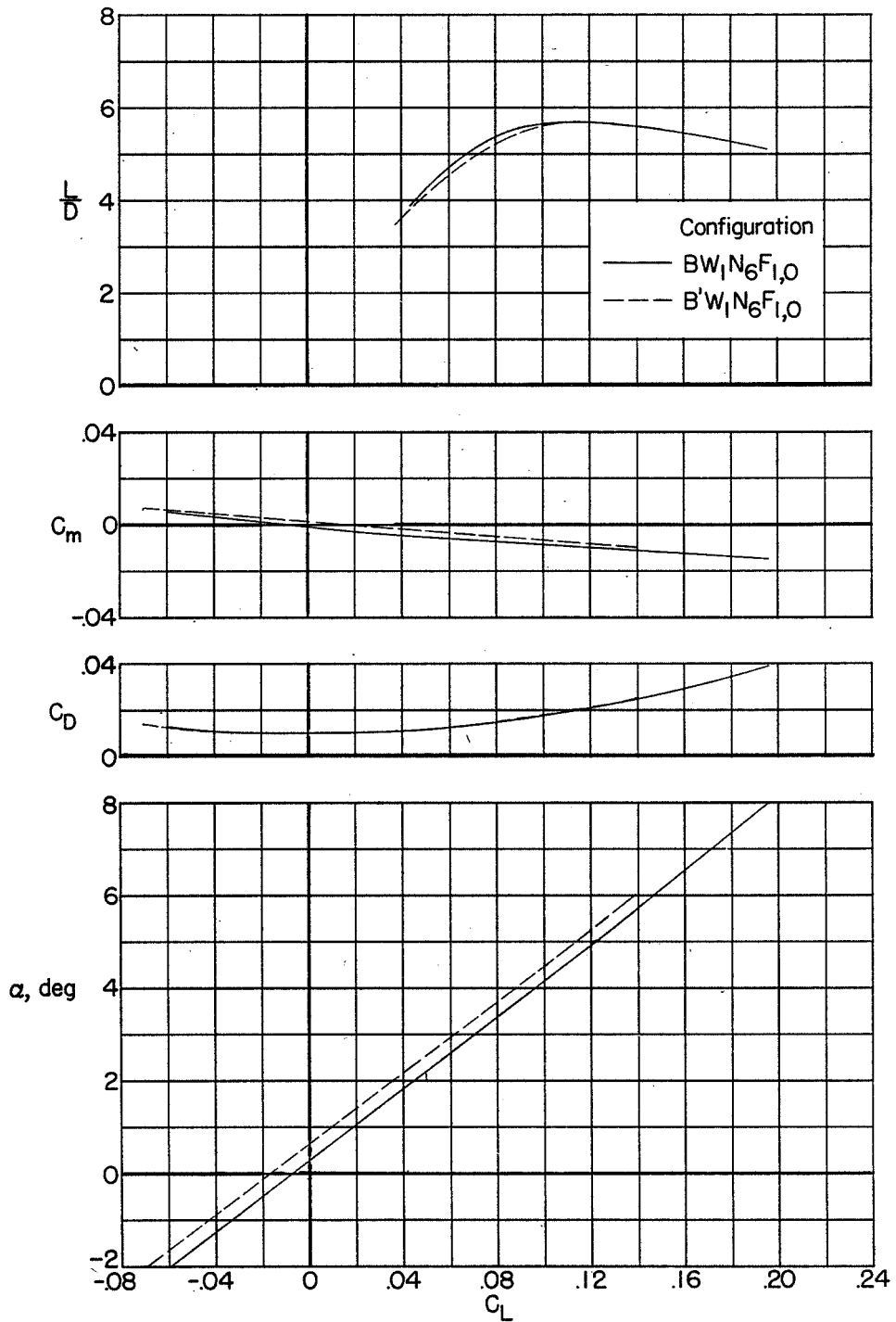


Figure 15.- Effect of forebody fuselage alteration on the longitudinal characteristics of the low-aspect-ratio arrow-wing configuration.

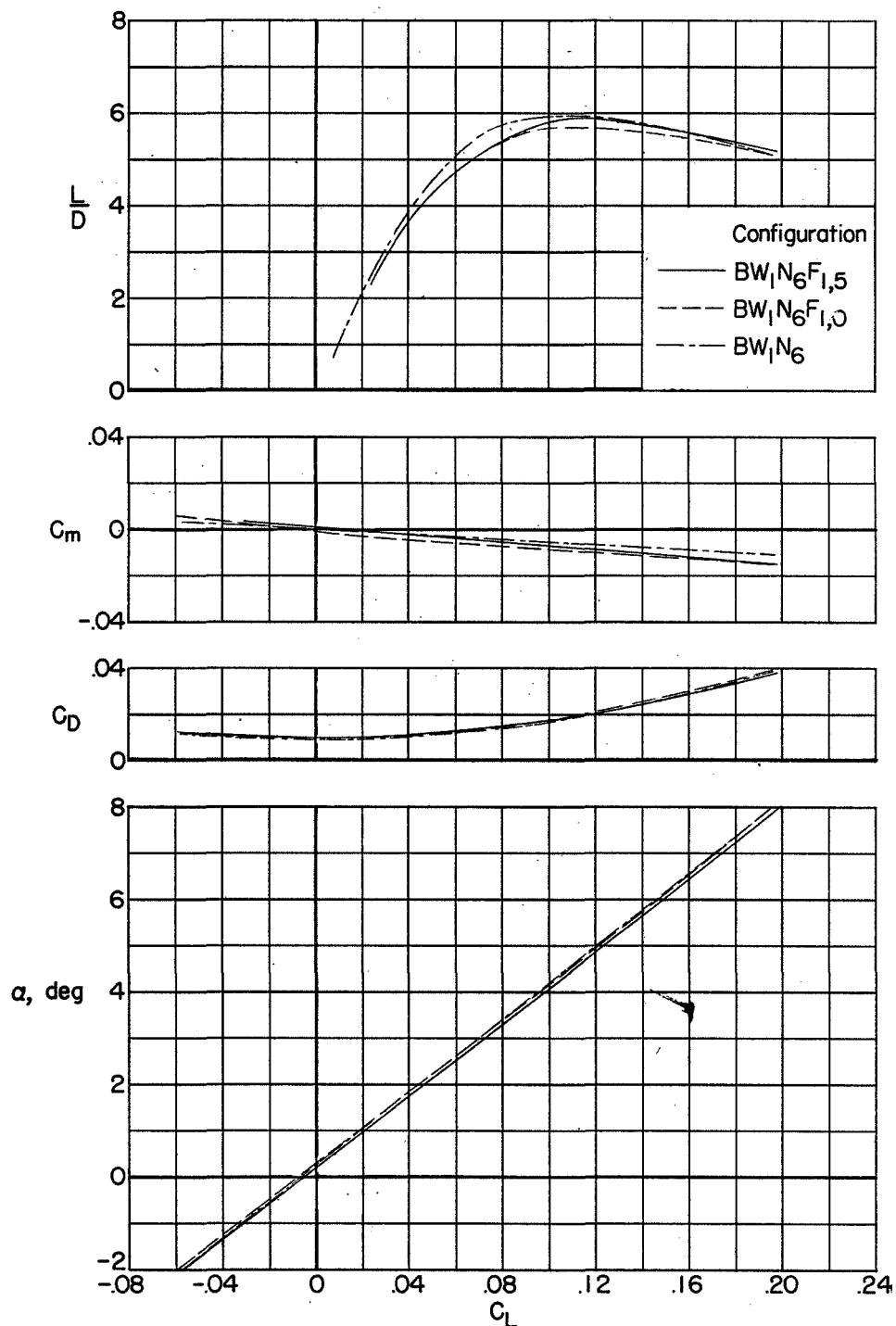


Figure 16.- Effects of tip fins on the longitudinal characteristics of the low-aspect-ratio arrow-wing configuration.

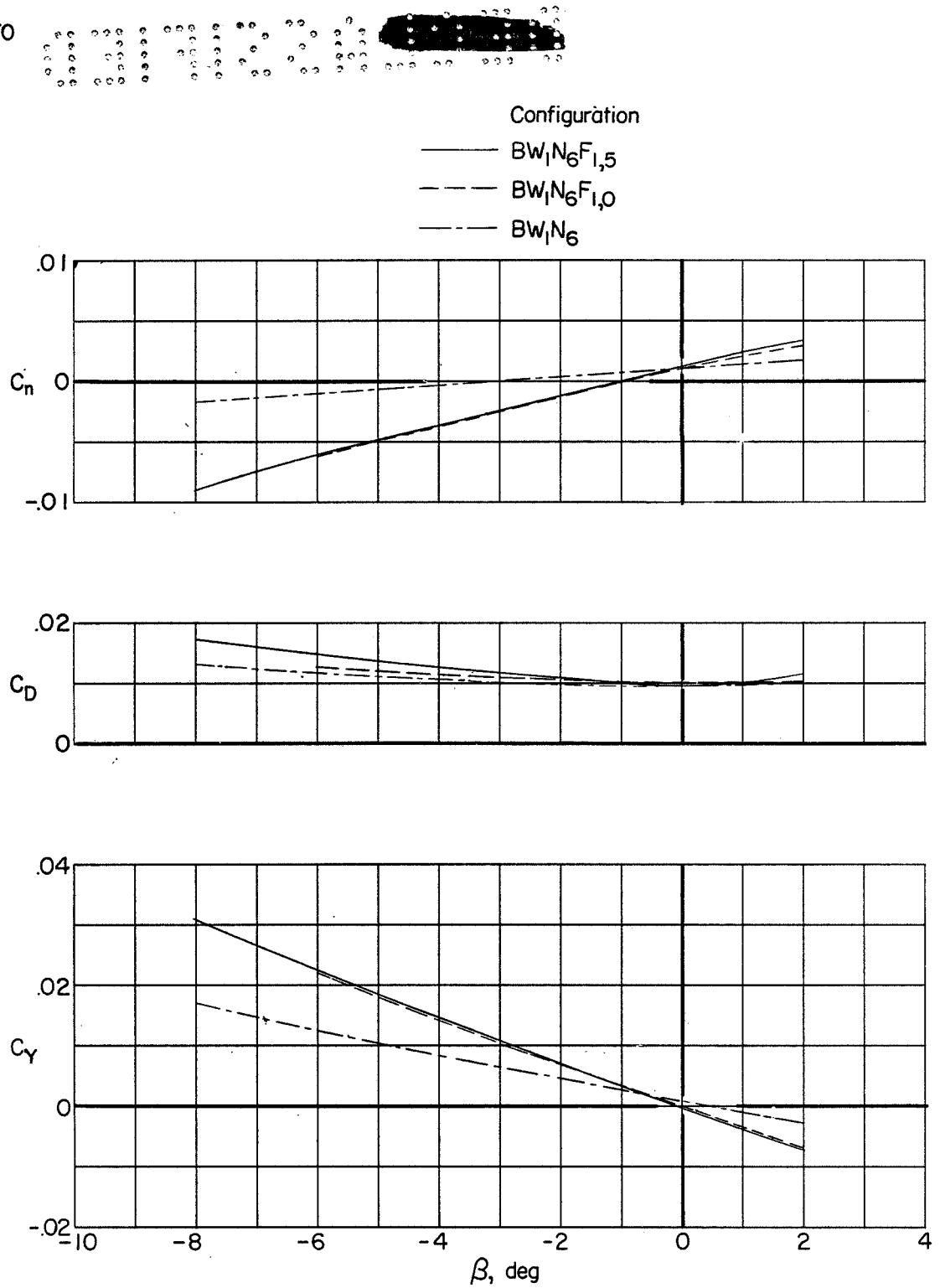


Figure 17.- Effect of tip fins on the lateral characteristics of the low-aspect-ratio arrow-wing configuration. $\alpha = 0^\circ$.

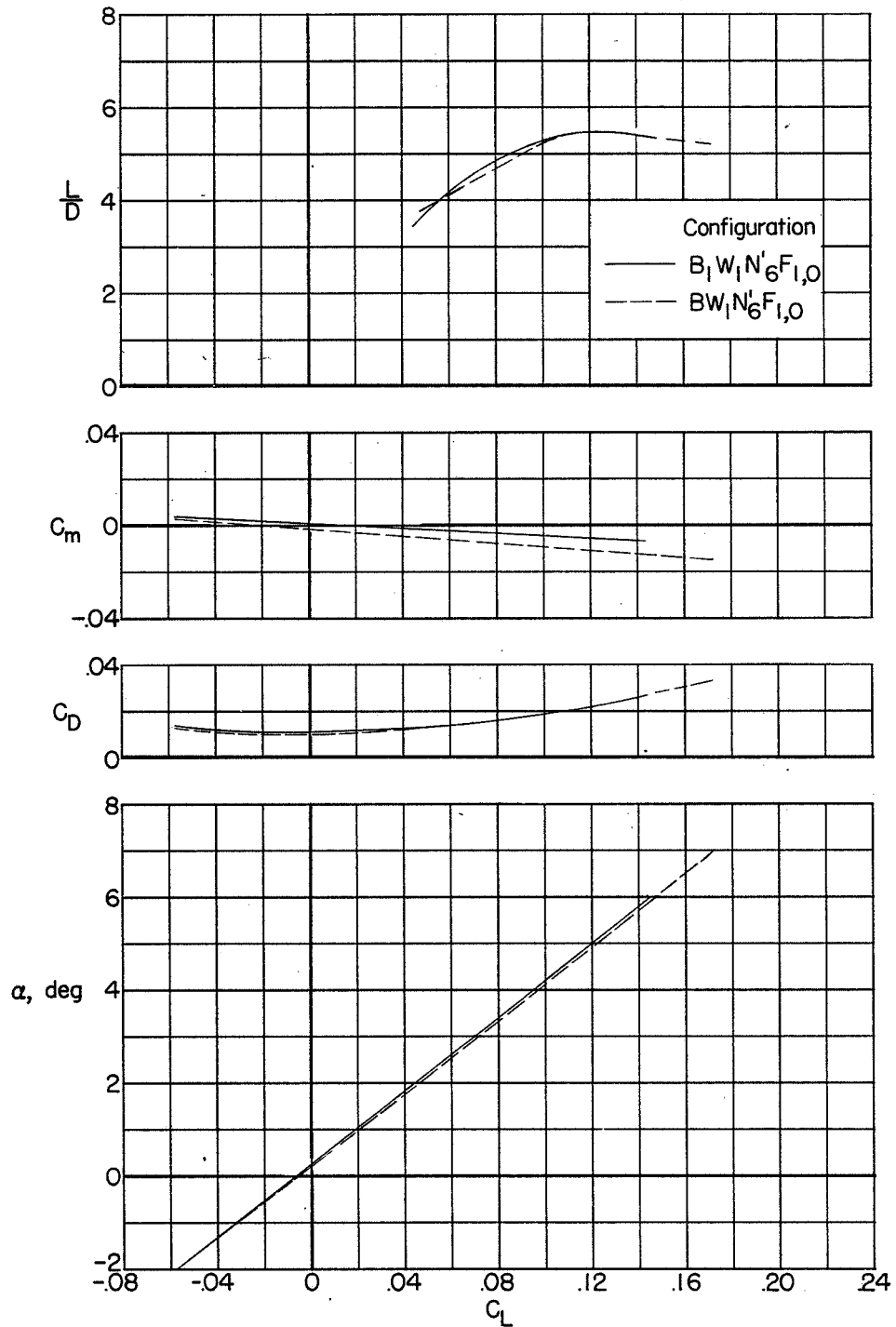


Figure 18.- Effects of fuselage shape on the longitudinal characteristics of the low-aspect-ratio arrow-wing configuration.

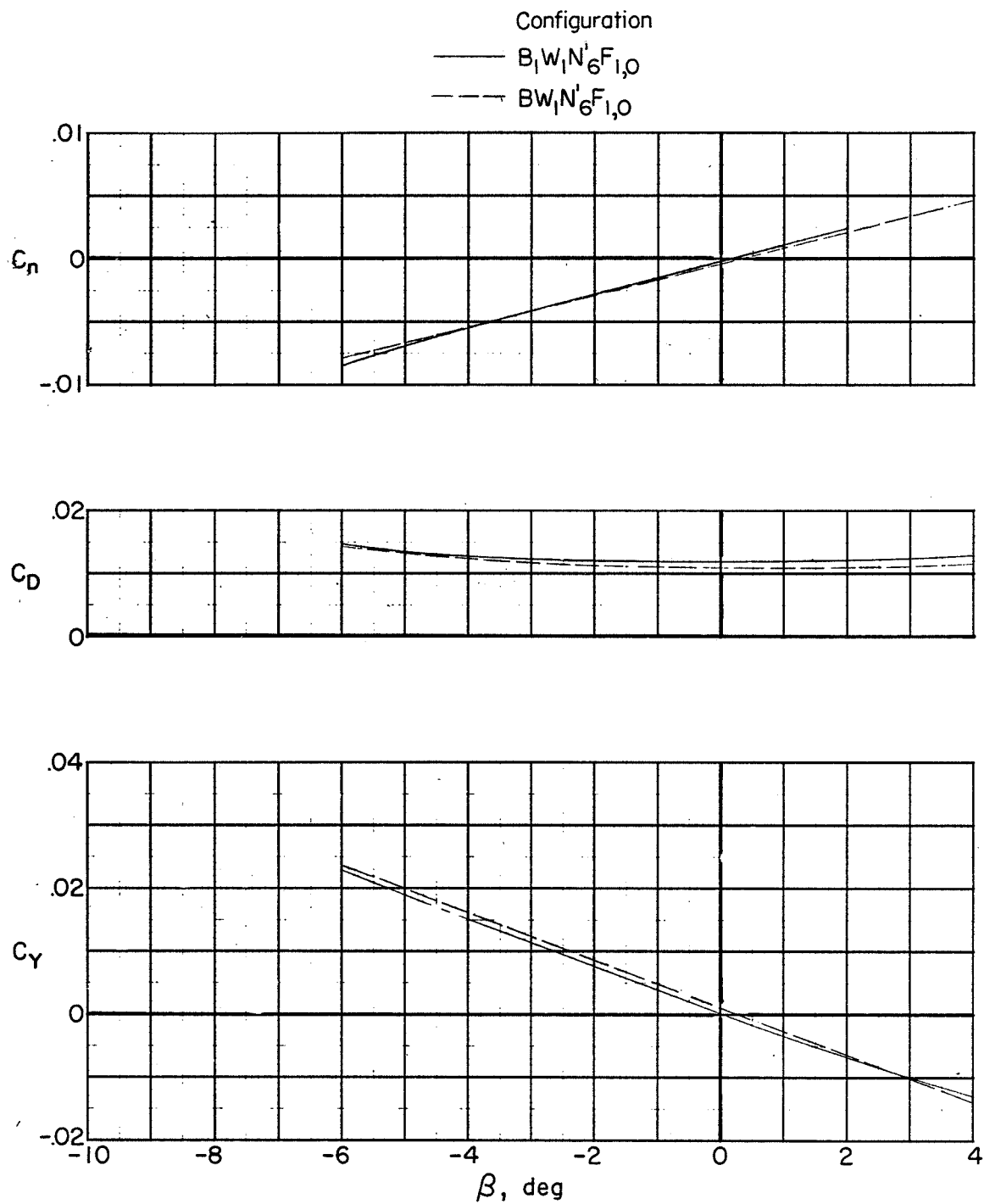


Figure 19.- Effect of fuselage shape on the lateral characteristics of the low-aspect-ratio arrow-wing configuration.

L-183

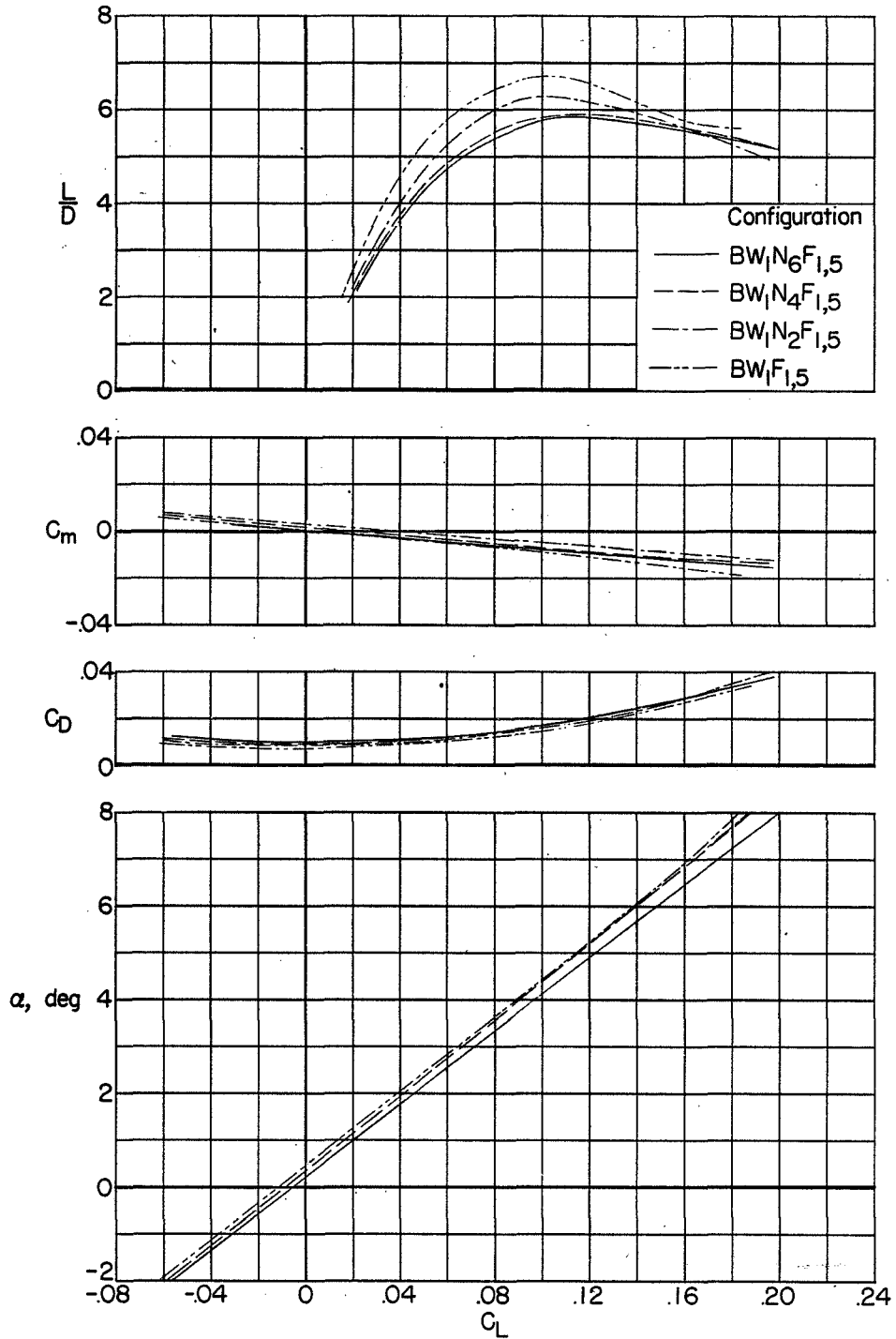
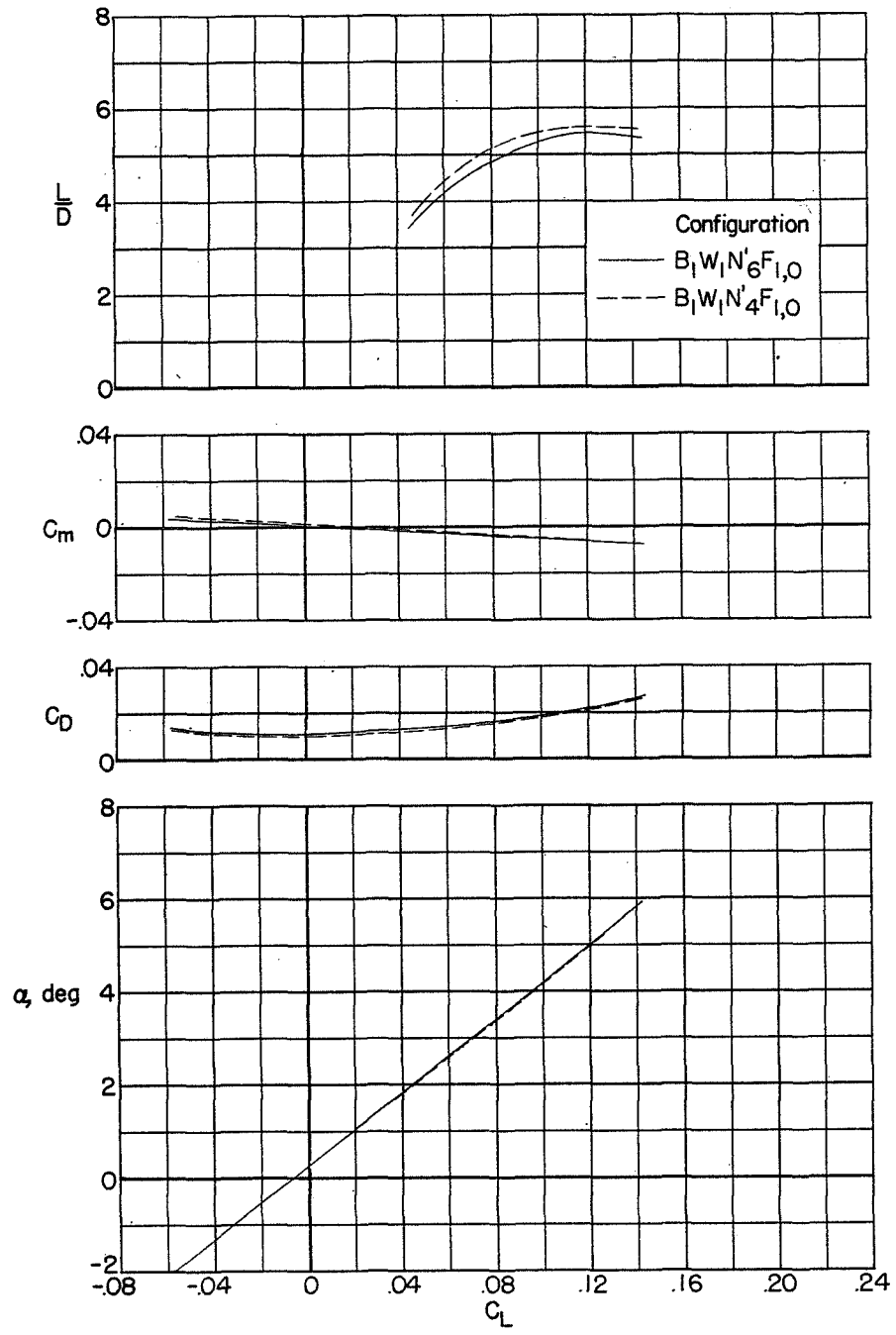


Figure 20.- Effects of nacelles on the longitudinal characteristics of the low-aspect-ratio arrow-wing configuration.

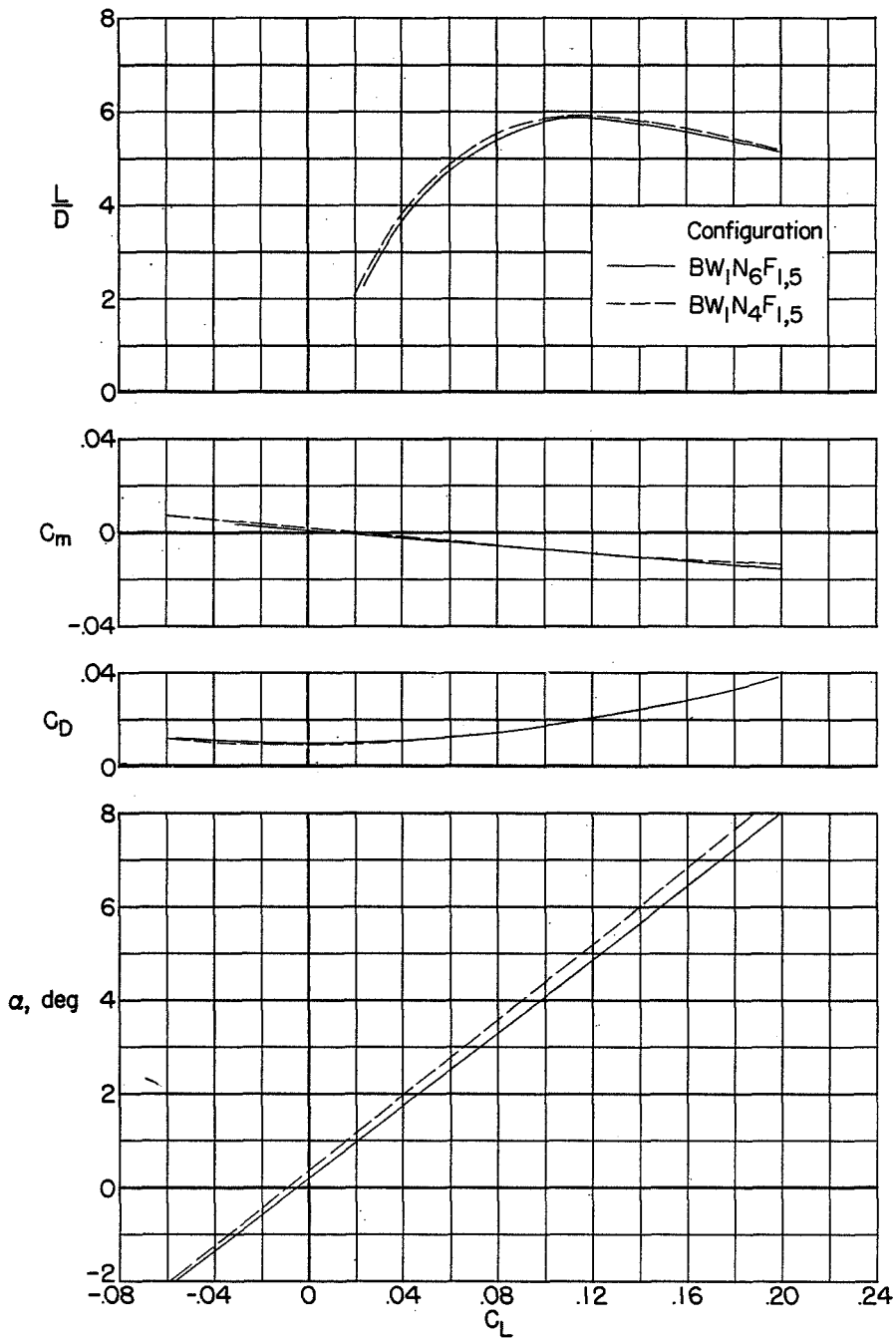


(a) 2/3-power half-body configuration.

Figure 21.- Effect of removing the inboard nacelles on the longitudinal characteristics of the low-aspect-ratio arrow-wing configuration.



I-183



(b) Ogive-cylinder body configuration.

Figure 21.- Concluded.

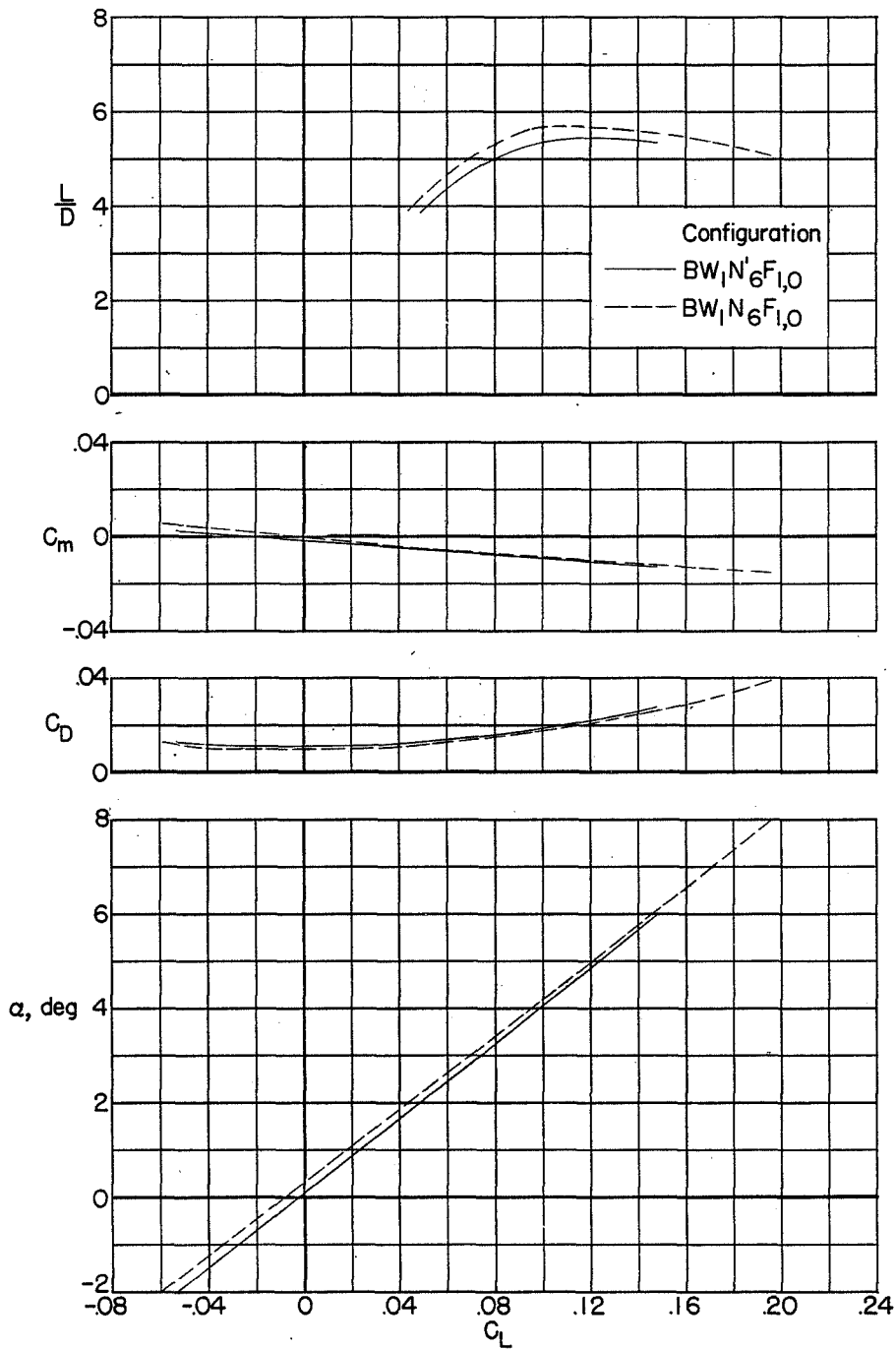


Figure 22.- Effect of moving nacelles outboard on the longitudinal characteristics of the low-aspect-ratio arrow-wing configuration.

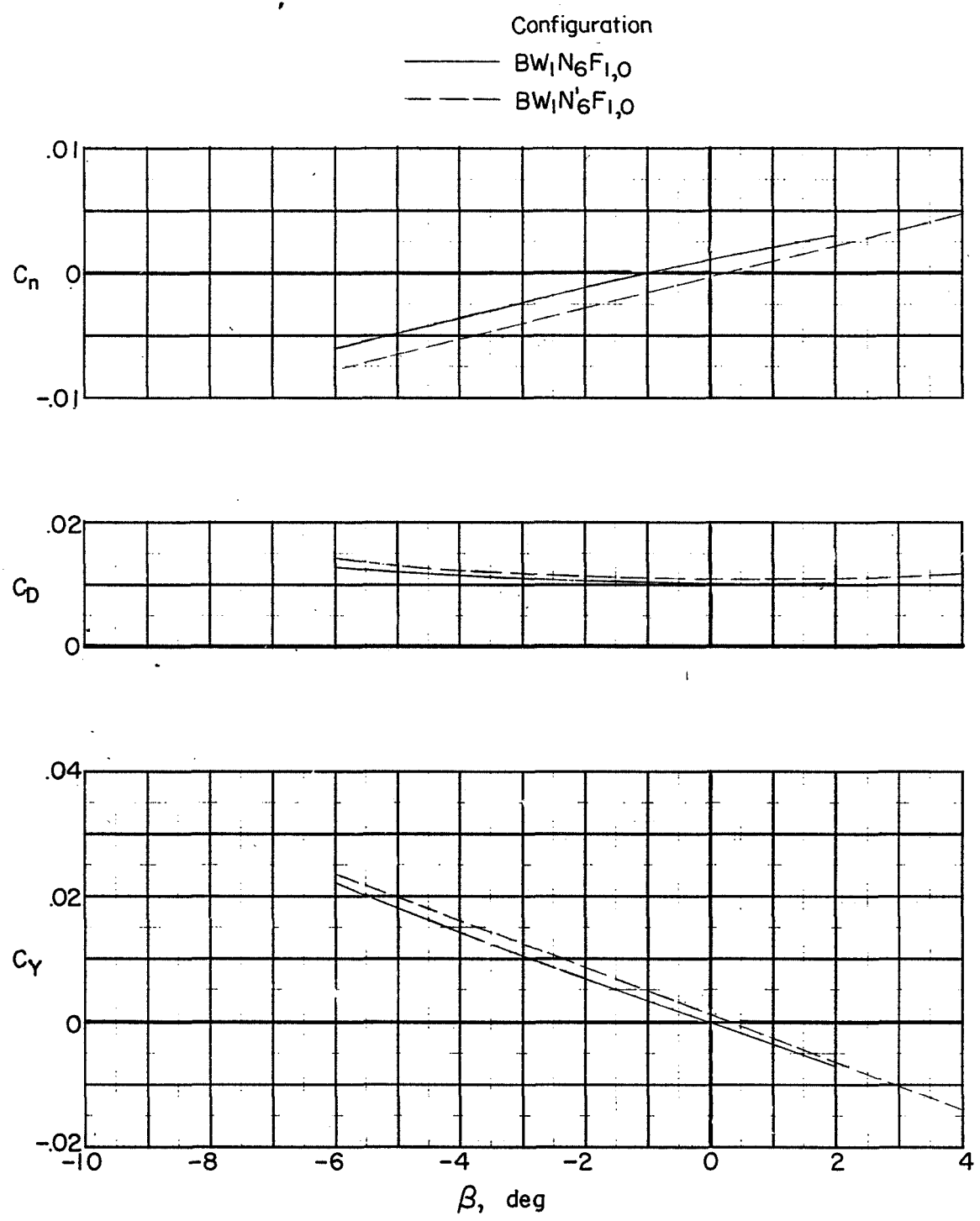
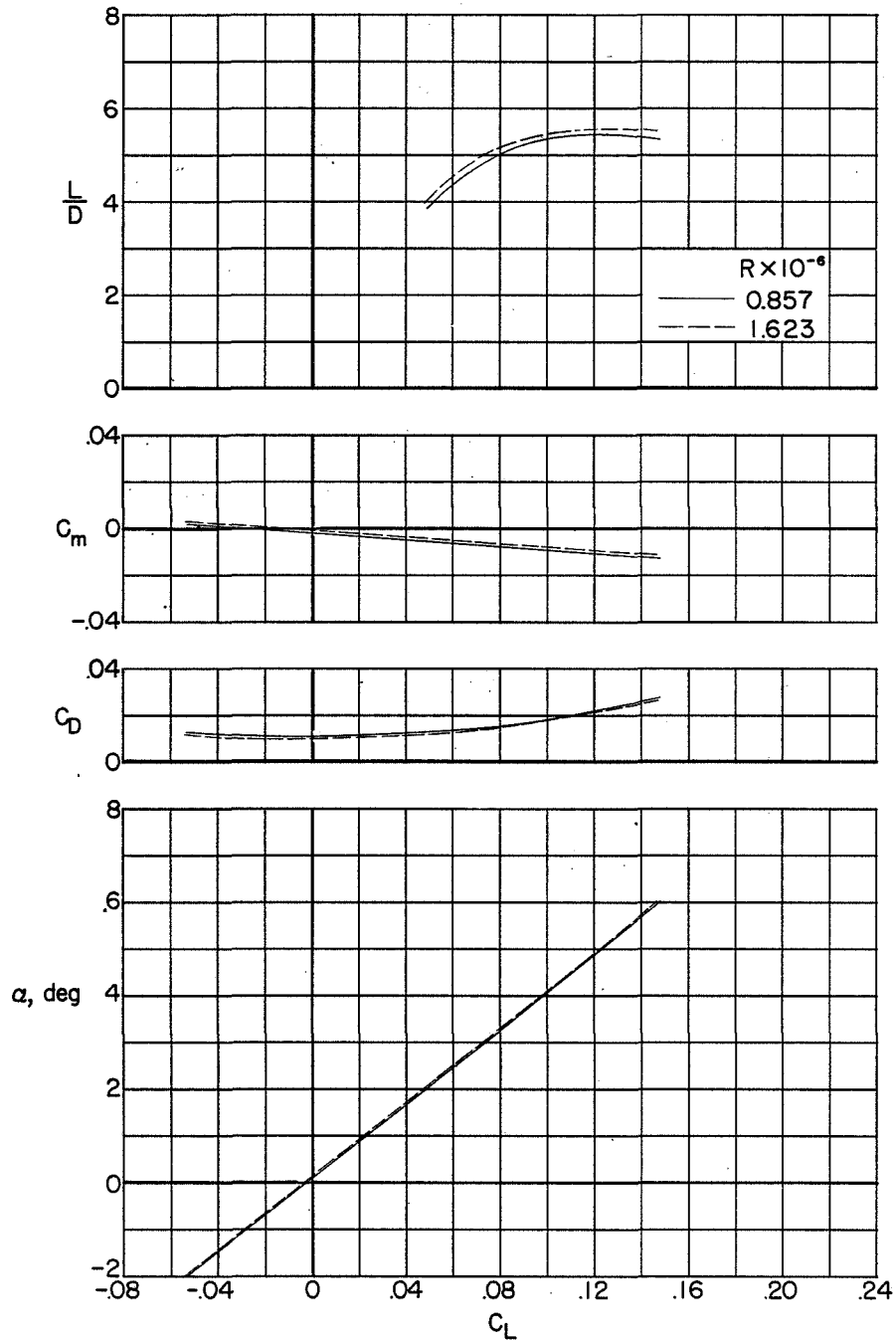
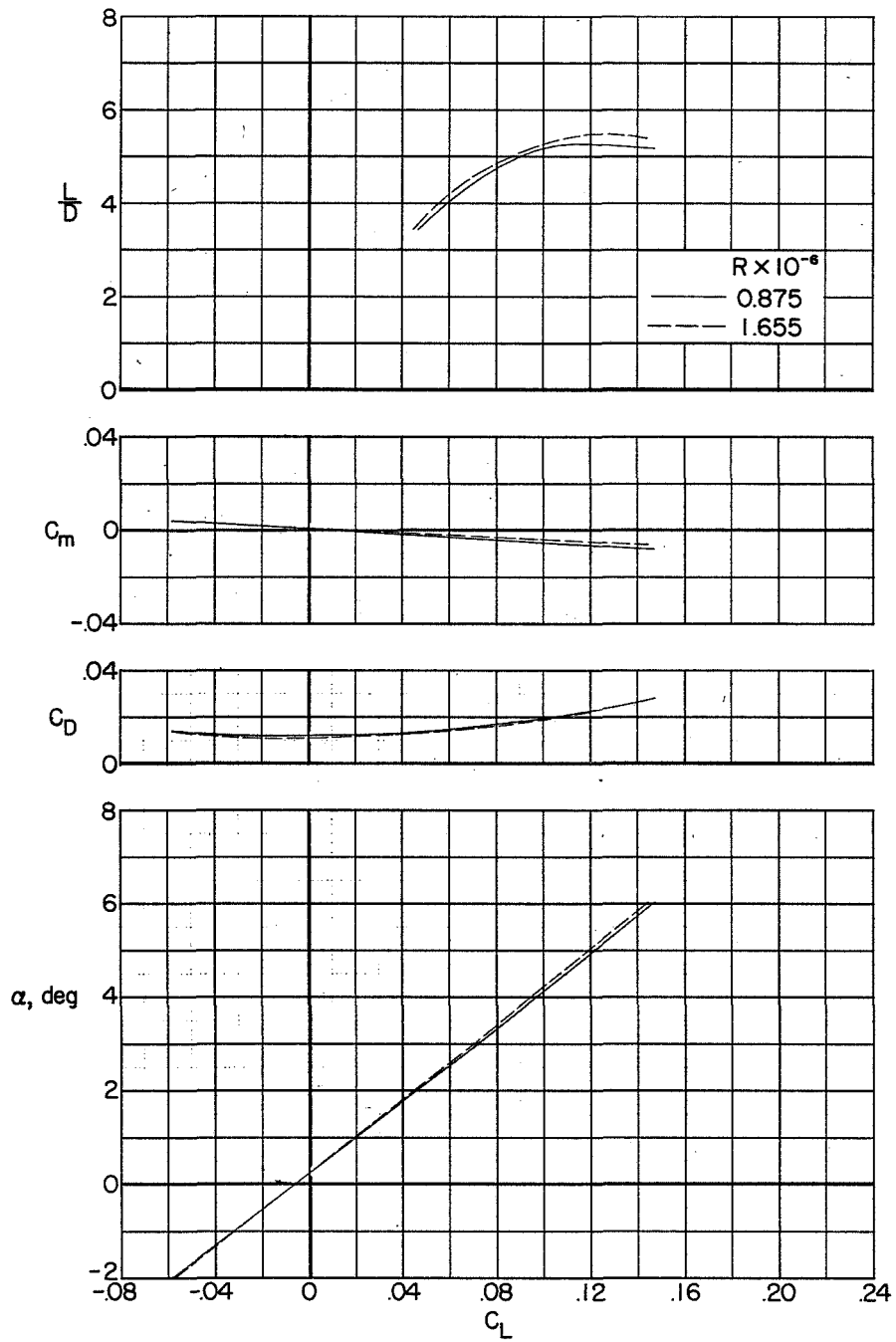


Figure 23.- Effect of moving nacelles outboard on the lateral characteristics of the low-aspect-ratio arrow-wing configuration.



(a) BW₁N'6F_{1,0}

Figure 24.- Effect of Reynolds number on the longitudinal characteristics of the low-aspect-ratio arrow-wing configuration.



(b) $B_1 W_1 N'_{6F1,0}$

Figure 24.- Concluded.

B₂W₂N₆F₂0

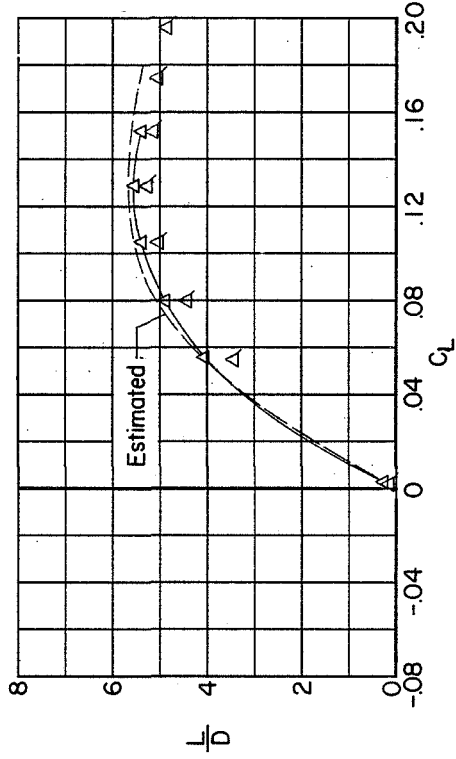
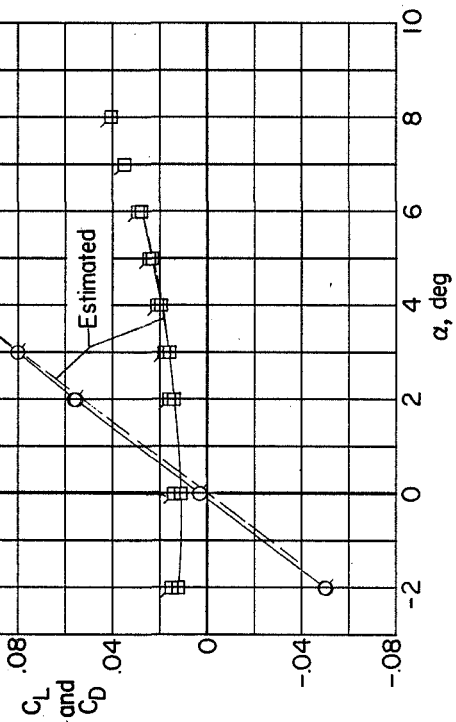
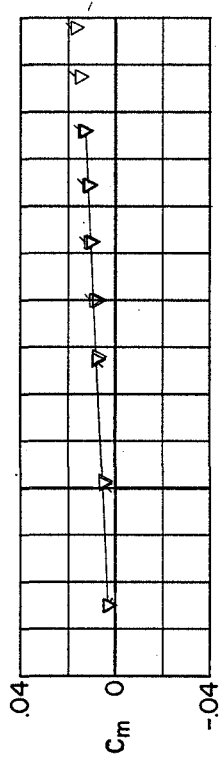
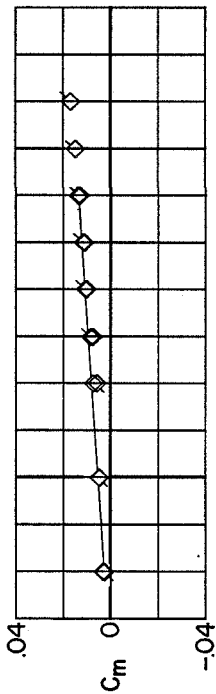


Figure 25.- Measured aerodynamic characteristics in pitch of the high-aspect-ratio arrow-wing configuration. B₂W₂N₆F₂0. (Flagged symbols denote fixed transition.)

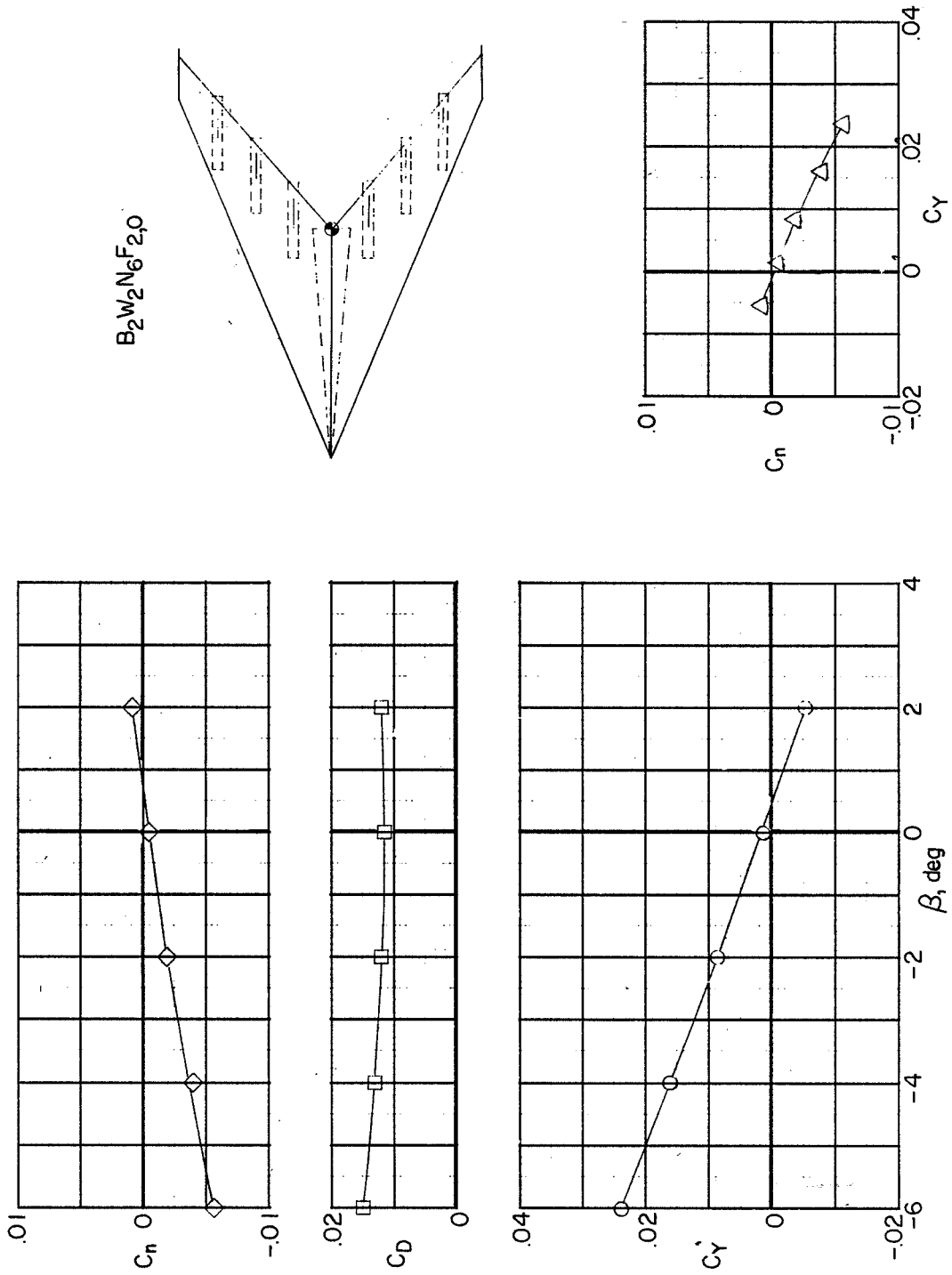


Figure 26.- Measured aerodynamic characteristics in sideslip of the high-aspect-ratio arrow-wing configuration. $B_2W_2N_6F_2,0$.

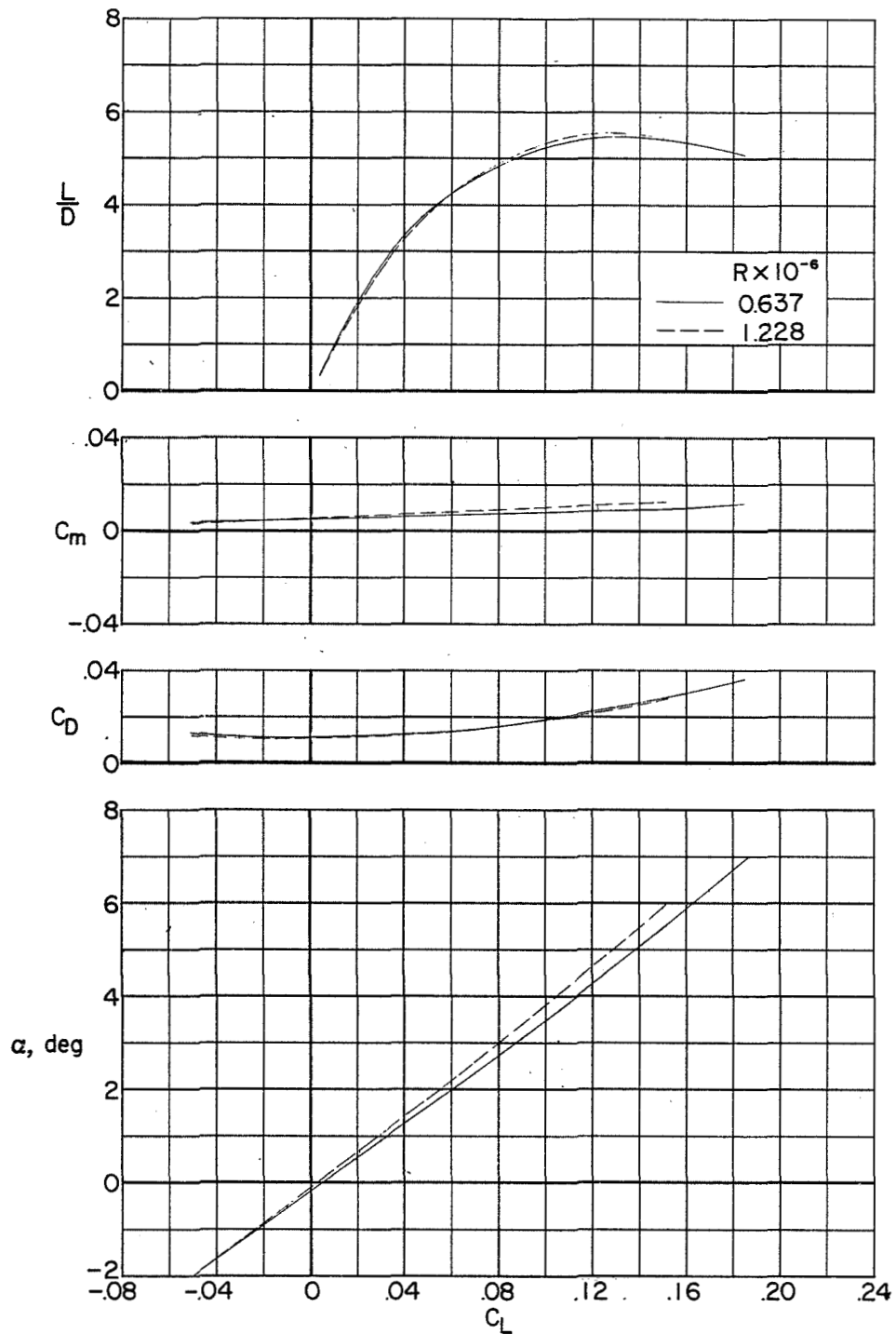
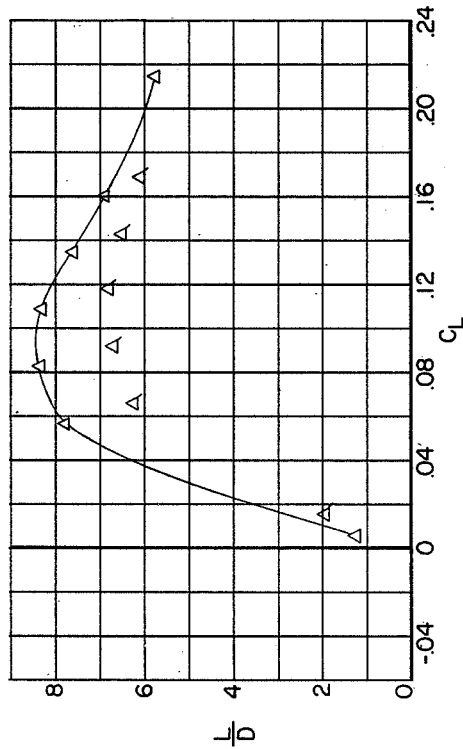
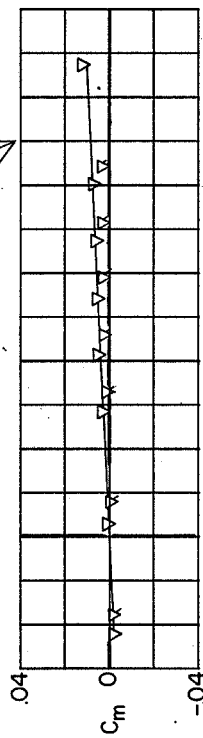
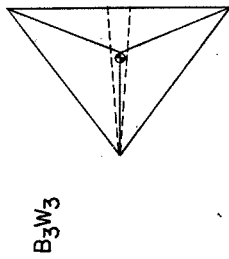
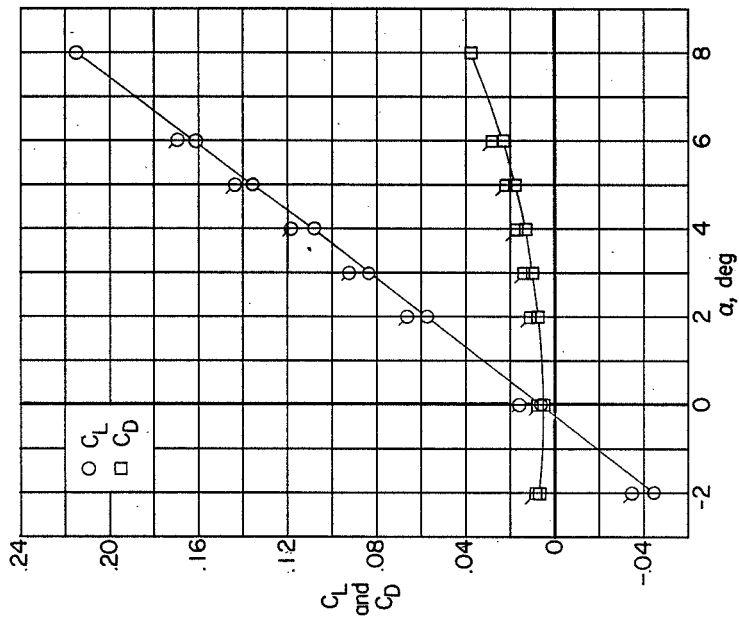
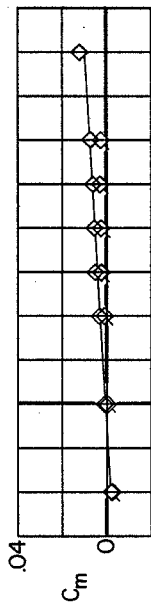
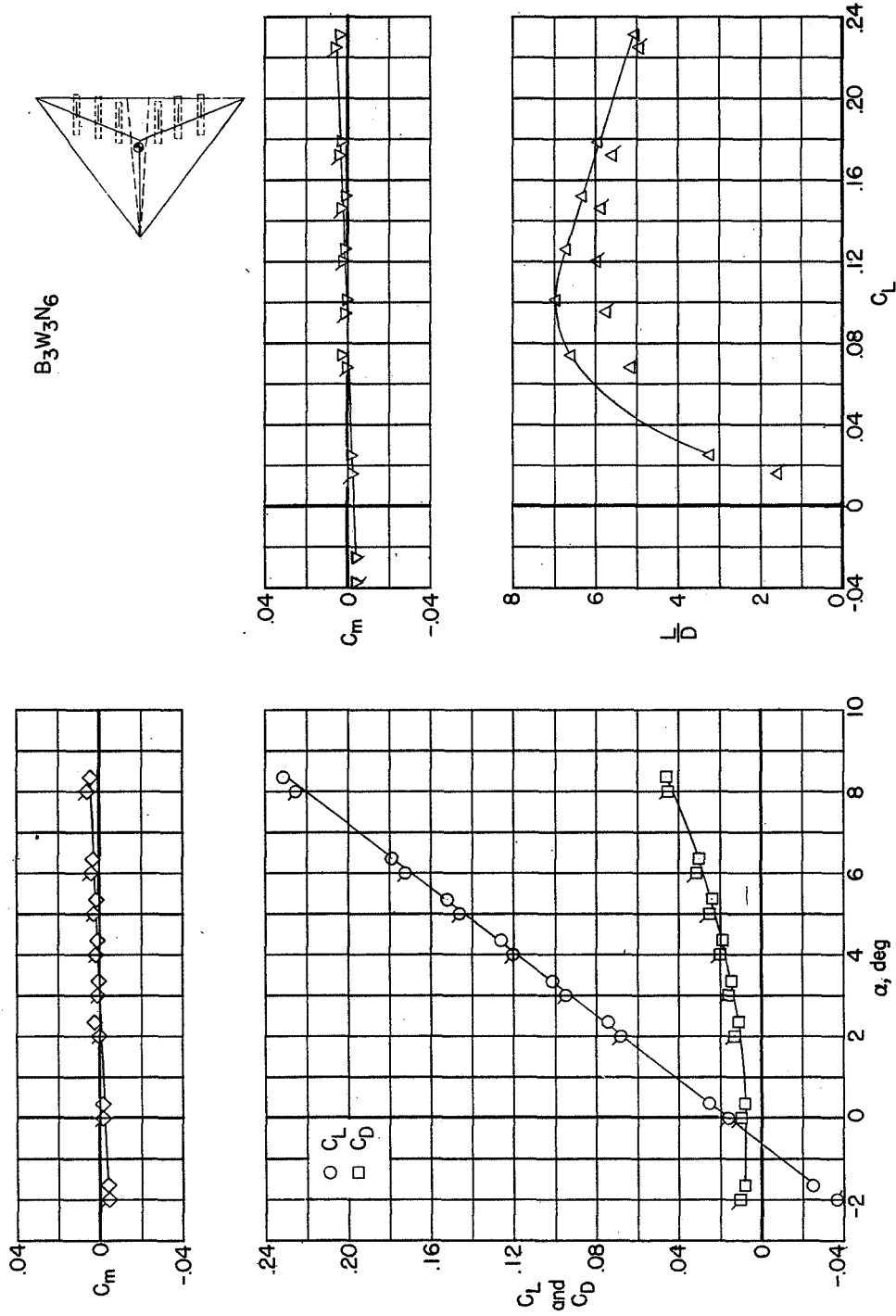


Figure 27.- Effects of Reynolds number on the longitudinal characteristics of the high-aspect-ratio arrow-wing configuration. $B_2W_2N_6F_2,0$.



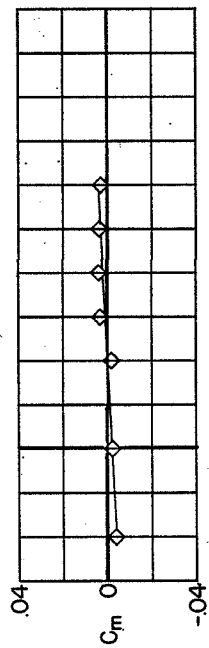
(a) B_3W_3 .

Figure 28.- Measured aerodynamic characteristics in pitch of the delta-wing configuration.
(Flagged symbols denote fixed transition.)

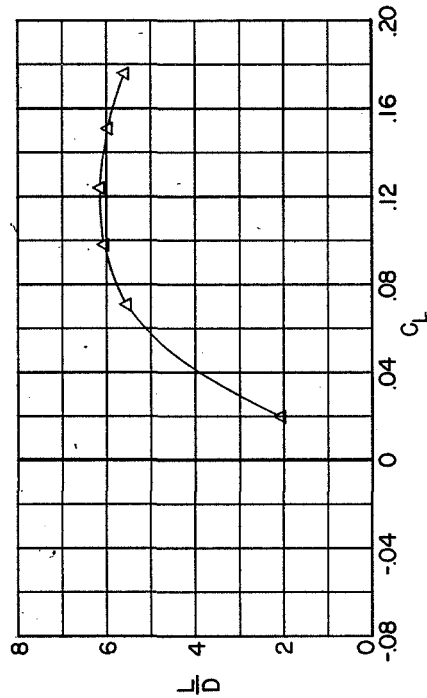
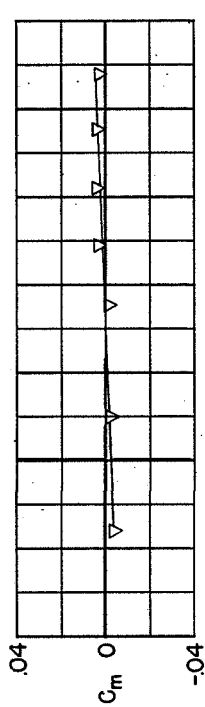
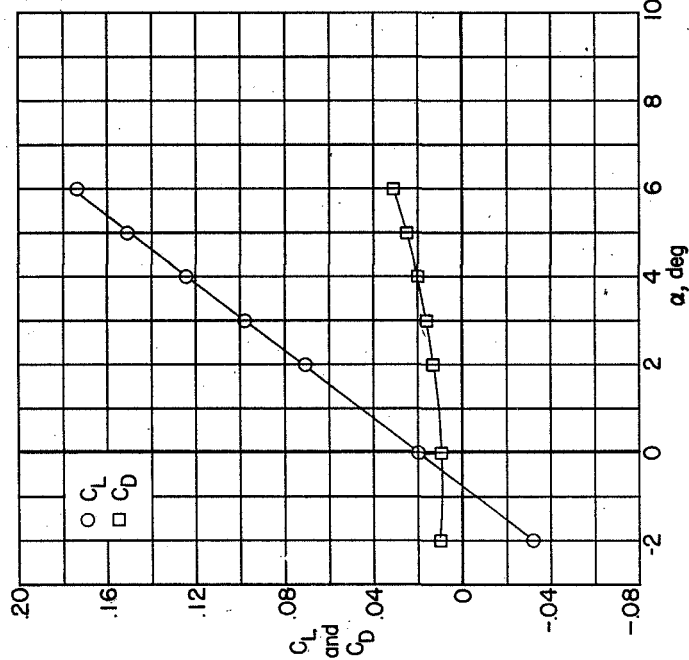
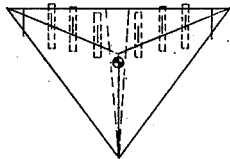


(b) $B_3W_3N_6$.

Figure 28.- Continued.



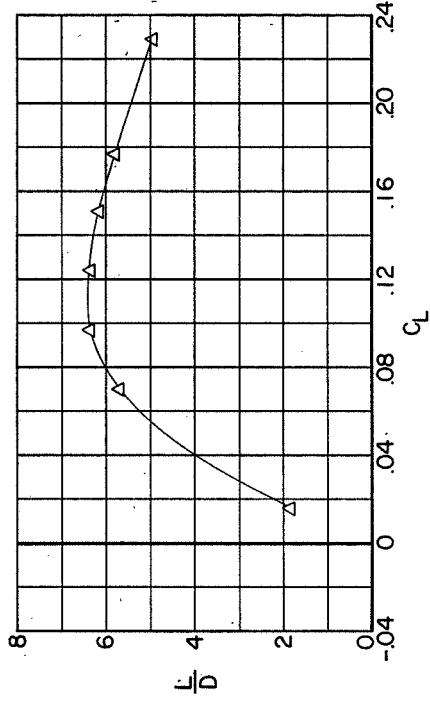
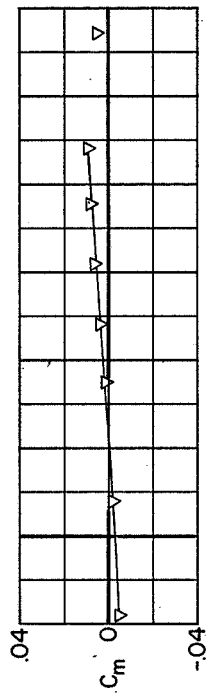
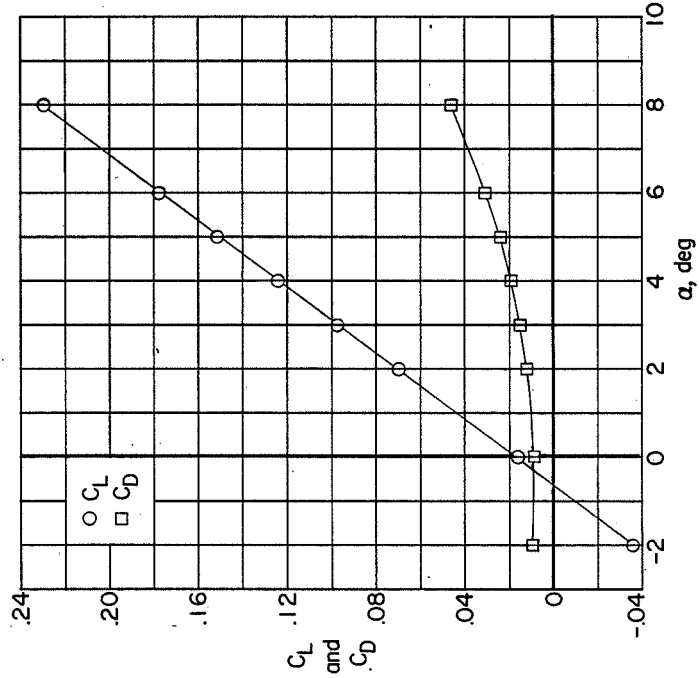
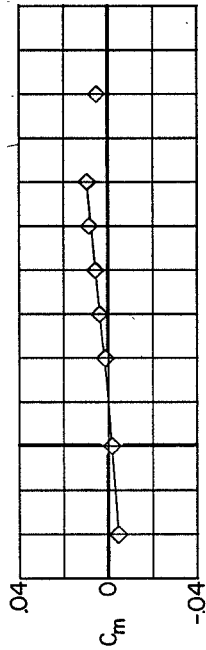
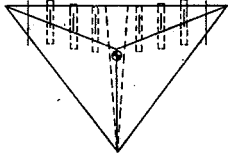
B₃W₃N₆FS



(c) B₃W₃N₆FS.

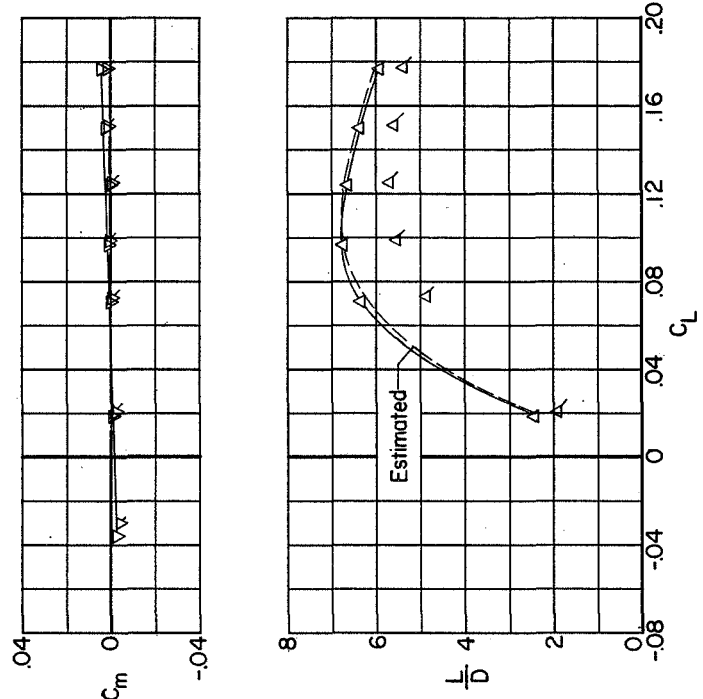
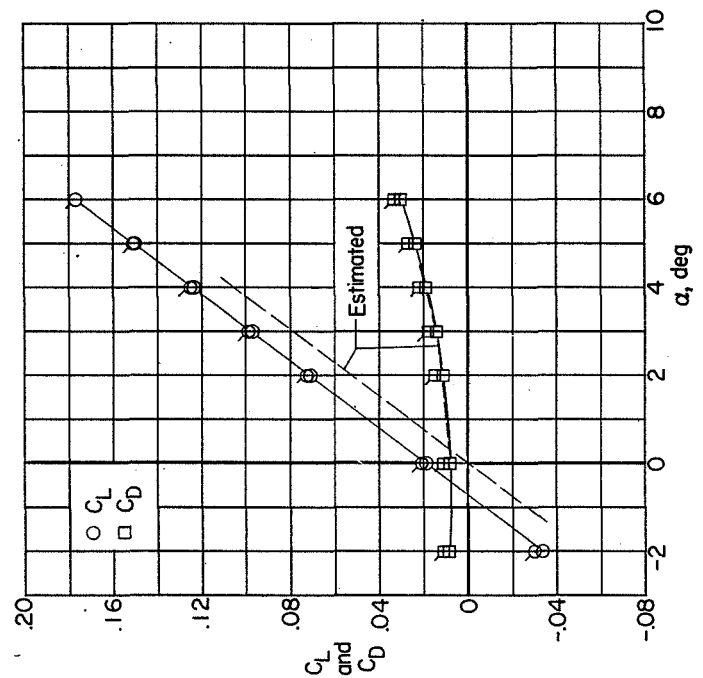
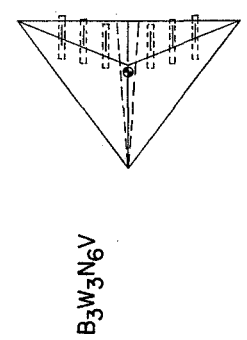
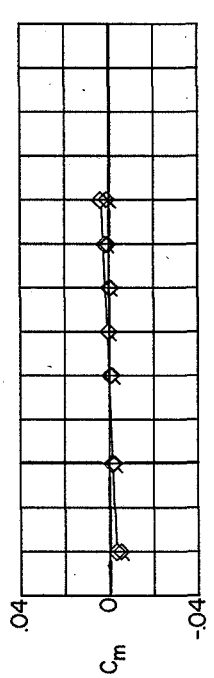
Figure 28.- Continued.

B₃W₃N₆FL



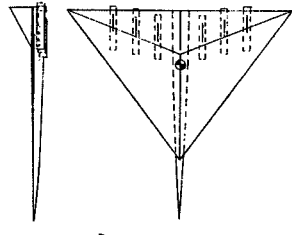
(a) B₃W₃N₆FL.

Figure 28.- Continued.

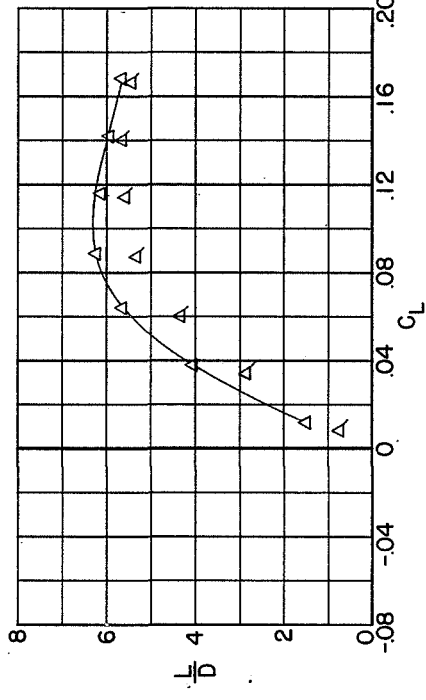
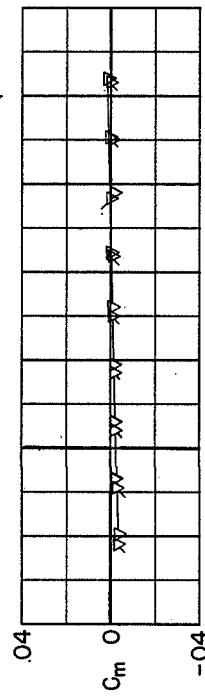
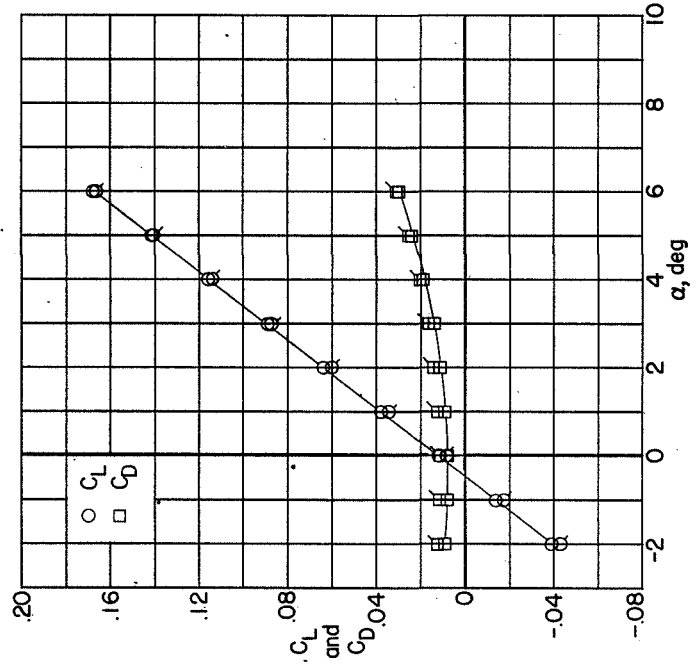
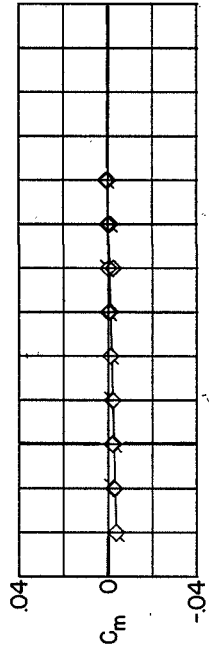


(e) $B_3W_3N_6V$.

Figure 28.- Continued.

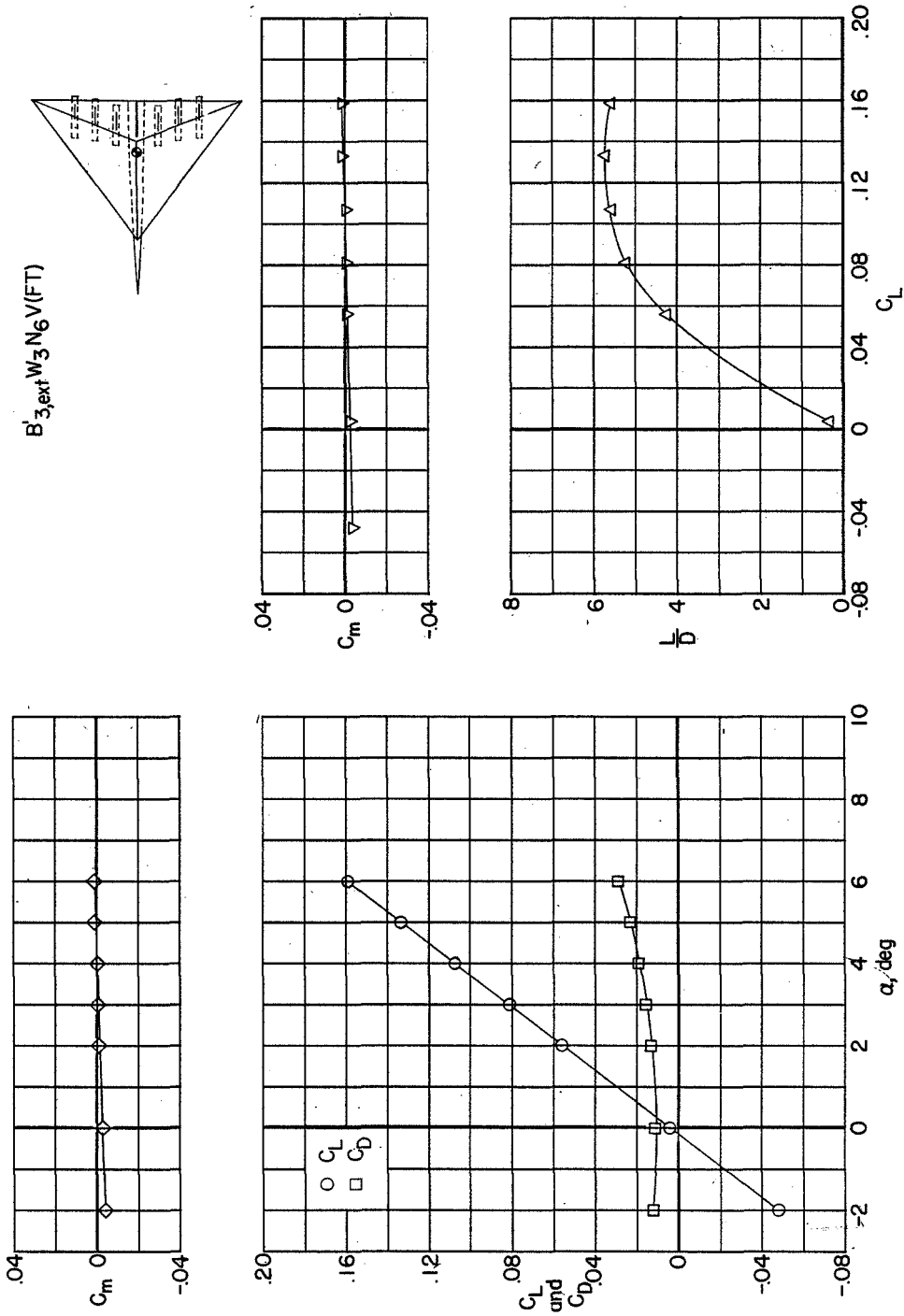


B_{3,ext}W₃N₆V



(f) B_{3,ext}W₃N₆V.

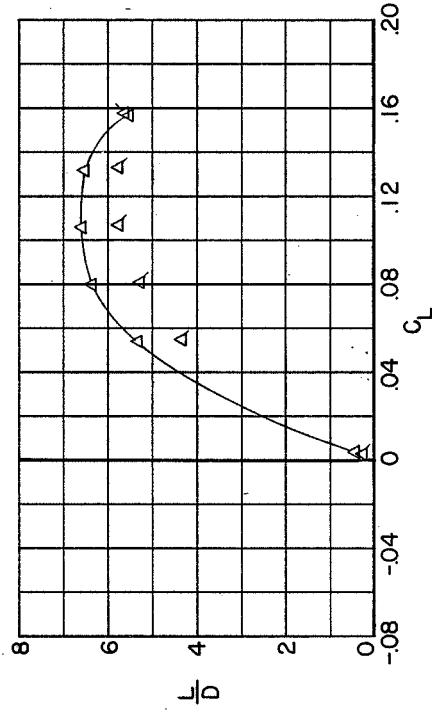
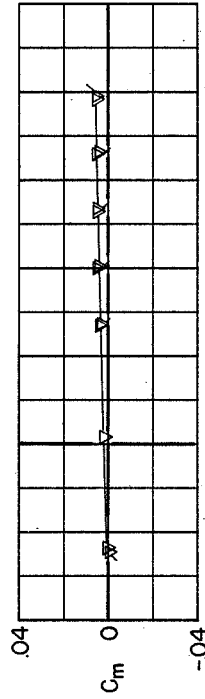
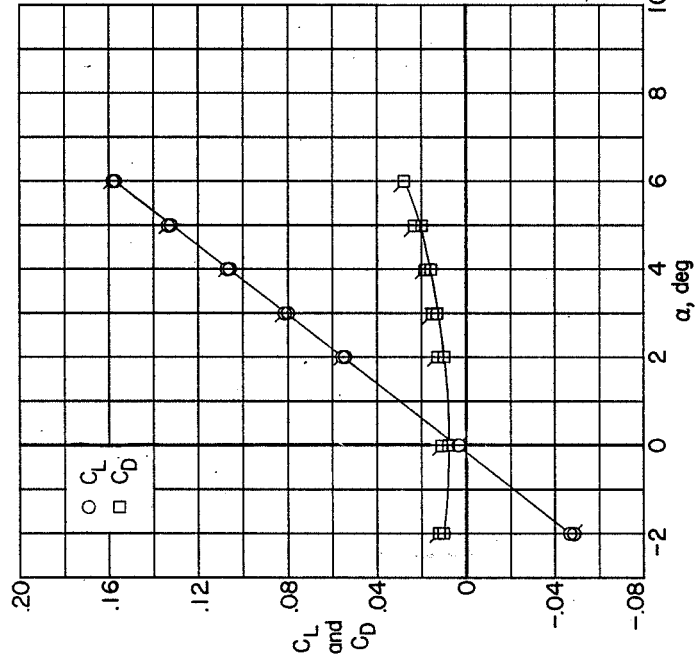
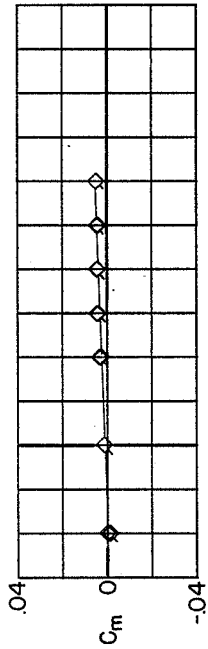
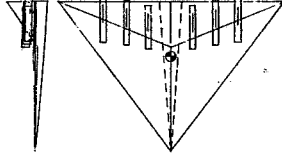
Figure 28.- Continued.



(g) $B'_{3,ext}W_3N_6V(FT)$.

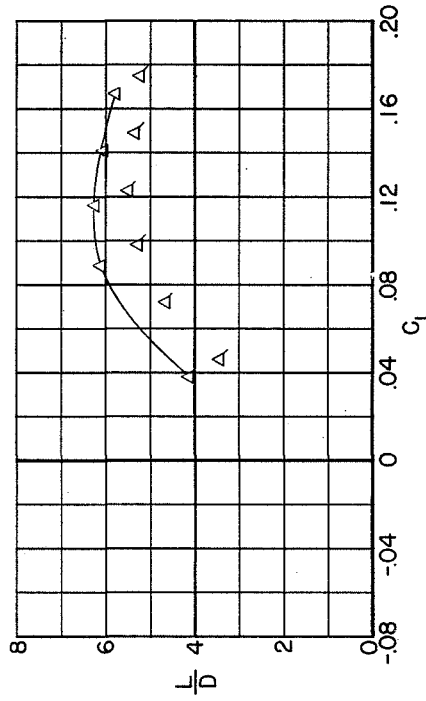
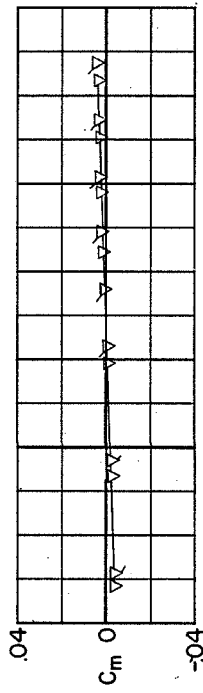
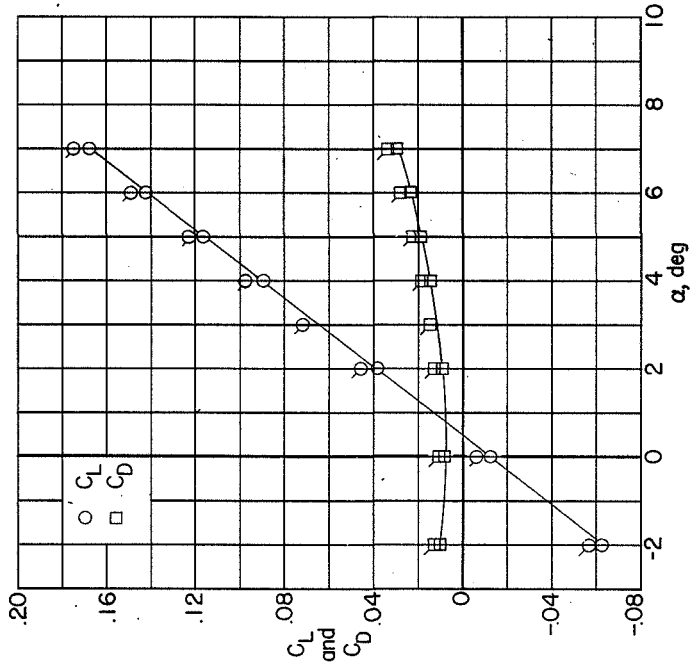
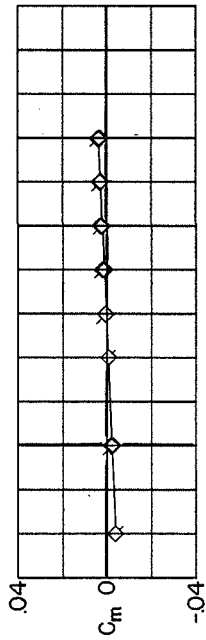
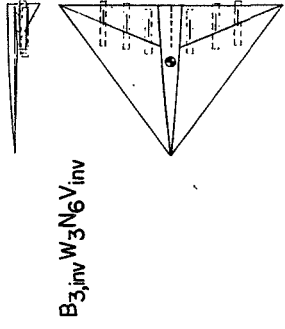
Figure 28.- Continued.

B₃W₃N₆, inv V



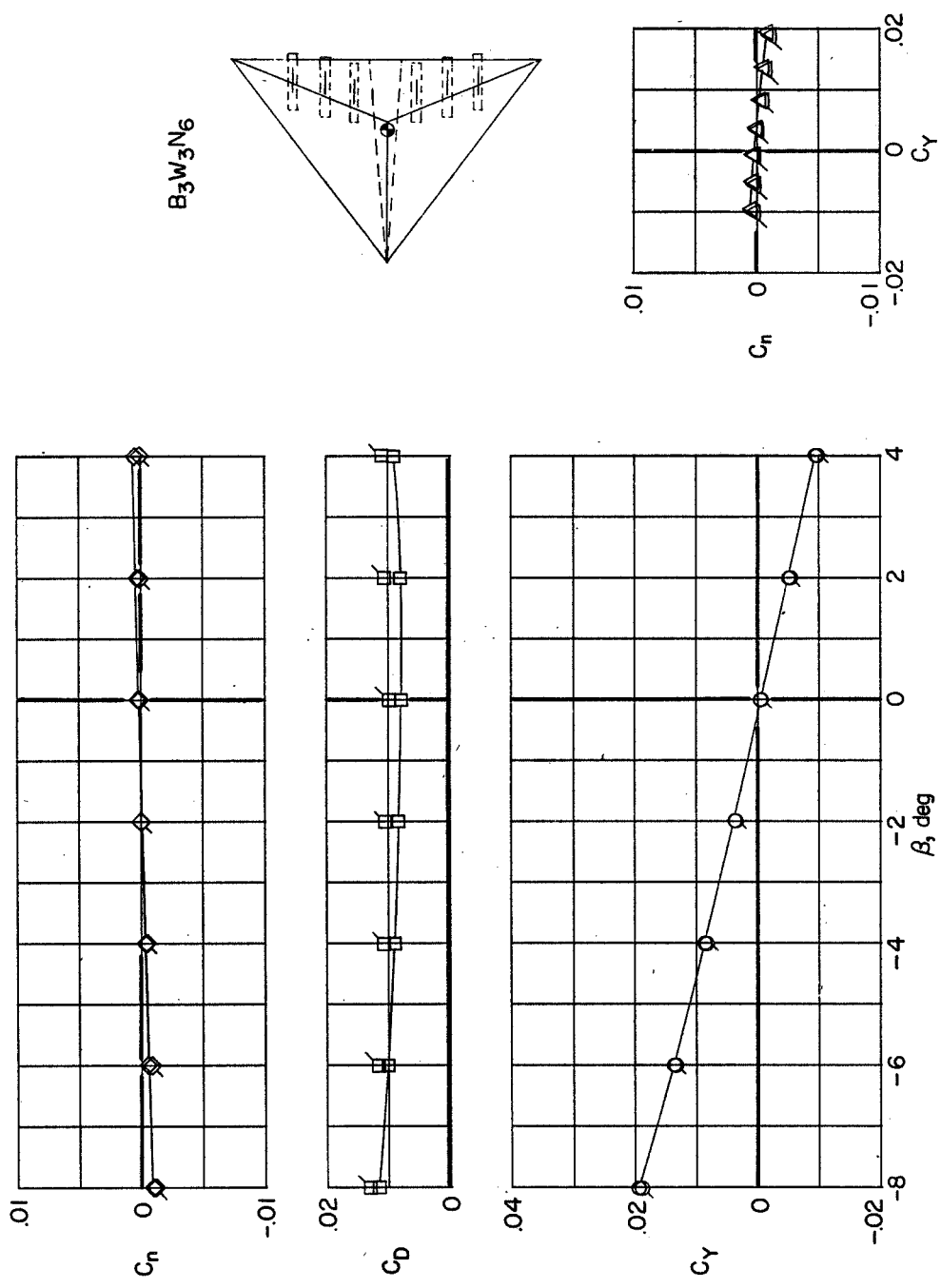
(h) B₃W₃N₆, inv V.

Figure 28.- Continued.



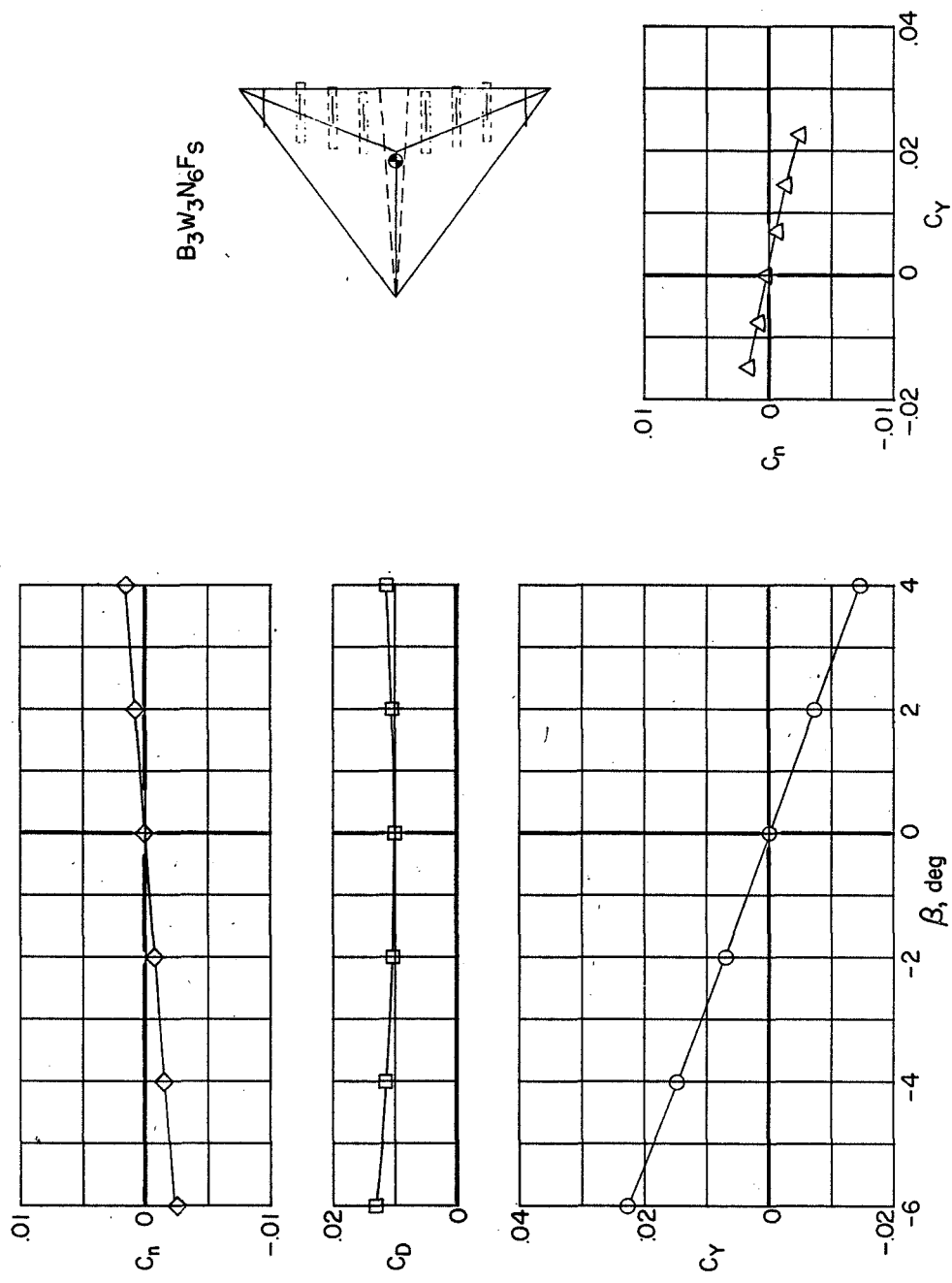
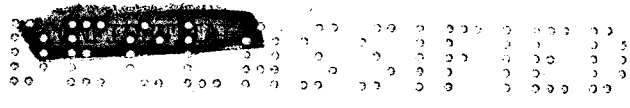
(1) $B_{3,inv}W_3N_6V_{inv}$.

Figure 28.- Concluded.



(a) $B_3W_3N_6$.

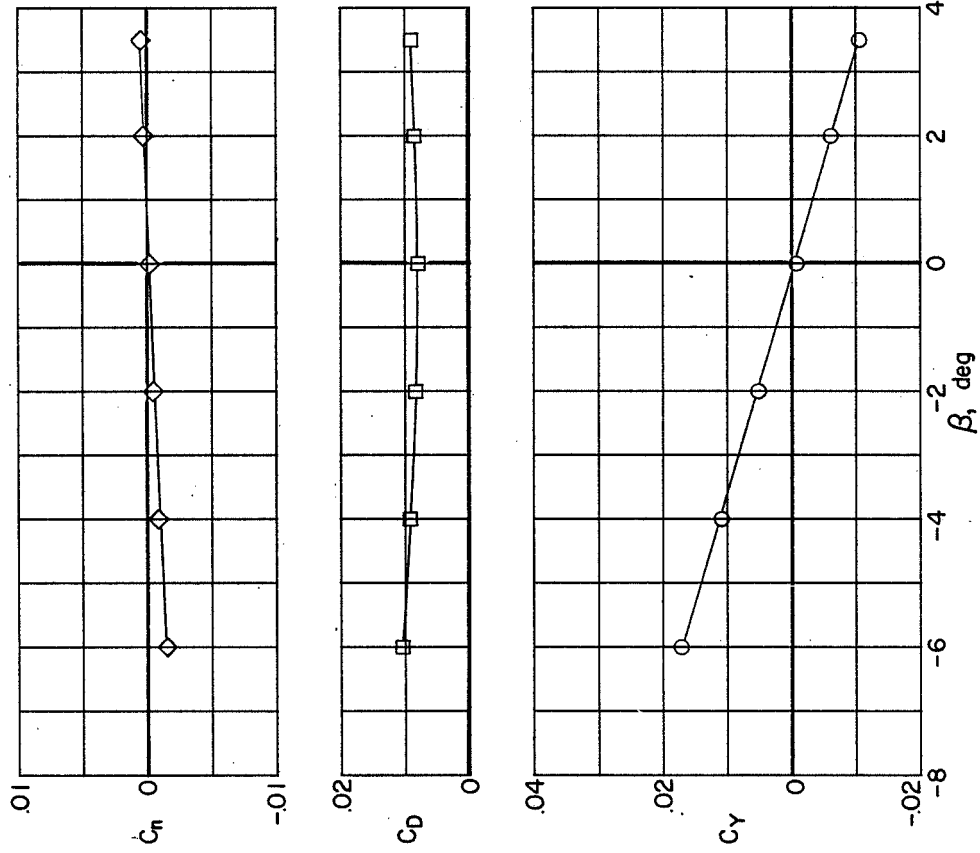
Figure 29.- Measured aerodynamic characteristics in sideslip of the delta-wing configuration.
(Flagged symbols denote fixed transition.)



(b) B₃W₃N₆FS.

Figure 29.- Continued.

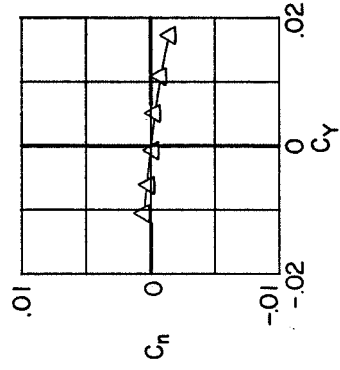
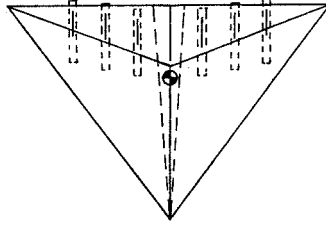




(a) $B_3W_3N_6V$.

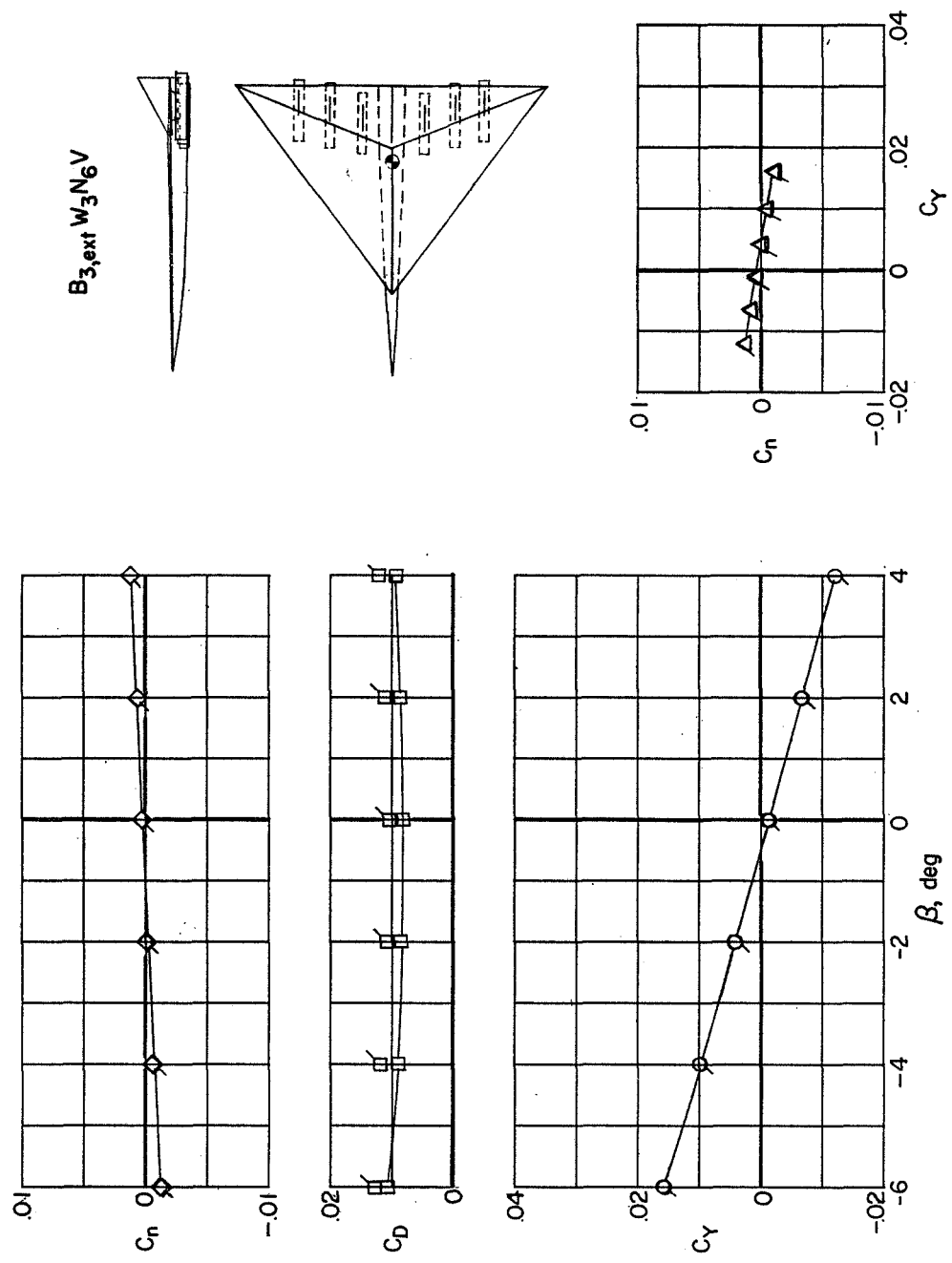
Figure 29.- Continued.

$B_3W_3N_6V$



0.037
0.036
0.035
0.034
0.033
0.032
0.031
0.030
0.029
0.028
0.027
0.026
0.025
0.024
0.023
0.022
0.021
0.020
0.019
0.018
0.017
0.016
0.015
0.014
0.013
0.012
0.011
0.010
0.009
0.008
0.007
0.006
0.005
0.004
0.003
0.002
0.001
0.000
-0.001
-0.002
-0.003
-0.004
-0.005
-0.006
-0.007
-0.008
-0.009
-0.010

$B_{3,ext} W_3 N_6 V$



(e) $B_{3,ext} W_3 N_6 V$.

Figure 29.- Concluded.

L-183

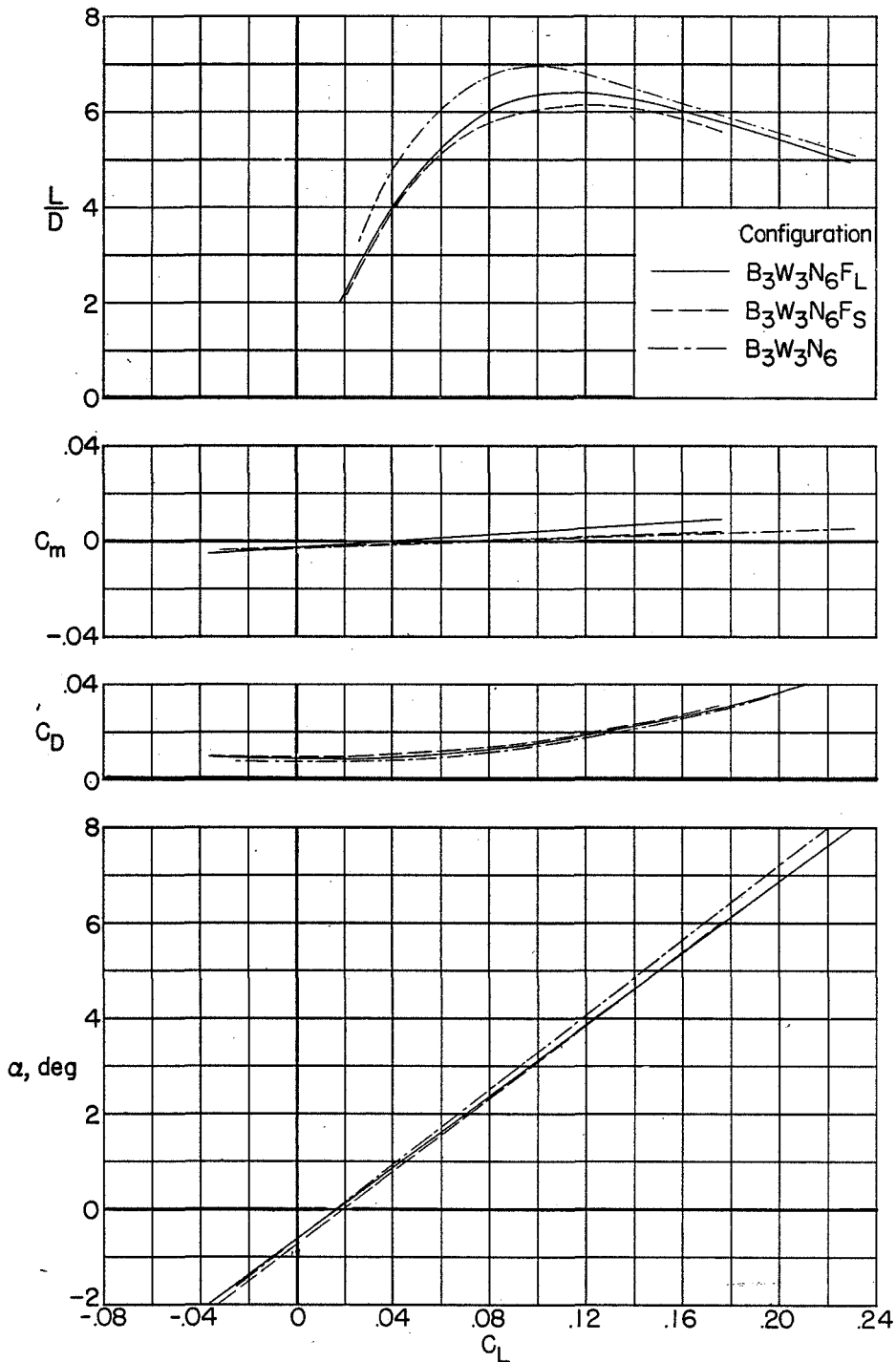


Figure 30.- Effect of tip fins on the longitudinal characteristics of the delta-wing configuration.

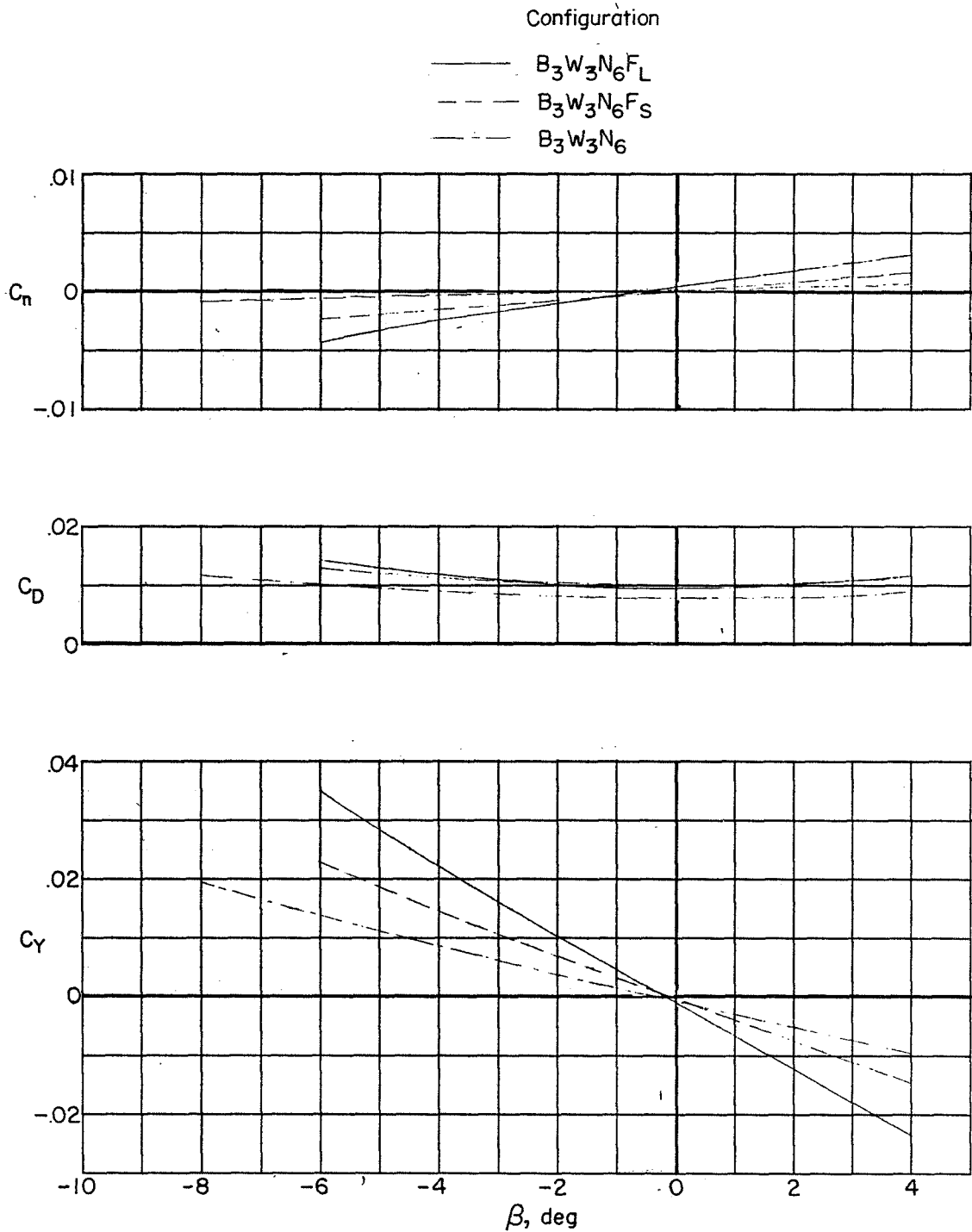


Figure 31.- Effect of tip fins on the lateral characteristics of the delta-wing configuration.

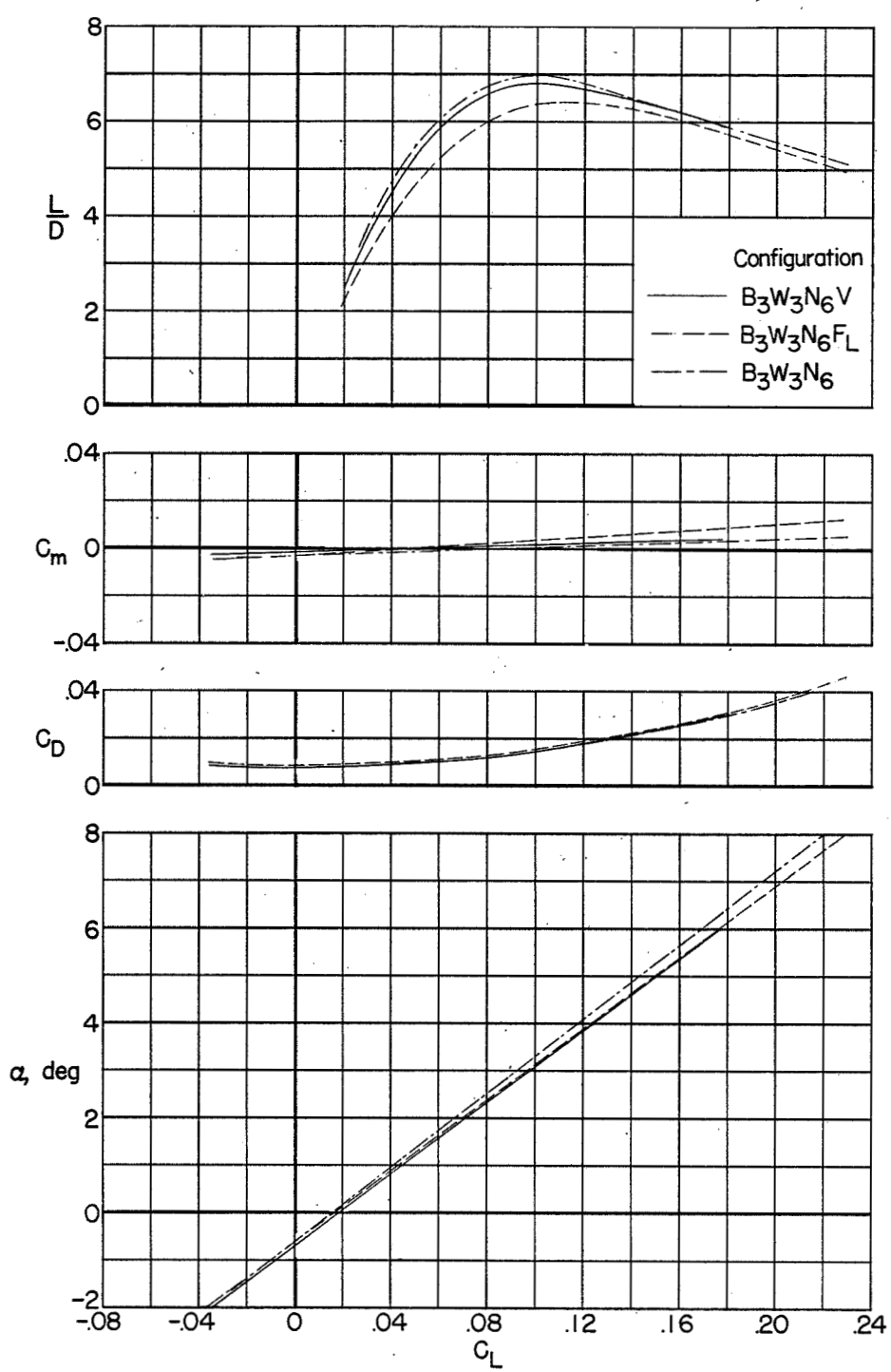


Figure 32.- Effect of vertical tail and large tip fins on the longitudinal characteristics of the delta-wing configuration.

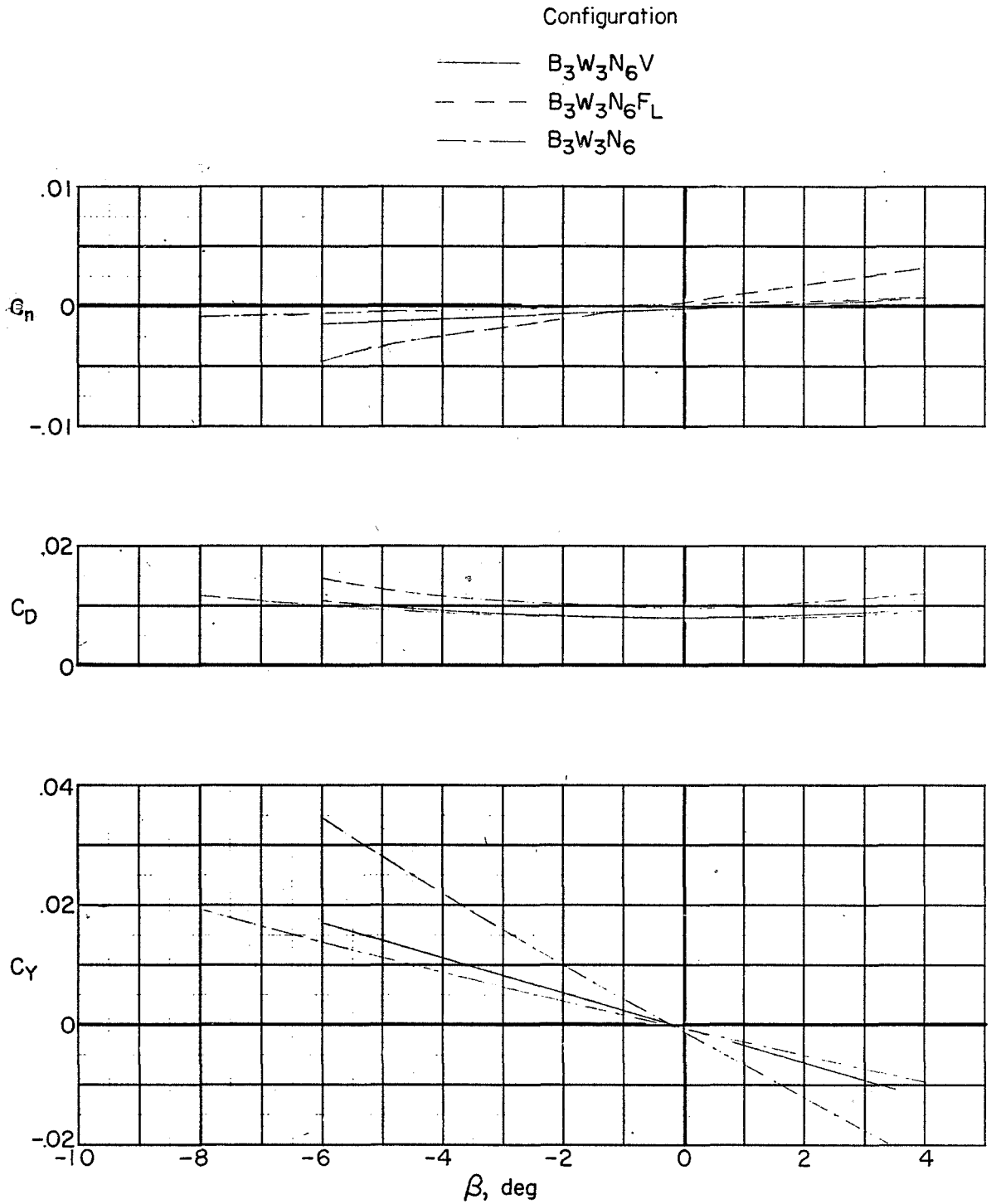


Figure 33.- Effect of vertical tail and large tip fins on the lateral characteristics of the delta-wing configuration.

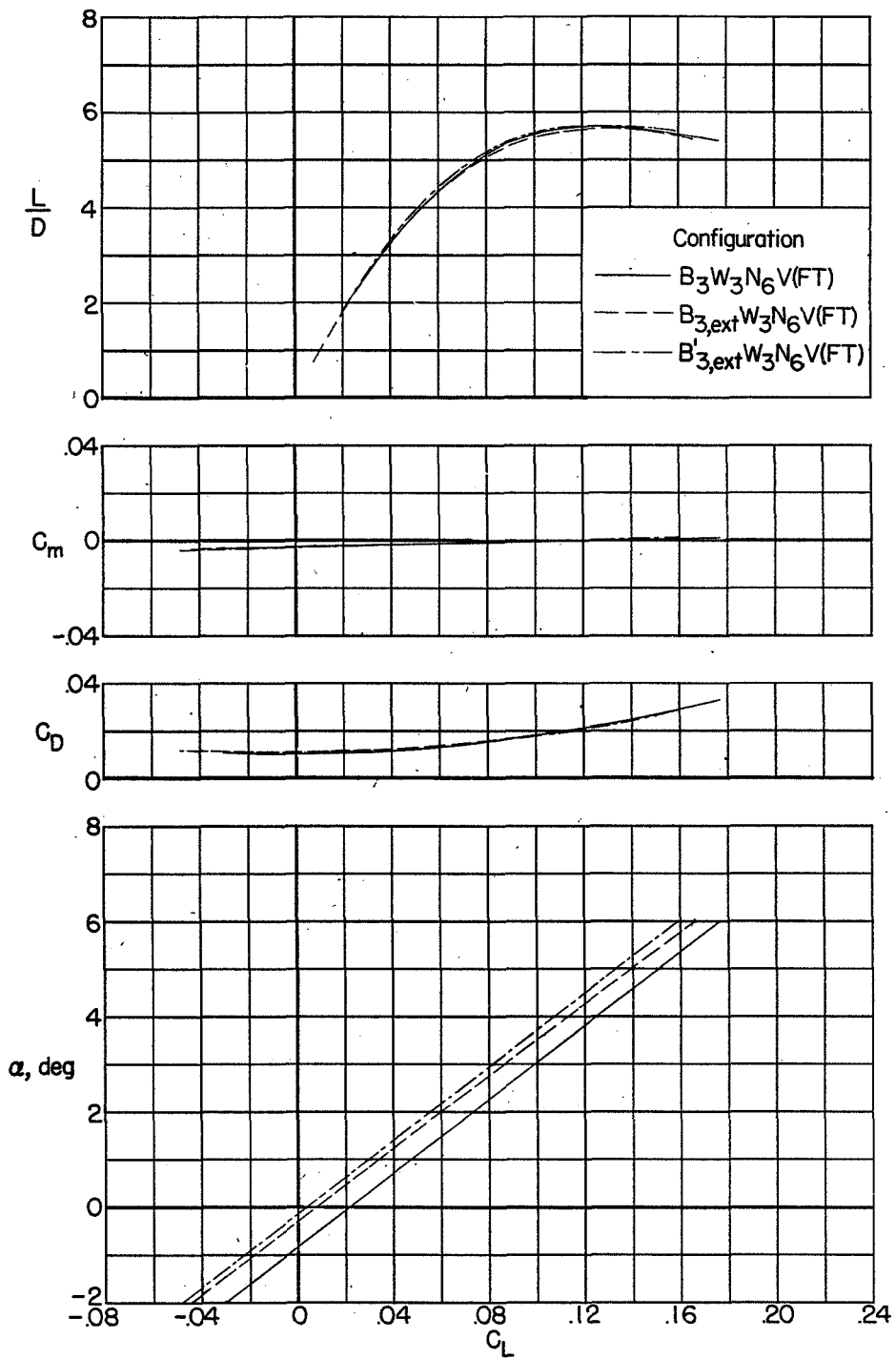


Figure 34.- Effect of body modification on the longitudinal characteristics of the delta-wing configuration.

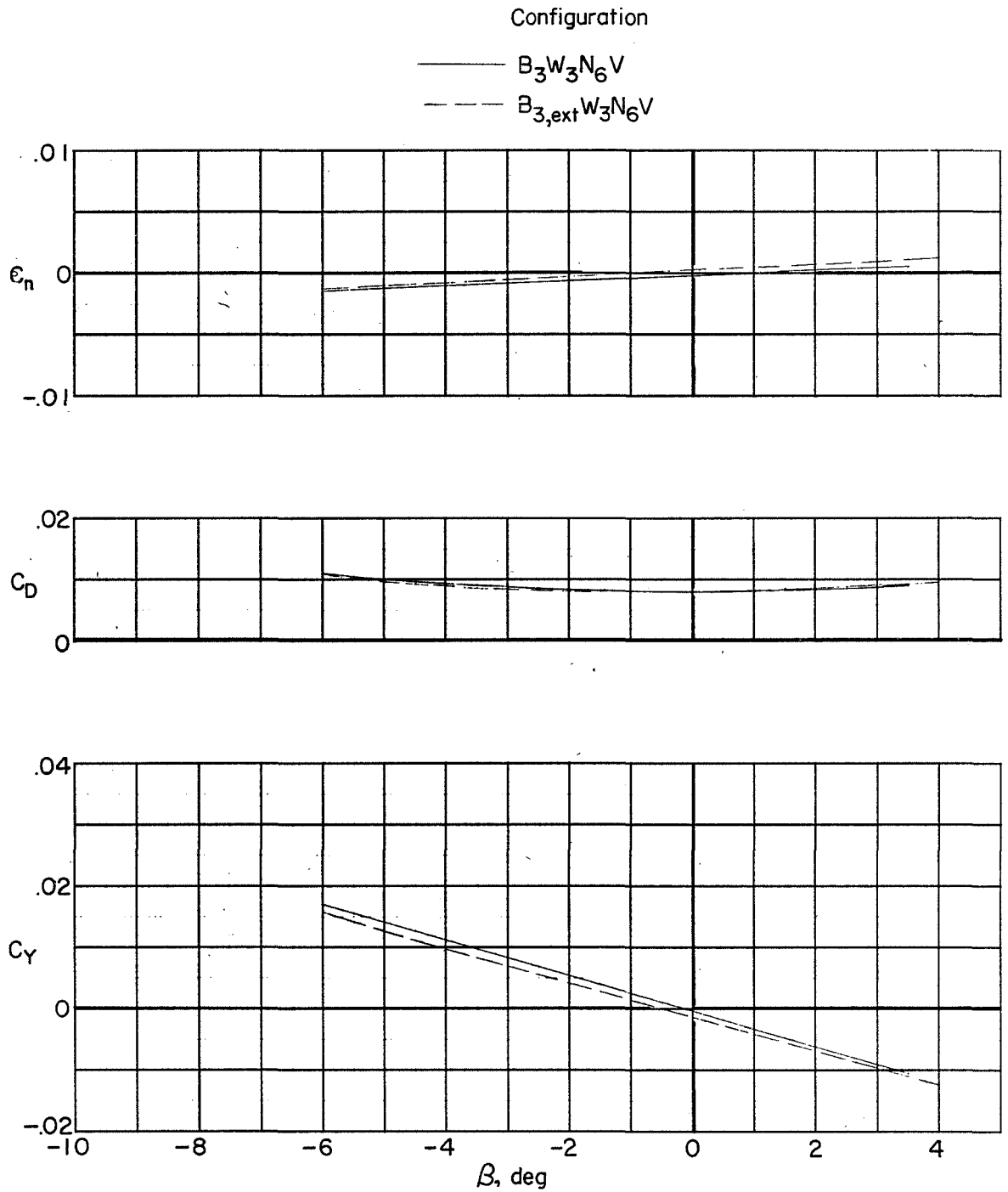
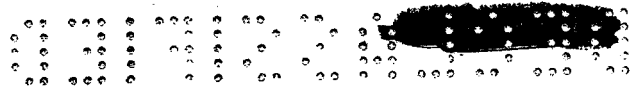


Figure 35.- Effect of body modification on the lateral characteristics of the delta-wing configuration.



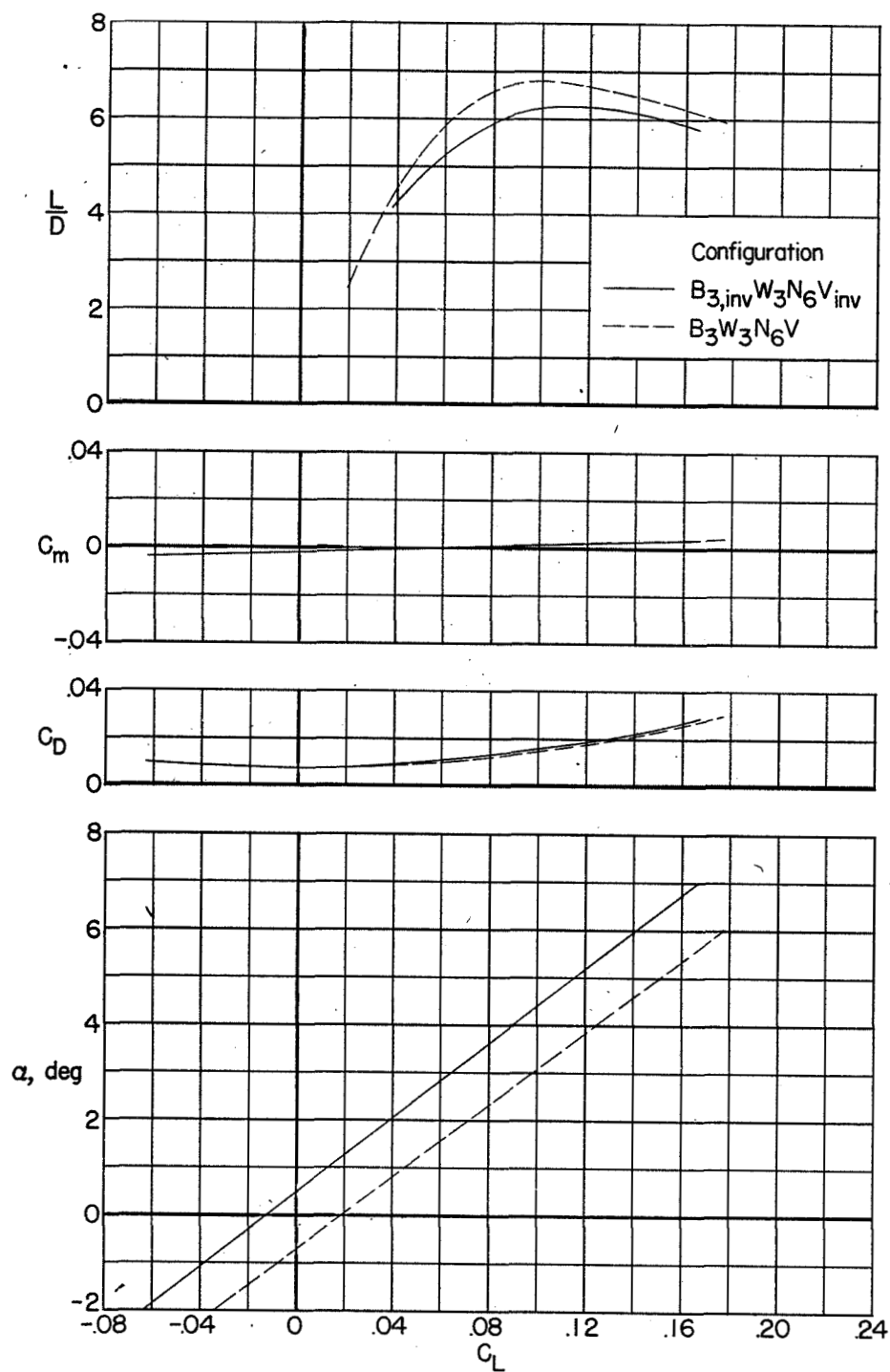


Figure 36.- Effect of inverting the body and vertical tail on the longitudinal characteristics of the delta-wing configuration.

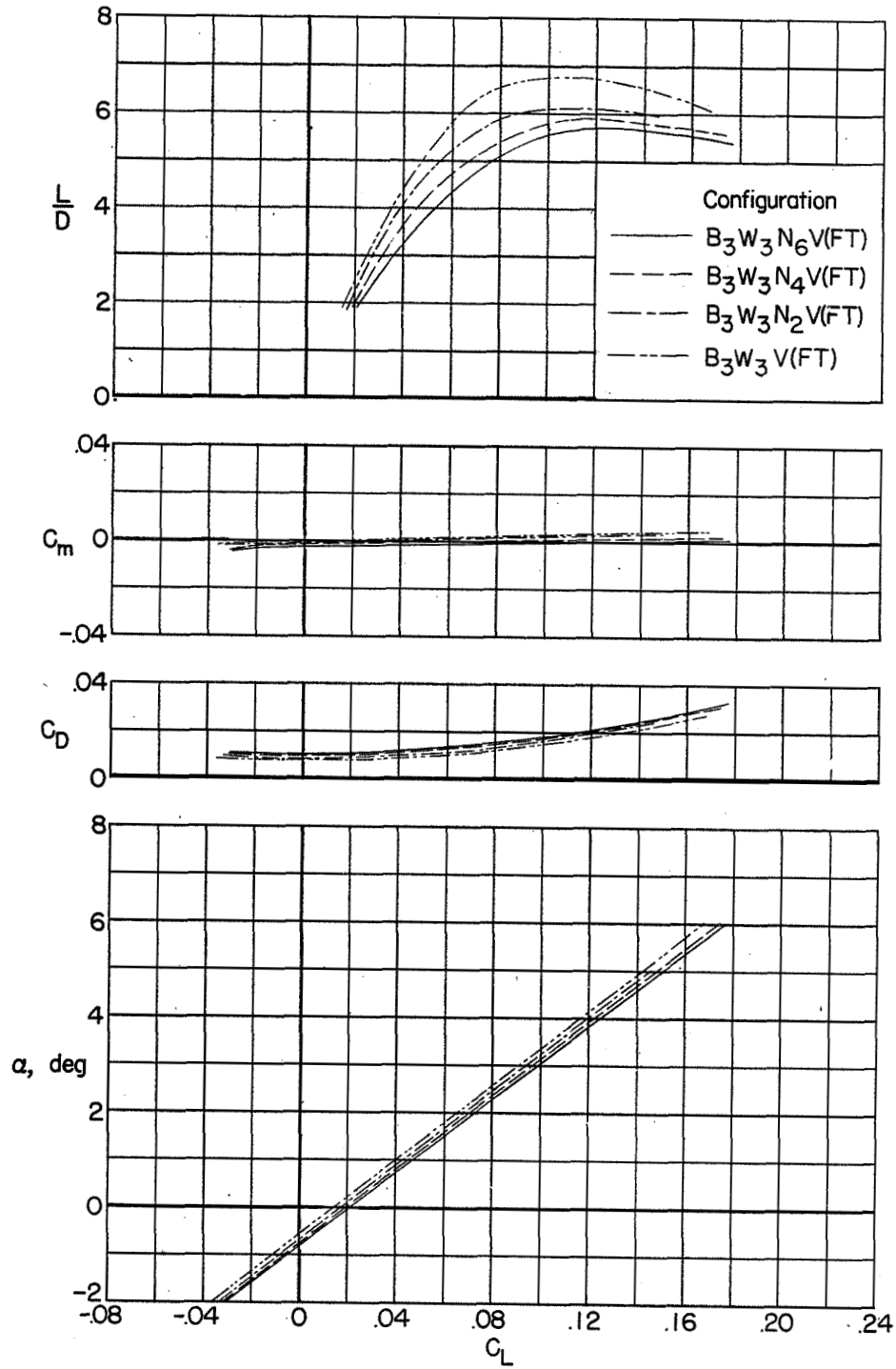
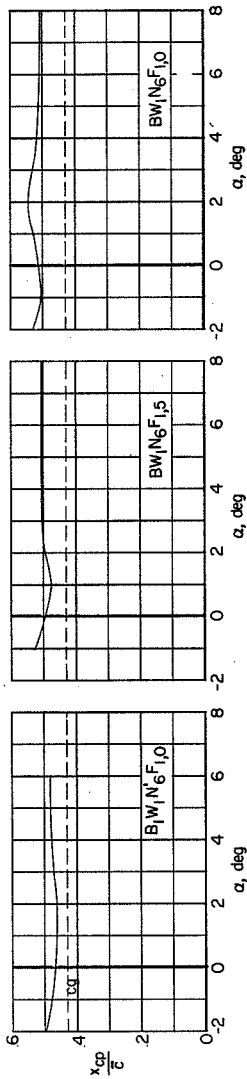
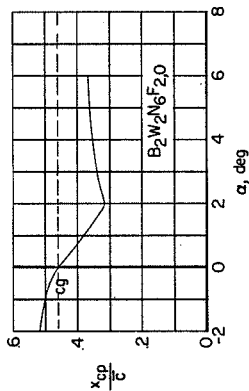


Figure 37.- Effect of nacelles on longitudinal characteristics of the delta-wing configuration.

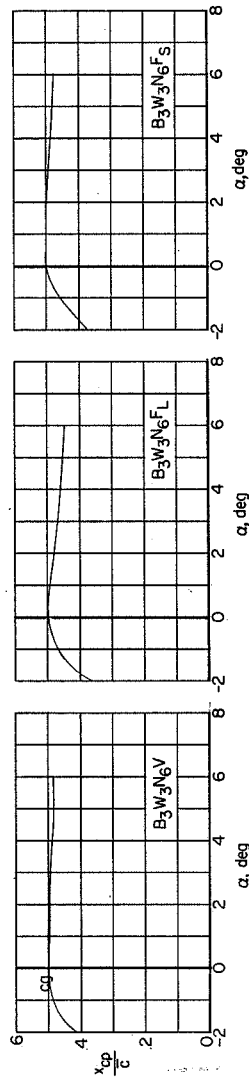




(a) Low-aspect-ratio arrow-wing configurations.

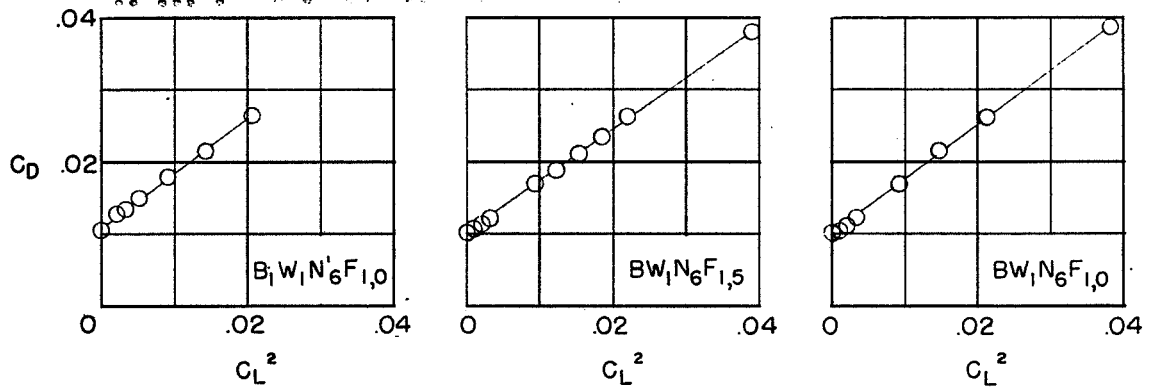


(b) High-aspect-ratio arrow-wing configuration.

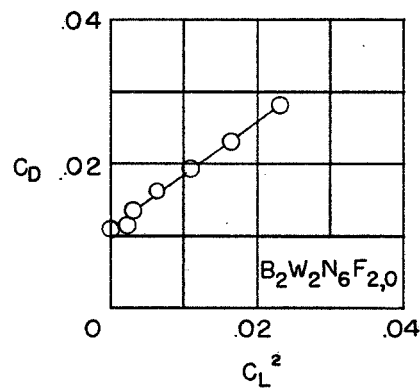


(c) Delta-wing configurations.

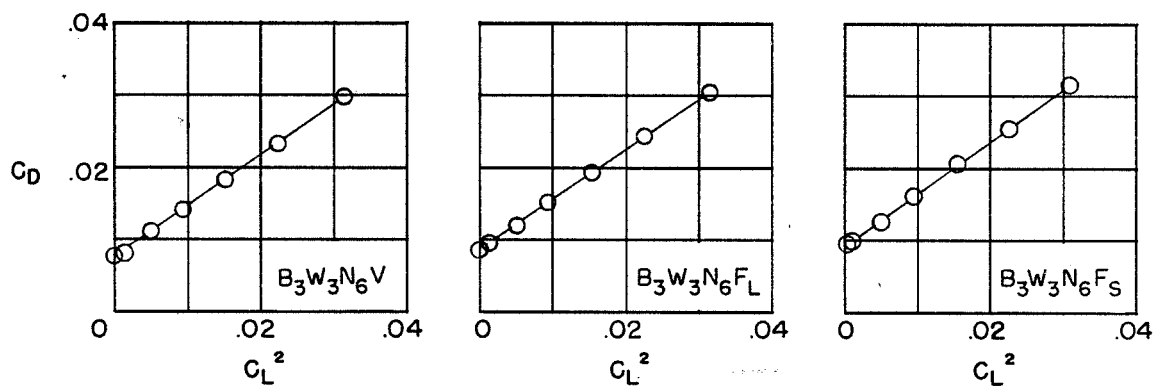
Figure 38.- Center-of-pressure variation of the basic low-aspect-ratio arrow-, high-aspect-ratio arrow-, and delta-wing configurations. (The assumed center of gravity is shown by a dashed line.)



(a) Low-aspect-ratio arrow-wing configurations.



(b) High-aspect-ratio arrow-wing configuration.



(c) Delta-wing configurations.

Figure 39.- Drag-due-to-lift variation for the basic low-aspect-ratio arrow-, high-aspect-ratio arrow-, and delta-wing configurations.

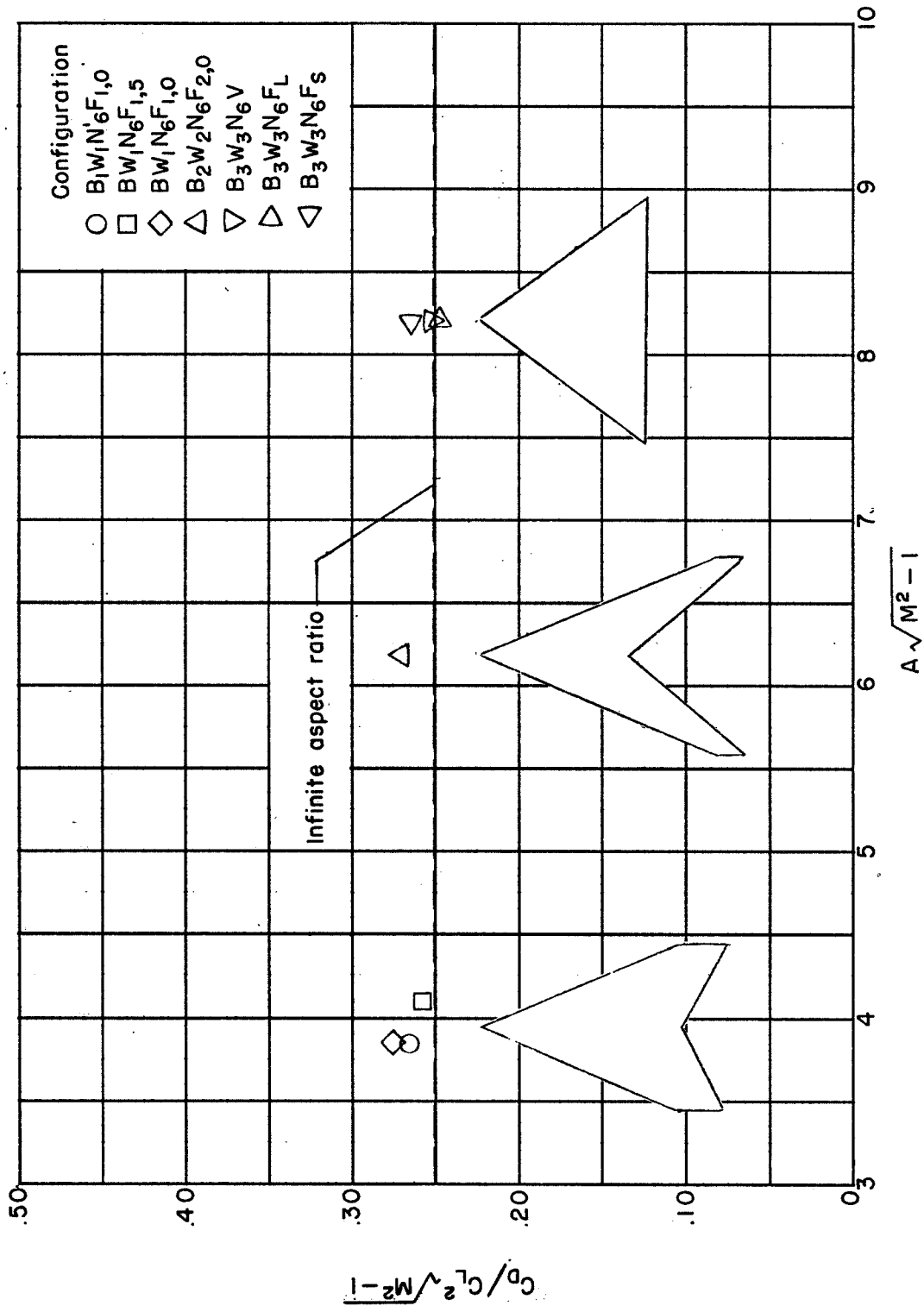
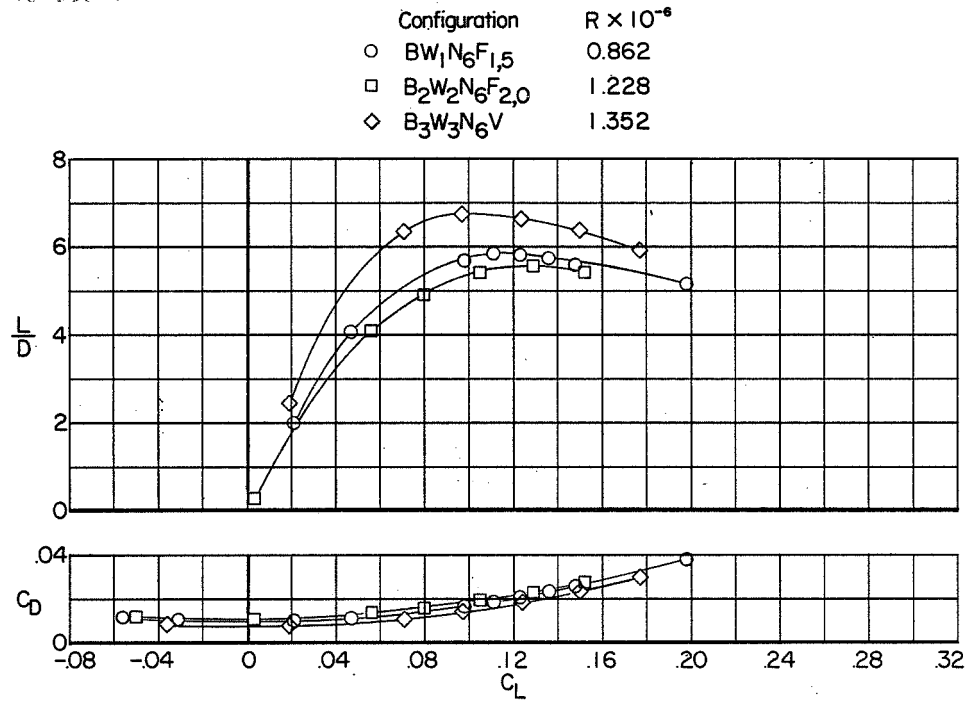
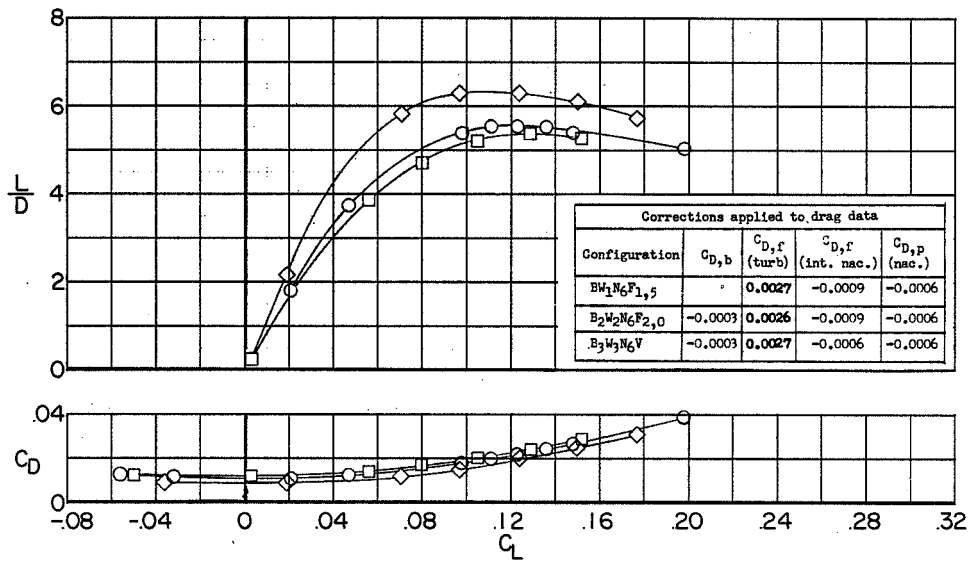


Figure 40.- Summary of drag-due-to-lift parameters for the low-aspect-ratio arrow-, high-aspect-ratio arrow-, and delta-wing configurations.



(a) Measured wind-tunnel data. (Natural transition.)



(b) Corrected wind-tunnel data.

Figure 41.- Comparison of the L/D characteristics of the basic low-aspect-ratio arrow-, high-aspect-ratio arrow-, and delta-wing configurations.

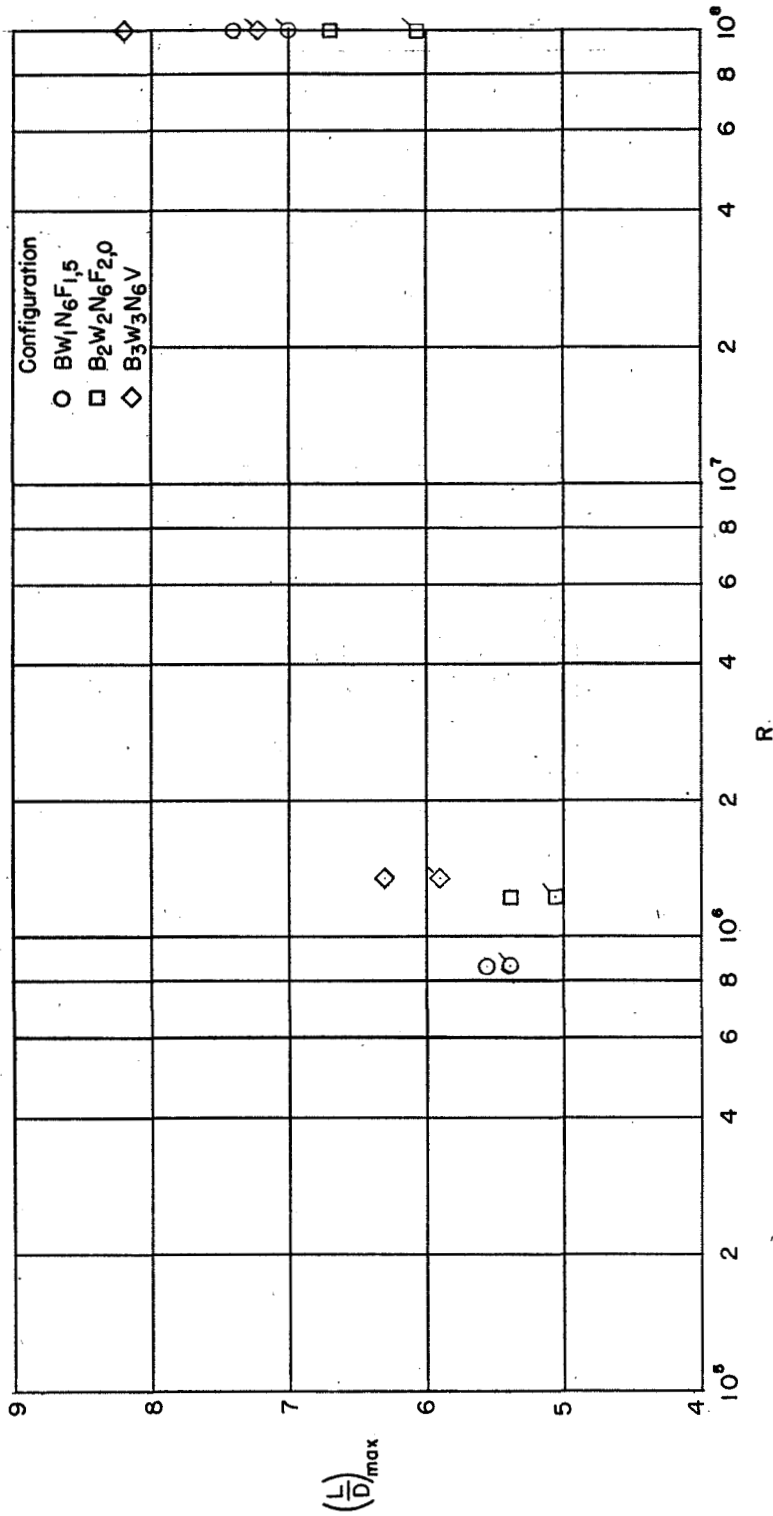


Figure 42.- Extrapolation of the lift-drag characteristics to full scale of the basic low-aspect-ratio arrow-, high-aspect-ratio arrow-, and delta-wing configurations. $M = 2.91$. (Flagged symbols denote the condition whereby the base-pressure coefficient on the models is assumed to be $-1/M^2$.)

